Numerical simulations of chromospheric physics: sunspot resonating cavity, 2D magnetic reconnection and forward modelling

B. J. Snow

PhD

2016

Numerical simulations of chromospheric physics: sunspot resonating cavity, 2D magnetic reconnection and forward modelling

Benjamin James Snow

A thesis submitted in partial fulfilment of the requirements of the University of Northumbria at Newcastle for the degree of Doctor of Philosophy

Research undertaken in the

Department of Mathematics, Physics and Electrical Engineering

February 2017

Abstract

There are three branches to this thesis: chromospheric resonator, forward modelling, and magnetic reconnection at different atmospheric heights.

The first branch investigates the behaviour of resonant waves in the chromosphere above sunspot umbrae. The steep temperature gradients at the solar photosphere and transition region allow waves to be partially transmitted and partially reflected creating the boundaries of a resonating cavity. These resonant waves can be used to explain the existence of three-minute oscillations frequently observed above sunspot umbrae. 1D numerical simulations have been performed of wave propagation along a magnetic field line perpendicular to the umbra to analyse the behaviour of this resonating cavity driven by continuous random noise. It was found that the gradient of the velocity spectra present in the corona is directly correlated with the size of the chromospheric cavity. This provides a potentially useful diagnostic for indirectly measuring chromospheric cavity size.

The second branch uses line-of-sight integration to compare simulation data with observations. LOS integration has been performed on two cases: 1D resonances above sunspot umbrae, and a 3D simulation of a coronal kink instability. The LOS integration of resonant waves is an extension to the first branch of this thesis. The intensity was calculated using several coronal lines. It was found that the broadband of excited frequencies is correlated with chromospheric cavity size, providing a potentially useful diagnostic for chromospheric cavity size. For the kink-unstable loop, several Hinode/EIS lines were used to investigate the observational intensity and Doppler velocities. It was found that the intensity maps overestimate the loop width due to temporal and spatial degradation. Synthetic intensity maps were also generated using spectral lines from the DKIST/DL-NIRSP instrument.

The final branch consists of a numerical investigation into the onset of 2D magnetic reconnection in the solar photosphere, chromosphere and corona. The initial state is an equilibrium Harris current sheet. A reconnection event is triggered by applying a velocity driver perpendicular to the magnetic field. This external velocity driver allows us to study the early behaviour of reconnection in a naturalistic manner. The heating manifests differently across the different atmospheric layers. The photospheric heating is guided by the slow-mode shocks. The chromospheric heating is confined to the reconnection region. The ambipolar diffusion in the chromospheric case alters the distribution of the current on the inflow region in line with theoretical models.

Contents

Acknowledgements

Firstly I would like to thank my supervisor Gert Botha. Without his expert guidance none of this would have been possible.

I would also like to thank all those who have all those who have provided assistance and advice over the last three years, in particular: James McLaughlin, Stéphane Régnier, Andrew Hillier and Richard Morton.

Finally I would like to thank Northumbria University for my studentship and the Royal Astronomical Society for their support in funding my conference attendance.

Declaration

I declare that the work contained in this thesis has not been submitted for any other award and that it is all my own work. I also confirm that this work fully acknowledges opinions, ideas and contributions from the work of others.
Any ethical clearance for the research presented in this thesis has been approved. Approval has been sought and granted by the University Ethics Committee on 7th of April 2014.

I declare that the Word Count of this Thesis is 36038 words.

Name: Benjamin James Snow

Signed:

Date:

Chapter 1

Introduction

Due to the Sun's proximity to Earth, there is a great deal of research and measurements which highlight that, despite being a fairly typical star, the Sun is a highly complex system supporting a wealth of interesting phenomena, for example: sunspots, flares, coronal mass ejections. This makes solar physics a highly interesting field of study.

In this thesis, numerical simulations using magnetohydrodynamics are used to elucidate various solar phenomena, namely oscillations above sunspot umbrae, and the onset of magnetic reconnection. Synthetic observables are also generated to investigate the oscillations above a sunspot umbra, and the observational signatures of a kink-unstable flux rope. This chapter presents a few specifics about the Sun which will provide context to the work presented in later chapters.

1.1 Structure of the Solar Atmosphere

Due to the complexity of the Sun, it is often separated into different layers based on key properties and phenomena. A simple schematic of this is shown in Figure 1.1. In this thesis, the key layers of interest are the solar photosphere, chromosphere, transition region and corona.

1.1.1 Photosphere

The visible surface of the Sun is a very thin layer of plasma known as the photosphere, from the Greek meaning 'Sphere of Light'. It is relatively cool at approximately 6000 K, has a high density, approximately 10^{23} m^{-3}, and is the visible 'surface' of the Sun. In the photosphere, the gas pressure generally exceeds the magnetic pressure and fluid

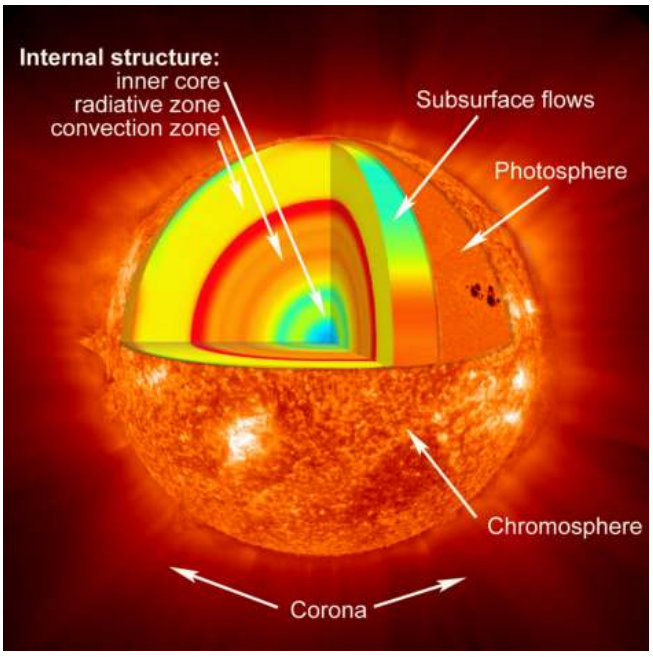

FIGURE 1.1: Solar structure, NASA [2007].

effects become more important than magnetic effects. The photosphere is subject to convective motions, namely granulation and supergranulation. The photosphere is home to various phenomena, for example sunspots and Ellerman bombs [Ellerman, 1917]. In the photosphere, absorption plays a significant role in the plasma intensity.

1.1.2 Chromosphere

The layer above the photosphere is called the chromosphere. In the chromosphere, the temperature is at a minimum ($T \approx 3600$ K), before rapidly rising at the transition region ($T \approx 10^4$) and the corona ($T \approx 10^6$ K). The density is also considerably lower than that of the photosphere due to the pressure balance and gravitational effects. The region's name, literally 'Sphere of Colour', originates from its observed reddish hue emitted by this region due to the presence of hydrogen at the given temperature, Hα emissions. This colour is visible when observed using a Hα filter or in prominences during a total eclipse. The chromosphere also emits a violet colour due to the ionized calcium atoms, Ca II. This colour has been observed in a number of other stars, providing insight into the active cycles and chromospheres of distant stars. The chromosphere is also a site of activity, with changes in solar flares, prominence and filament eruptions, and the flow of post flare loop material. Also, due to the low temperature of the chromosphere, the plasma is not fully ionized. As such, the underlying physics is altered by the presence of neutrals and an effective anisotropic resistivity is added. For these reasons, the chromosphere is a very interesting area of research.

There are a lot of interesting dynamics in the solar chromosphere. The plasma-β, the ratio of gas pressure to magnetic pressure, varies greatly in this region meaning that both fluid and magnetic effects are important. Magnetic reconnection events in this region include penumbral microjets [Katsukawa et al., 2007] and calcium (Ca II) jets [Shibata et al., 2007].

The steep temperature gradients at the photosphere and transition region allow waves to resonate in the chromospheric cavity above sunspot umbrae, with energy being partially transmitted and partially reflected at the photosphere and transition region. These resonances produce the three-minute oscillations that are frequently observed in the solar corona.

1.1.3 Transition region and corona

The transition region bridges the chromosphere and coronal regions of the Sun. In the transition region, the temperature rises rapidly, from a few thousand Kelvin to a few million Kelvin, over a distance of less then 100 km [Priest, 2014, p.p. 7].

The corona extends from the transition region, into the solar wind which fills the heliosphere. The solar corona is a low-density plasma at several million Kelvin. The magnetic effects dominate for small solar radii. At large solar radii, the magnetic field strength decreases and plasma effects dominate [e.g. Gary, 2001, Figure 3]. Key magnetic reconnection phenomena in the corona include x-ray jets [Shibata et al., 1992] and flares [Moore et al., 2001].

1.2 Magnetohydrodynamic Equations

The Sun can be approximated using the magnetohydrodynamics (MHD) equations. These equations arise from combining the Navier-Stokes equations for fluid dynamics, with Maxwell's equations for electromagnetism.

The MHD equations can include various different terms depending on the phenomena being investigated, for example resistive MHD includes a resistive term η. The equations used in this thesis vary across the major chapters as we investigate different effects. The MHD equations for a partially-ionised, non-linear, compressible plasma are given below.

$$\frac{\partial \rho}{\partial t} = -\nabla \cdot (\rho \mathbf{v}), \tag{1.1}$$

$$\frac{\partial \mathbf{v}}{\partial t} + \mathbf{v} \cdot \nabla \mathbf{v} = \frac{1}{\rho}\mathbf{J} \times \mathbf{B} - \frac{1}{\rho}\nabla P + \mathbf{g}, \tag{1.2}$$

$$\frac{\partial \mathbf{B}}{\partial t} = -\nabla \times \mathbf{E}, \tag{1.3}$$

$$\frac{\partial \epsilon}{\partial t} + \mathbf{v} \cdot \nabla \epsilon = -\frac{P}{\rho}\nabla \cdot \mathbf{v} + \frac{\eta}{\rho}J^2 + \frac{\eta_\perp}{\rho}J_\perp^2, \tag{1.4}$$

$$\mathbf{E} + \mathbf{v} \times \mathbf{B} = \eta \mathbf{J} + \eta_\perp \mathbf{J}_\perp, \tag{1.5}$$

$$\nabla \times \mathbf{B} = \mu_0 \mathbf{J}, \tag{1.6}$$

$$P = \frac{\rho k_B T}{\mu_m}, \tag{1.7}$$

$$\epsilon = \frac{P}{\rho(\gamma - 1)} + (1 - \xi_n)\frac{\chi_i}{\bar{m}}, \tag{1.8}$$

$$\mu_m = \frac{\bar{m}}{2 - \xi_n}, \tag{1.9}$$

where ρ, P, T, and $\mathbf{v}$ are the plasma density, pressure, temperature, and velocity, respectively. Here, $\mathbf{J}$ is current density, $\mathbf{B}$ is magnetic field, $\mathbf{E}$ is electric field, and $\mathbf{g}$ is gravity. The internal energy ϵ is given by Equation (1.8). Here, $\mu_m = 1.4 m_p$ where m_p is the mass of a proton, k_B is the Boltzmann constant, μ_0 is the permeability of free space, and $\gamma = 5/3$ is the ratio of specific heats. The Spitzer resistivity is η and the perpendicular resistivity is $\eta_\perp$. Ionisation potential for hydrogen is given by χ_i and the neutral fraction is ξ_n.

Equation (1.1) is the continuity of mass which states that mass cannot be created of destroyed. Mass can, however, enter or leave the system through inflows or outflows.

The momentum Equation (1.2) equates the acceleration of the plasma with the forces acting on the plasma, namely the Lorentz force $\mathbf{J} \times \mathbf{B}$, the pressure gradient ∇P, and gravitational force $\mathbf{g}$. Additional terms can be included to account for additional forces.

The induction Equation (1.3) equates the rate of change of the magnetic field with the curl of the electric field. Through Ohm's law (Equation (1.5)), the induction equation relates the magnetic field and velocity.

The rate of change of internal energy of the plasma is governed by Equation (1.4). This accounts for changes in the internal energy of the plasma through Ohmic heating (ηJ^2) and kinetic motion ($P \nabla \cdot \mathbf{v}$).

Ohm's law, Equation (1.5), relates the total electric field exerted by the plasma to the magnetic diffusion in the plasma.

Ampére's law, Equation (1.6), states that the magnetic field produces a current density that is perpendicular to the magnetic field lines.

In this thesis, the equation of state is given by the ideal gas law, Equation (1.7), which states that the pressure exerted by the plasma can be calculated from the density and temperature of the plasma.

Equation (1.8) give the internal energy of the plasma. This is calculated using the density and pressure of the plasma. There is also a term to account for the increased internal energy of ionised particles compared to neutrals. Note that since the internal energy appears as a derivative in other equations, only gradients in the internal energy are important.

The reduced mass μ_m, i.e. the average mass of all particles in the plasma, is given by Equation (1.9).

The species mass $\bar{m}$ is defined by considering the abundances of elements at the height of interest, for example in the corona, there is approximately 6% helium and 94% hydrogen with very low abundances of heavier particles [e.g. Schmelz et al., 2012], so the average species mass is approximately 1.2. In the chromosphere there are more heavy particles, resulting in $\bar{m} \approx 1.4 - 1.6$.

In the chromospheric resonator section of this thesis (Chapter 2), the above equations can be simplified by assuming an ideal plasma ($\eta = 0$) and neglecting the role of partial-ionisation ($\xi_n = 0$, $\eta_\perp = 0$). These reduced equations are given in Chapter 2.

1.3 LareXd

In this thesis, the MHD equations have been numerically implemented using LareXd [Arber et al., 2001]. LareXd is a Lagrangian remap code using a staggered grid for solving the MHD equations, written in Fortran 90. The name is derived from the two main steps in the solver. Firstly, in the Lagrangian stage, the grid is allowed to move with the fluid. This allows for higher grid resolution in key areas. However, when a shock is encountered, the grid can fold in on itself causing problems. LareXd circumvents this problem with the second stage, the remap phase where the variables on the distorted Lagrangian grid are remapped onto the original grid. This allows LareXd to accurately capture shocks without a Riemann solver and thus in LareXd fewer grid cells are necessary and the simulations are less computationally expensive. LareXd uses a predictor-corrector method scheme and is second order in both space and time.

LareXd has been widely used in the solar community since its introduction and is currently in a mature stage of development. Some of the salient features of LareXd are as follows:

1. Numerically solves the full set of nonlinear MHD equations
2. Enforces the constraint of $\nabla \cdot \mathbf{B} = 0$ using the constrained transport method on a staggered grid [Evans and Hawley, 1988]
3. Allows for implementation of different equations of state and physics, e.g. partial ionisation

The neutral fraction ξ_n is calculated using the modified Saha equation [Athay and Thomas, 1961] and is a function of density and temperature, i.e. $\xi_n = \xi_n(\rho, T)$. This was implemented in LareXd by Leake et al. [2005].

The normalisation in LareXd is performed by specifying a normalisation length scale L_0, magnetic field B_0, and density ρ_0. Normalisation for other parameters can then be calculated using these three specified normalisation values, i.e.

$$v_0 = \frac{B_0}{\sqrt{\mu_0 \rho_0}} \tag{1.10}$$

$$P_0 = \frac{B_0^2}{\mu_0} \tag{1.11}$$

$$t_0 = \frac{L_0}{v_0} \tag{1.12}$$

$$J_0 = \frac{B_0}{\mu_0 L_0} \tag{1.13}$$

$$E_0 = v_0 B_0 \tag{1.14}$$

$$T_0 = \frac{\epsilon_0 \bar{m}}{k_B} \tag{1.15}$$

$$\epsilon_0 = v_0^2 \tag{1.16}$$

$$\eta_0 = \mu_0 L_0 v_0 \tag{1.17}$$

In this thesis, a few modifications are made to the boundary conditions, initial conditions and the output routines to tailor LareXd to the specific problems investigated. The numerical set-up is discussed in detail in each chapter.

1.4 Waves in the Solar Atmosphere

There are a multitude of different wave modes that can be supported by MHD plasma. To derive these modes, consider the continuity, momentum, energy and induction equations for an ideal plasma:

$$\frac{d\rho}{dt} + \rho\nabla\cdot\mathbf{v} = 0, \tag{1.18}$$

$$\rho\frac{d\mathbf{v}}{dt} = -\nabla P + \mathbf{J}\times\mathbf{B} - \rho g\hat{\mathbf{z}}, \tag{1.19}$$

$$\frac{d}{dt}\left(\frac{P}{\rho^\gamma}\right) = 0, \tag{1.20}$$

$$\frac{\partial\mathbf{B}}{\partial t} = \nabla\times(\mathbf{v}\times\mathbf{B}), \tag{1.21}$$

$$\nabla\cdot\mathbf{B} = 0, \tag{1.22}$$

$$\mathbf{J} = \nabla\times\mathbf{B}/\mu_0, \tag{1.23}$$

$$T = \frac{mP}{k_B\rho}, \tag{1.24}$$

where $\frac{d}{dt}$ is the total derivative.

This is a simplified set of equations, assuming an adiabatic plasma and frozen flux. This derivation is adapted from Priest [2014].

The wave modes can be derived by applying perturbation analysis. For an equilibrium state consider a vertically stratified, stationary plasma with uniform magnetic field ($\mathbf{B}_0$) and temperature (T_0), where the density and pressure behave according to:

$$\rho_0(z) \propto e^{-z/H}, \tag{1.25}$$

$$P_0(z) \propto e^{-z/H}, \tag{1.26}$$

and satisfy the equilibrium momentum equation

$$\frac{dP_0}{dz} = -\rho_0 g, \tag{1.27}$$

for a scale height $H = P_0/\rho_0 g$.

Now, consider a small perturbation of this equilibrium state of the form:

$$\rho = \rho_0 + \rho_1, \tag{1.28}$$
$$\mathbf{v} = \mathbf{v}_1, \tag{1.29}$$
$$P = P_0 + P_1, \tag{1.30}$$
$$\mathbf{B} = \mathbf{B}_0 + \mathbf{B}_1, \tag{1.31}$$

where subscript '1' indicated a small quantity.

By applying these to Equations (1.18)-(1.24) and linearising by neglecting the product of small perturbation terms, we obtain:

$$\frac{\partial \rho_1}{\partial t} + (\mathbf{v}_1 \cdot \nabla)\rho_0 + \rho_0(\nabla \cdot \mathbf{v}_1) = 0, \tag{1.32}$$
$$\rho_0 \frac{\partial \mathbf{v}_1}{\partial t} = -\nabla P_1 + (\nabla \times \mathbf{B}_1) \times \mathbf{B}_0/\mu_0 - \rho_1 g\hat{\mathbf{z}}, \tag{1.33}$$
$$\frac{\partial P_1}{\partial t} + (\mathbf{v}_1 \cdot \nabla)P_0 - c_s^2 \left(\frac{\partial \rho_1}{\partial t} + (\mathbf{v}_1 \cdot \nabla)\rho_0 \right) = 0, \tag{1.34}$$
$$\frac{\partial \mathbf{B}_1}{\partial t} \times (\mathbf{v}_1 \times \mathbf{B}_0), \tag{1.35}$$
$$\nabla \cdot \mathbf{B}_1 = 0, \tag{1.36}$$

where

$$c_s^2 = \frac{\gamma P_0}{\rho_0}. \tag{1.37}$$

From Equations (1.32)-(1.36) it is possible to derive a single equation to investigate the different wave modes supported by MHD plasma.

First, differentiate Equation (1.33) with respect to time:

$$\rho_0 \frac{\partial^2 \mathbf{v}_1}{\partial t^2} = -\nabla \frac{\partial P_1}{\partial t} + \frac{\partial}{\partial t}((\nabla \times \mathbf{B}_1) \times \mathbf{B}_0/\mu_0) - \frac{\partial \rho_1}{\partial t} g\hat{\mathbf{z}}. \tag{1.38}$$

In this equation, all non-equilibrium terms are expressed as time derivatives and can be substituted using the perturbation Equations (1.32), (1.34) and (1.35) after some rearrangement.

Rearranging the perturbed continuity of mass Equation (1.32) gives

$$\frac{\partial \rho_1}{\partial t} = -(\mathbf{v}_1 \cdot \nabla)\rho_0 - \rho_0(\nabla \cdot \mathbf{v}_1). \tag{1.39}$$

This appears in Equation (1.38) as

$$-\frac{\partial \rho_1}{\partial t} = (\mathbf{v}_1 \cdot \nabla)\rho_0 + \rho_0(\nabla \cdot \mathbf{v}_1). \tag{1.40}$$

Equation (1.40) can be substituted into the energy equation (1.34) to yield

$$\frac{\partial P_1}{\partial t} = c_s^2(-(\mathbf{v}_1 \cdot \nabla)\rho_0 - \rho_0(\nabla \cdot \mathbf{v}_1) + (\mathbf{v}_1 \cdot \nabla)\rho_0) - (\mathbf{v}_1 \cdot \nabla)P_0 \tag{1.41}$$

$$\frac{\partial P_1}{\partial t} = -c_s^2(\rho_0(\nabla \cdot \mathbf{v}_1)) - (\mathbf{v}_1 \cdot \nabla)P_0. \tag{1.42}$$

But, from the equilibrium momentum equation

$$\frac{dP_0}{dz} = -\rho_0 g. \tag{1.43}$$

Therefore, Equation (1.42) becomes

$$\frac{\partial P_1}{\partial t} = -c_s^2\rho_0(\nabla \cdot \mathbf{v}_1) + v_{1z}\rho_0 g. \tag{1.44}$$

This equation appears in Equation (1.38) as:

$$-\nabla\frac{\partial P_1}{\partial t} = c_s\rho_0\nabla(\nabla \cdot \mathbf{v}_1) + \rho_0\gamma g(\nabla \cdot \mathbf{v}_1)\hat{\mathbf{z}} - g\rho_0\nabla v_{1z} - g v_{1z}\nabla\rho_0. \tag{1.45}$$

The time derivative of the induction equation appears in Equation (1.38) as

$$\begin{aligned}\frac{\partial}{\partial t}\left[(\nabla \times \mathbf{B}_1) \times \mathbf{B}_0/\mu_0\right] &= \left[\left(\nabla \times \frac{\partial \mathbf{B}_1}{\partial t}\right) \times \mathbf{B}_0/\mu_0\right] \\ &= \nabla \times [\nabla \times (\mathbf{v}_1 \times \mathbf{B}_0)] \times \mathbf{B}_0/\mu_0.\end{aligned} \tag{1.46}$$

Now, substituting Equations (1.40), (1.45) and (1.46) into (1.38) yields a single wave equation:

$$\begin{aligned}\frac{\partial^2 \mathbf{v}_1}{\partial t^2} &= c_s^2\nabla(\nabla \cdot \mathbf{v}_1) - (\gamma - 1)g\hat{\mathbf{z}}(\nabla \cdot \mathbf{v}_1) - g\nabla v_{1z} \\ &+ \nabla \times [\nabla \times (\mathbf{v}_1 \times \mathbf{B}_0)] \times \mathbf{B}_0/\mu_0\rho_0.\end{aligned} \tag{1.47}$$

This is a generalised wave equation (1.47) and plane-wave solutions can be found in terms of the frequency ω and the wavenumber vector $\mathbf{k}$ by assuming a wave form of

$$\mathbf{v}_1(\mathbf{r}, t) = \mathbf{v}_1 e^{i(\mathbf{k}\cdot\mathbf{r} - \omega t)}. \tag{1.48}$$

Equation (1.47) then becomes:

$$\omega^2 \mathbf{v}_1 = c_s^2 \mathbf{k}(\mathbf{k}\cdot\mathbf{v}_1) + i(\gamma-1)g\hat{\mathbf{z}}(\mathbf{k}\cdot\mathbf{v}_1) + igkv_{1z} + \langle \mathbf{k}\times[\mathbf{k}\times(\mathbf{v}_1\times\mathbf{B}_0)]\rangle \times \frac{\mathbf{B}_0}{\mu_0\rho_0}. \quad (1.49)$$

This equation allows us to consider the different types of waves that can exist.

1.4.1 Acoustic waves

Acoustic waves are compressional waves, e.g. sound waves, which are comprised solely of density and pressure fluctuations, i.e. $g = 0$ and $\mathbf{B}_0 = \mathbf{0}$. The wave equation (1.49) therefore reduces to:

$$\omega^2 \mathbf{v}_1 = c_s^2 \mathbf{k}(\mathbf{k}\cdot\mathbf{v}_1), \quad (1.50)$$

which has the dispersion relation

$$\omega = \pm k c_s. \quad (1.51)$$

This states that sound waves propagate uniformly in all directions with a phase speed and a group velocity of c_s.

Note that for a magnetic field solely in the same direction as the velocity perturbation, the generalised wave equation (1.49) still reduces to acoustic waves since the induction term $\mathbf{v}_1 \times \mathbf{B} = 0$. Therefore, the magnetic field acts as a wave guide for the acoustic waves. This is used in the resonances Chapter 2 of this thesis.

1.4.2 Acoustic cut-off frequency

For a stratified atmosphere, there is a minimum frequency for propagating waves. To derive this, Equation (1.47) can be considered in the z direction, assuming the absence of magnetic field ($\mathbf{B}_0 = \mathbf{0}$):

$$\frac{\partial^2 v_z}{\partial t^2} - c_s^2 \frac{\partial^2 v_z}{\partial z^2} + \gamma g \frac{\partial v_z}{\partial z} = 0. \quad (1.52)$$

Now, introduce the transform:

$$v_z(z,t) = \sqrt{\frac{\rho_0(0)c_s^2(0)}{\rho_0(z)c_s^2(z)}}\, Q(z,t). \quad (1.53)$$

Since $c_s^2 = \gamma p_0/\rho_0$ this transformation can be expressed as

$$v_z(z,t) = \sqrt{\frac{p_0(0)}{p_0(z)}}\, Q(z,t). \tag{1.54}$$

Substituting this transform into Equation (1.52) leads to

$$\frac{\partial^2 Q}{\partial t^2} - c_s^2 \frac{\partial^2 Q}{\partial z^2} + \gamma g \frac{\partial Q}{\partial z} + \frac{c_s^2}{p_0}\frac{\partial p_0}{\partial z}\frac{\partial Q}{\partial z} - \frac{\gamma g}{2p_0}\frac{\partial p_0}{\partial z} - \frac{3c_s^2 Q}{4p_0^2}\left(\frac{\partial p_0}{\partial z}\right)^2 + \frac{c_s^2}{2p_0 Q}\frac{\partial^2 p_0}{\partial z^2} = 0. \tag{1.55}$$

Now considering $\frac{\partial Q}{\partial z}$ terms and the pressure balance equation $\frac{dp_0}{dz} = -\rho_0 g$ we find that

$$\gamma g + \frac{c_s^2}{p_0}\frac{\partial p_0}{\partial z} = \gamma g - \frac{c_s^2}{p_0}\rho_0 g = \gamma g - \gamma g = 0, \tag{1.56}$$

and by considering Q terms we find:

$$-\frac{\gamma g}{2p_0}\frac{\partial p_0}{\partial z} - \frac{3c_s^2}{4p_0^2}\left(\frac{\partial p_0}{\partial z}\right)^2 + \frac{c_s^2}{2p_0}\frac{\partial^2 p_0}{\partial z^2} = -\frac{\gamma g^2 \rho_0}{4p_0}\left(1 + \frac{2p_0}{\gamma \rho^2}\frac{\partial \rho_0}{\partial z}\right) = \frac{c_s^2}{4H^2}\left(1 + 2\frac{\partial H}{\partial z}\right), \tag{1.57}$$

where

$$H = \frac{c_s^2}{\gamma g}. \tag{1.58}$$

Substituting these into Equation (1.55) yields a Klein-Gordon equation in terms of Q

$$\frac{\partial^2 Q}{\partial t^2} - c_s^2 \frac{\partial^2 Q}{\partial z^2} + \Lambda^2 Q = 0, \tag{1.59}$$

where

$$\Lambda^2 = \frac{c_s^2}{4H}\left(1 + 2\frac{\partial H}{\partial z}\right). \tag{1.60}$$

From this, a wave solution of the following form can be assumed

$$Q \propto \exp^{i(\omega t \pm kz)}, \tag{1.61}$$

which leads to the dispersion relation

$$\omega^2 = c_s^2 k^2 + \Lambda^2. \tag{1.62}$$

Now, for $k^2 > 0$ we yield the condition that the frequencies of the propagating wave must be higher than a critical cut-off ω_c

$$\omega > \frac{c_s}{2H}\sqrt{1 + 2\frac{\partial H}{\partial z}} = \omega_c. \tag{1.63}$$

Waves less than this critical frequency will be unable to propagate in the solar atmosphere and exist only as evanescent waves.

1.4.3 Alfvén waves

MHD also supports purely magnetic waves called Alfvén waves. When the magnetic field dominates the system, Equation (1.49) becomes

$$\omega^2 \mathbf{v}_1 = \left\langle \mathbf{k} \times \left[\mathbf{k} \times (\mathbf{v}_1 \times \hat{\mathbf{B}}_0) \right] \right\rangle \times \hat{\mathbf{B}}_0 v_A^2, \tag{1.64}$$

where $\hat{\mathbf{B}}_0$ is a unit vector in the direction of $\mathbf{B}_0$, and the Alfvén speed v_A is defined as

$$v_A = \frac{B_0}{\sqrt{\mu_0 \rho_0}}. \tag{1.65}$$

1.4.4 Fast and slow magnetoacoustic waves

For the case where gravity effects are negligible ($g = 0$) but both magnetic and pressure effects are important ($\mathbf{B} \neq 0$, $\rho_1 \neq 0$) the wave equation becomes:

$$\begin{aligned} \omega^2 \mathbf{v}_1 / v_A^2 &= k^2 \cos^2\theta_B \mathbf{v}_1 - (\mathbf{k} \cdot \mathbf{v}_1) k \cos\theta_B \hat{\mathbf{B}}_0 \\ &\quad + [(1 + c_s^2 v_A^2)(\mathbf{k} \cdot \mathbf{v}_1) - k \cos\theta_B (\hat{\mathbf{B}}_0 \cdot \mathbf{v}_1)] \mathbf{k}, \end{aligned} \tag{1.66}$$

where θ_B is the propagation angle.

This leads to the dispersion relation:

$$\omega^4 - \omega^2 k^2 (c_s^2 + v_A^2) + c_s^2 v_A^2 k^4 \cos^2\theta_B = 0, \tag{1.67}$$

which has two solutions for outwards propagating waves ($\omega/k > 0$):

$$\frac{\omega}{k} = \left[\frac{1}{2}(c_s^2 + v_A^2) \pm \frac{1}{2}\sqrt{c_s^4 + v_s^4 - 2 c_s^2 v_A^2 \cos 2\theta_B} \right]^{1/2}. \tag{1.68}$$

This has two solutions: a higher-frequency mode known as a fast magnetoacoustic wave, and a lower-frequency mode known as a slow magnetoacoustic wave.

1.5 Line-of-Sight Integration

With simulation data, one can easily isolate and analyse specific discrete points. In observations of the Sun, a range of points contribute to the observed intensity due to

the non-locality of radiative processes. To compare simulation results with observations it is necessary to apply line-of-sight integration to calculate to intensity along a line of sight. This analysis is valid for optically thin plasma, i.e. coronal plasma.

1.5.1 Intensity

For optically thin plasma, the line-of-sight intensity I can be calculated from the following formula:

$$I = \int R(T, n_e) n_e^2 dl, \tag{1.69}$$

where n_e is the electron number density, l is the line of integration and $R(T, n_e)$ is the response function. In this thesis, response function refers to the thermal response of the ion, i.e. the intensity of the ion at different temperature. In the simulations performed and analysed in this thesis, the electron number density is equal to the proton number density that can be calculated from the simulation mass density ρ. Note that if density variations in the plasma are small, one can assume a reference density and then the response is dependent on temperature only. This equation is valid for optically thin plasma, e.g. corona.

The SDO/AIA response functions R(T) were generated using version V6 available in ssw-idl [Boerner et al., 2012].

In 1D, integrating along a line produces a single intensity value. In 3D the integration can be performed over a series of parallel lines to produce a 2D intensity map.

1.5.2 Doppler velocities

Along a similar vein, the line-of-sight Doppler shifts D can be calculated according to:

$$D = \frac{\int R(T) n_e^2 \mathbf{v} \cdot d\mathbf{l}}{\int R(T) n_e^2 dl}, \tag{1.70}$$

where $\mathbf{v}$ is the velocity and the dot product with $\mathbf{l}$ produces the Doppler shift along the line of integration.

1.5.3 Line synthesis

The response function $R(T)$ accounts for the quantities of the ion or particle of interest at different temperatures. SSW/IDL contains response function for SDO/AIA spectral

lines. Contribution functions $C(T)$ can be generated for other instruments using CHIANTI V7 [Dere et al., 1997, Landi et al., 2013] and the generated contribution function can be used in place of $R(T)$.

1.6 Magnetic Reconnection Basics

Magnetic reconnection is ubiquitous in the solar atmosphere existing at photospheric levels (e.g. Ellerman bombs [Ellerman, 1917]), chromospheric levels (e.g. penumbral microjets [Katsukawa et al., 2007] and Ca II jets [Shibata et al., 2007]) and coronal levels (e.g. flares [Moore et al., 2001] and x-ray jets [Shibata et al., 1992]). In a sentence, magnetic reconnection is the process whereby there is a change in magnetic connectivity. This results in magnetic potential energy being converted into kinetic energy, thermal energy and energy of accelerated particles.

The classical schematic of reconnection involves oppositely directed magnetic fields diffusing and reconnecting, changing the global connectivity of the field lines [Priest, 2014, p.p. 189].

There are several effects caused by magnetic reconnection:

1. Convert magnetic energy to thermal energy via Ohmic dissipation
2. Accelerate plasma by converting magnetic energy to bulk kinetic energy
3. Accelerate particles
4. Change the magnetic field connectivity.

1.6.1 Sweet-Parker (slow) reconnection

The first quantitative model for magnetic reconnection was developed by Sweet [1958] and Parker [1957]. This was a model for 2D steady-state reconnection in an incompressible plasma. Under the assumption that the reconnection occurs in a current sheet with length set by the global scale L_e of the field, the inflow velocity is approximately

$$v_i = v_{Ai} S^{-1/2}, \tag{1.71}$$

where S is the Lundquist number and v_{Ai} is the Alfvén speed in the inflow region. The outflow velocity v_o in this case is v_{Ai}, independent of S.

The derivation of this result is as follows.

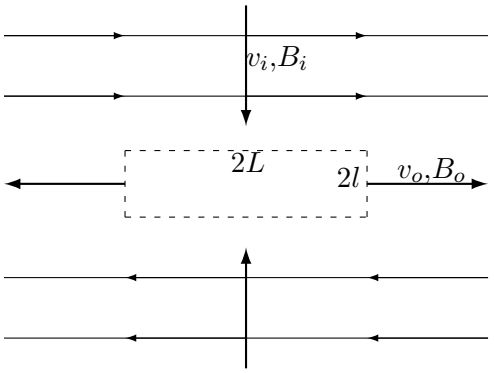

FIGURE 1.2: Sweet-Parker reconnection schematic with velocity and magnetic field v and B at inflow (subscript i) and outflow (subscript o) positions. Oppositely polarised magnetic field is separated by a diffusion region (dashed box) of width $2l$ and length $2L$.

Consider a simple diffusion region of length $2L$ and width $2l$ between oppositely directed magnetic fields with inflow velocity v_i and outflow velocity v_o (Figure 1.2).

For a steady state solution, the plasma must carry field lines inwards at the same rate they are trying to diffuse outwards.

In the inflow region, the current is approximately equal to zero ($J \approx 0$). Therefore, Ohm's law in the inflow region becomes:

$$E = v_i B_i. \tag{1.72}$$

At the centre of the diffusion region (point N) the magnetic field strength is zero ($B = 0$). Therefore, here Ohm's law gives

$$E = \eta \mu_0 J_N, \tag{1.73}$$

where η is the resistivity and μ_0 is the permeability of free space.

The current at this centre region can be approximated using Ampere's law:

$$J_N = \frac{B_i}{\mu_0 l}. \tag{1.74}$$

Combining Equations (1.72)-(1.74) yields the rate of diffusion

$$v_i B_i = \mu_0 \eta J_N, \tag{1.75}$$

$$v_i = \frac{\eta}{l}. \tag{1.76}$$

Now consider the conservation of mass, i.e. mass inflow = mass outflow:

$$Lv_i = lv_o. \tag{1.77}$$

Using Equations (1.76) and (1.77), the diffusion width l can be eliminated:

$$v_i^2 = \frac{\eta v_o}{L}, \tag{1.78}$$

or in terms of non-dimensional parameters:

$$M_i = \frac{\sqrt{v_0/v_{Ai}}}{\sqrt{R_{mi}}}, \tag{1.79}$$

for an inflow Alfvén Mach number $M_i = v_i/v_{Ai}$ and an inflow magnetic Reynolds number $R_{mi} = Lv_{Ai}/\eta$.

Now, if v_o, v_i and L are known, one can calculate the width of the diffusion region from Equation (1.77):

$$l = \frac{Lv_i}{v_o}, \tag{1.80}$$

and the outflow magnetic field strength can be determined from flux conservation:

$$v_i B_i = v_o B_o, \tag{1.81}$$

$$B_o = B_i \frac{v_i}{v_o}. \tag{1.82}$$

However, this relies on knowing the values of v_o, v_i and L. To calculate v_o consider the order of magnitude of the current $J \approx B_i/(\mu l)$. This leads to the Lorentz force:

$$\mathbf{J} \times \mathbf{B} \approx JB_o = B_i \frac{B_o}{\mu l}. \tag{1.83}$$

Now, the Lorentz force acts to accelerate plasma from rest at centre point N, to v_o over distance L. Therefore, by equating the inertial term $\rho(v \cdot \nabla)v_x$, neglecting pressure gradient, to the Lorentz force we find that

$$\rho \frac{v_o^2}{L} = \frac{B_i B_o}{\mu l}. \tag{1.84}$$

However, since $\nabla \cdot \mathbf{B} = 0$, $B_o/l \approx B_i/L$, Equation (1.84) can be rewritten as

$$v_o = \frac{B_i}{\sqrt{\mu\rho}} \equiv v_{Ai}. \tag{1.85}$$

Hence Equation (1.79) can be rewritten to yield the Sweet-Parker reconnection rate:

$$v_i = \frac{v_{Ai}}{\sqrt{R_{mi}}}, \tag{1.86}$$

or in terms of the Lundquist number:

$$\frac{v_i}{v_{Ai}} \approx \frac{1}{S^{1/2}}. \tag{1.87}$$

This leads to plasma being ejected from a current sheet of width

$$l = \frac{L}{\sqrt{R_{mi}}}, \tag{1.88}$$

at speed

$$v_o = v_{Ai}, \tag{1.89}$$

with a magnetic field strength of

$$B_o = \frac{B_i}{\sqrt{R_{mi}}}. \tag{1.90}$$

This type of reconnection is often referred to as slow reconnection. Solar magnetic Reynolds numbers in the coronal are typically in the range $10^6 \lesssim R_{mi} \lesssim 10^{12}$ [Priest, 2014, p.p. 209] which means that the reconnection rate predicted by Sweet-Parker is far too slow.

1.6.2 Petscheck (fast) reconnection

The slow reconnection rate of Sweet-Parker reconnection is partially due to the aspect ratio of the diffusion region. For astrophysical plasmas the Lundquist number is very large, resulting in a slow reconnection rate and a high aspect ratio diffusion region. A faster reconnection rate was derived by Petschek [1964]. This method again assumed a steady-state, however the initial schematic includes two pairs of slow shocks separating the inflow and outflow regions and a diffusion region aspect ratio of order one, as shown in Figure 1.3. Far from the diffusion region, the magnetic field is of uniform strength B_e, which decreases to B_i towards the diffusion region. The velocity increases from far-field value v_e to inflow value v_i. The slow-mode shocks have a normal magnetic field component B_N which in a small variation from the equilibrium value B_e. This produced slightly curved magnetic field lines in the inflow region.

Now, in the upper inflow region, the magnetic field can be considered as a uniform field (of strength B_e) plus a potential field of strength B_N along the shock waves that

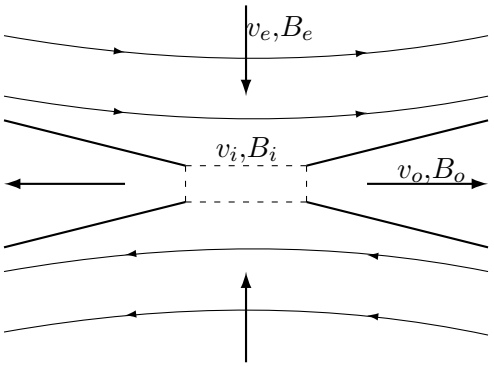

FIGURE 1.3: Petschek reconnection schematic. The solid lines indicate shocks.

approached zero at the diffusion region. A low order approximation can be applied to neglect the curvature of the magnetic field lines and the normal field can be considered as a series of poles. This results in a potential field of strength $\pm 2B_N/\pi$ between $L \leq L_e$ and $-L_e \leq -L$. Integrating this over the length dx gives the diffusion region inflow:

$$B_i = B_e - \frac{4B_N}{\pi} \log \frac{L_e}{L}. \tag{1.91}$$

The slow-mode shock propagates at the local Alfvén speed based on the normal magnetic field strength, i.e. $v_e = B_N/\sqrt{\mu\rho}$. Substituting this into Equation (1.91) yields:

$$B_i = B_e \left(1 - \frac{4M_e}{\pi} \log \frac{L_e}{L}\right). \tag{1.92}$$

Petschek estimated the maximum reconnection rate by assuming $B_i = \frac{1}{2}B_e$, arguing that the reconnection cannot be sustained if B_i is too small. This results in a faster reconnection rate:

$$\frac{v_i}{v_{Ai}} \approx \frac{\pi}{8 \ln S}. \tag{1.93}$$

1.6.3 Partial ionisation

The temperature in the solar atmosphere varies by orders of magnitudes, from the several-thousand degree photosphere, to the several-million degree corona. As such, the energy levels vary greatly depending on the area of interest. In the corona, there is sufficiently high energy to ionise all present particles. However, at chromospheric temperature and density conditions, the energy levels are far lower, resulting in neutral particles in addition to ionised particles. At the photosphere, these neutral particles dominate, i.e. the plasma is weakly-ionised. As one moves further up through the solar

atmosphere, the energy levels increase and ionised particles emerge. When both these ionised and neutral particles are present, Cowling resistivity becomes prominent.

1.6.3.1 Estimating the neutral fraction

To estimate the ionisation degree, one can use the Saha equation. This assumes a local thermal equilibrium (LTE) and allows one to estimate the ionisation level by considering a single temperature. For a pure hydrogen plasma this is given by

$$\frac{n_i^2}{n_n} = f(T) = \left(\frac{2\pi m_e k_B T}{\bar{h}^2}\right)^{3/2} \exp\left(-\frac{\chi_i}{k_B T}\right), \tag{1.94}$$

where $\bar{h}$ is Planck's constant.

By defining the neutral fraction ξ_n as;

$$\xi_n = \frac{n_n}{n_i + n_n}, \tag{1.95}$$

where n_n is the number of neutral particles and n_i is the number of ionised particles, one can estimate the neutral fraction via

$$r = \frac{n_n}{n_i} = \frac{1}{2}\left(-1 + \sqrt{1 + \frac{4\rho/m_i}{f(T)}}\right), \tag{1.96}$$

and finally,

$$\xi_n = \frac{r}{1+r}. \tag{1.97}$$

This however is only valid for LTE plasma. For many solar phenomena this approximation is not appropriate. However, solving for ionisation levels fully at each time step is too computationally expensive. Fortunately, the Saha equation can be modified to include a photospheric radiation temperature to approximate the non-LTE effects on hydrogen ionisation [Brown, 1973]. Note that alternatively, a look-up table can be created to estimate the ionisation level of the plasma based in plasma properties.

For the modified Saha equation:

$$\frac{n_i^2}{n_n} = \frac{f(T)}{b(T)}, \tag{1.98}$$

where

$$f(T) = \left(\frac{2\pi m_e k_B T}{\bar{h}^2}\right)^{3/2} \exp\left(-\frac{\chi_i}{k_B T}\right), \tag{1.99}$$

$$b(T) = \frac{T}{\omega T_R} \exp\left[\frac{\chi_i}{4k_B T}\left(\frac{T}{T_R} - 1\right)\right], \tag{1.100}$$

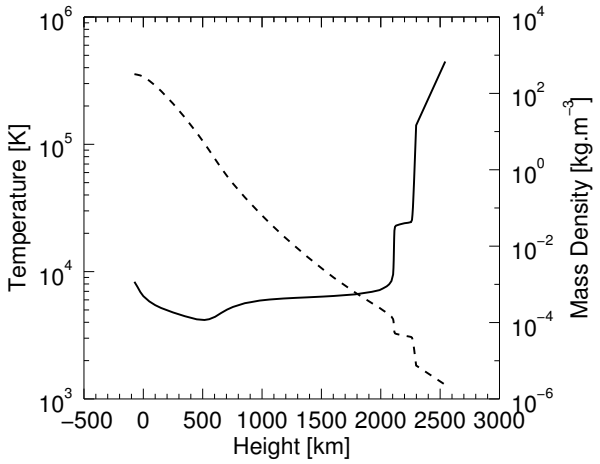

FIGURE 1.4: Temperature and density profiles of the VALC model for the quiet Sun.

with T_R the photospheric temperature and $\omega = 1/2$ a dilution factor.

As before, to calculate the neutral fraction use

$$r = \frac{n_n}{n_i} = \frac{1}{2}\left(-1 + \sqrt{1 + \frac{4\rho/m_i}{f(T)/b(T)}}\right), \tag{1.101}$$

and finally

$$\xi_n = \frac{r}{1+r}. \tag{1.102}$$

1.6.3.2 Quiet Sun ionisation levels

Now that the neutral fraction can be approximated it is possible to look at how this changes throughout the solar atmosphere. Using the VALC model [Vernazza et al., 1981] for the quiet Sun temperatures and densities (Figure 1.4), the ionised fraction can be estimated, see Figure 1.5. This shows that, as expected, the photosphere (height 0km) consist of neutral particles and the transition region (height 2500 km) is predominantly ionised particles. In the chromosphere both neutral and ionised particles exist and at approximately 2100 km, the temperature is approximately 9200 K and both neutral and ionised particles exist in roughly equal quantities.

1.6.3.3 Resistivity

The ionisation fraction comes into play when calculating the Spitzer (η) and Cowling (η_c) resistivity terms. Spitzer resistivity arises due to electron-ion collisions, whereas Cowling resistivity is due to neutral-ion collisions.

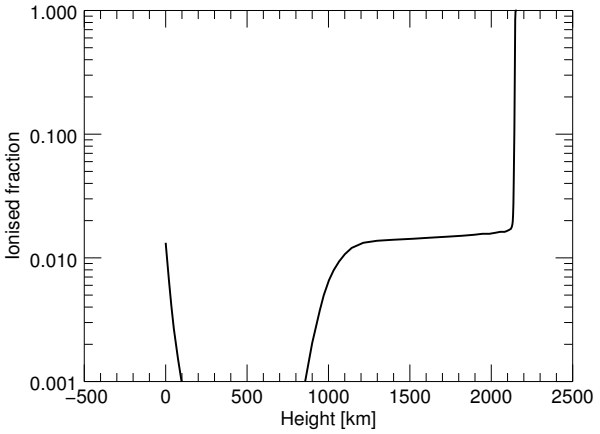

FIGURE 1.5: Ionisation fraction of the quiet Sun.

Spitzer resistivity can be calculated according to

$$\eta = \frac{m_e n_e (\nu_{ei}^{'} + \nu_{en}^{'})}{e^2 n}, \tag{1.103}$$

where $\nu_{ei}^{'}$ and $\nu_{en}^{'}$ are the effective collisional frequencies of electron and ion, and electron and neutral particles. The collisional frequencies for neutral collisions can be estimated according to Spitzer [1962]

$$\nu_{in} = n_n \sqrt{\frac{8 k_B T}{\pi m_{in}}} \Sigma_{in}, \tag{1.104}$$

$$\nu_{en} = n_n \sqrt{\frac{8 k_B T}{\pi m_{en}}} \Sigma_{en}, \tag{1.105}$$

$$\nu_{ei} = 3.7 \times 10^{-6} \frac{n_i \ln(\Lambda)}{T^{3/2}}, \tag{1.106}$$

where Σ_{in} and Σ_{en} are the ion-neutral and electron-neutral cross-sections, and $\ln\Lambda$ is the Coulomb logarithm.

Cowling resistivity can be calculated by

$$\eta_c = \eta + \frac{\xi_n^2 |\mathbf{B}|^2}{m_e n_e \nu_{en}^{'} + m_i n_i \nu_{in}^{'}}. \tag{1.107}$$

These values can be calculated using the VALC profile using an estimate for $|\mathbf{B}| = 100$ G. Note that whilst the choice of the magnetic field strength does change the magnitude of Cowling resistivity, this term is always several orders larger than the Spitzer resistivity in the partially ionised chromosphere. The Spitzer and Cowling resistivity terms using a constant $\mathbf{B} = 100$ G are shown in Figure 1.6. Note that in the sun, the magnetic

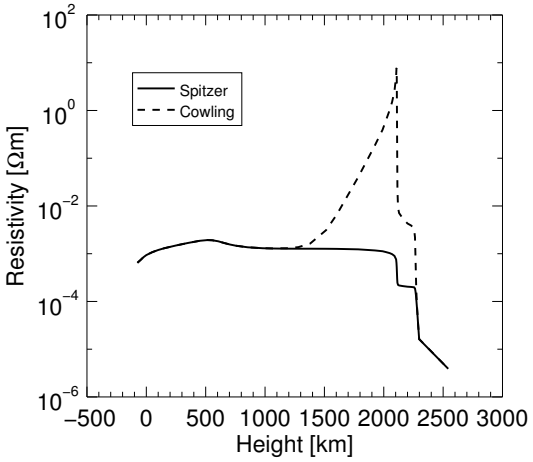

FIGURE 1.6: Spitzer and Cowling resistivity in the VALC quiet Sun.

field strength generally decreases with height, which would smooth out the sharp peak in Cowling resistivity in Figure 1.6.

1.6.4 Harris current sheet

In the 2D reconnection study (Chapter 4), a Harris current sheet will be used as the initial magnetic field configuration. This is of the form:

$$\mathbf{B} = (0, b, 0) \tag{1.108}$$

$$b = B_0 \tanh\left(\frac{x}{B_s}\right), \tag{1.109}$$

where B_s defines the width of the current sheet.

To obtain a stable initial condition one can solve the pressure balance equation to find the equilibrium position. In equilibrium, the momentum Equation (1.2) reduces to

$$\nabla P = \mathbf{J} \times \mathbf{B}, \tag{1.110}$$

$$\nabla\left(\frac{\rho k_B T}{\mu_m}\right) = \frac{1}{\mu_0}(\nabla \times \mathbf{B}) \times \mathbf{B}. \tag{1.111}$$

Assuming temperature is constant leads to

$$\frac{k_B T}{\mu_m}\nabla\rho = \left[\left(\frac{\partial}{\partial x}, \frac{\partial}{\partial y}, \frac{\partial}{\partial z}\right) \times (0, b, 0)\right] \times (0, b, 0), \tag{1.112}$$

$$\frac{\partial \rho}{\partial x} = -\frac{\mu_m b}{\mu_0 k_B T}\frac{\partial b}{\partial x}. \tag{1.113}$$

Now, $\partial b/\partial x$ can be evaluated as $(B_0/B_s)\text{sech}^2(x/B_s)$ leading to

$$\frac{\partial \rho}{\partial x} = -\frac{\mu_m B_0}{\mu_0 k_B T}\tanh\left(\frac{x}{B_s}\right)\frac{B_0}{B_s}\text{sech}^2\left(\frac{x}{B_s}\right), \tag{1.114}$$

$$= -\frac{\mu_m B_0^2}{\mu_0 k_B T B_s}\frac{\sinh\left(\frac{x}{B_s}\right)}{\cosh\left(\frac{x}{B_s}\right)}\frac{1}{\cosh^2\left(\frac{x}{B_s}\right)}, \tag{1.115}$$

$$= -\frac{2\rho_0}{B_s}\frac{\mu_m B_0^2}{2\mu_0 k_B T \rho_0}\frac{\sinh\left(\frac{x}{B_s}\right)}{\cosh^3\left(\frac{x}{B_s}\right)}. \tag{1.116}$$

Now, $\beta = \mu_m B_0^2/2\mu_0 k_B T \rho_0$, so that

$$\frac{\partial \rho}{\partial x} = -\frac{2\rho_0}{B_s \beta}\frac{\sinh\left(\frac{x}{B_s}\right)}{\cosh^3\left(\frac{x}{B_s}\right)}, \tag{1.117}$$

$$\rho = \int -\frac{2\rho_0}{B_s \beta}\frac{\sinh\left(\frac{x}{B_s}\right)}{\cosh^3\left(\frac{x}{B_s}\right)}dx, \tag{1.118}$$

$$= \frac{\rho_0}{\beta}\cosh^{-2}\left(\frac{x}{B_s}\right) + C. \tag{1.119}$$

The normalised constant of integration C is chosen as unity.

1.7 Overview of Thesis

There are three main branches to this thesis: chromospheric resonator, LOS integration, and magnetic reconnection.

1.7.1 Chromospheric resonator

The first branch in this thesis consist of a 1.5D numerical investigation into the behaviour of a chromospheric resonator above a sunspot umbra. The steep temperature gradients at the photosphere and transition region define a chromospheric cavity. Energy is partially transmitted and partially reflected at the photosphere and transition region. This allows waves to resonate in the chromospheric cavity.

In this thesis, resonances are driven by applying continuous random noise to the upper convection zone. These velocity perturbations propagate into the chromospheric cavity, where they resonate and produce a wave train that propagates into the corona.

The temperature configuration in the chromospheric cavity is then varied and the resultant coronal velocity spectra analysed. It is found that as the chromospheric cavity increases in size, the gradient of the coronal spectra becomes shallower. This is a potentially useful diagnostic for estimating the size of the chromospheric cavity.

1.7.2 Line-of-sight (LOS) integration

The second branch consists of performing LOS integration on the chromospheric resonator and a kink-unstable coronal flux tube to generate the observable spectra.

1.7.2.1 Chromospheric resonator

For the chromospheric resonator, 1D LOS integration is performed to look at the resultant waves present in the corona and upper transition region using SDO/AIA, TRACE and Hinode/EIS spectral lines. It is found that the broadband of exited frequencies becomes narrower as the chromospheric cavity size increases.

1.7.2.2 Kink-unstable coronal flux rope

The kink-unstable flux rope is a 3D simulation and LOS integration is performed to create 2D intensity and Doppler velocity maps using Hinode/EIS spectral lines and DKIST/DL-NIRSP spectral lines.

Using Hinode/EIS, several qualities of a kink-unstable flux rope can be detected observationally using Hinode/EIS. Firstly, the moving intensity rasters demonstrated an increase in intensity towards the loop edge. This is due to the loop conducting heat radially outwards, activating different spectral lines. Secondly, the growth of the loop could be measured in the intensity maps. Comparing this to the loop width measured in the simulation resolution intensity maps shows that the loop width is overestimated in the sit-and-stare intensity maps. Finally, the dense Doppler raster near the centre of the loop detected oppositely directed Doppler velocities. This corresponds to velocity being guided along a twisted magnetic field line in the simulation.

1.7.3 Onset of magnetic reconnection

The third branch of this thesis investigates 2D magnetic reconnection, in particular, the onset of magnetic reconnection in the solar corona, photosphere and chromosphere. The reconnection is triggered by applying an external velocity driver far away from an

equilibrium Harris current sheet. Waves and flows are ubiquitous in the solar atmosphere and this driver allows the onset of reconnection due to these waves encountering current sheets to be investigated in a naturalistic manner.

The parameter space is investigated for a fully-ionised plasma characteristic of the solar corona and the contributions of each parameter are studied independently. The role of ambipolar diffusion and partial ionisation is investigated for a chromospheric case. Comparisons are then made between the different atmospheric heights.

A reconnecting state is reached for all atmospheric heights considered, however the event is highly dependent on the chosen parameters and atmospheric conditions. The coronal case achieves a sharp rise in electric field (indicative of reconnection) for a range of velocity drivers. The electric field in the photospheric case is highly dependent on the inflow speed; a sharp increase in electric field is only obtained as the velocity entering the reconnection region approaches the Alfvén speed. The dynamics of the chromospheric case behave in a similar fashion to the coronal or photospheric case depending on the driver velocity.

The key parameters in determining the behaviour of the onset of reconnection are the plasma-β and the velocity inflow into the reconnection region. A lower plasma-β creates a larger change in the electric field signature of the reconnection event. A high plasma-β acts to hinder the reconnection, yielding a sharp rise in the electric field only when the velocity flowing into the reconnection region approaches the local Alfvén speed.

Chapter 2

Chromospheric resonantor

The first branch of this thesis consists of a numerical investigation of the behaviour of acoustic waves above a sunspot umbra. The steep temperature gradients at the photosphere and transition region allow waves to resonate in the chromospheric cavity. In this chapter, the behaviour of these waves is investigated for different chromospheric temperature profiles using a continuous random velocity driver of different colours. This work has been published as Snow et al. [2015].

2.1 Sunspot oscillations

On the surface (photosphere) of the sun, large concentrations of magnetic field form which are known as sunspots. A few hundred kilometres above and below the umbra, the atmospheric conditions vary massively such that below the umbra, the sound speed is greater than the Alfvén speed, and the opposite is true above the umbra. This makes the behaviour of waves above and around sunspots an interesting field of research. To quantify the atmospheric conditions, a plasma-β is defined as the ratio between the plasma pressure p and the magnetic pressure. In the corona, the magnetic pressure dominates so the plasma-$\beta \ll 1$. In the lower atmosphere, the gas pressure becomes larger and the plasma-$\beta \geq 1$.

Sunspots are capable of supporting three main types of oscillations: five-minute oscillations at photospheric levels, three-minute oscillations above the umbra, and running waves, moving away from the umbra along the penumbral structures [Bogdan, 2000, Bogdan and Judge, 2006]. In this research, waves above sunspot umbra are investigated hence the three-minute oscillations are of primary interest.

2.1.1 Observations of the three-minute oscillations

Following the work of Beckers and Schultz [1972], many papers have observed the three-minute oscillations above sunspot umbra. Marsh and Walsh [2006] observed these oscillations through both the 171 Å TRACE and the SOHO/CDS instruments. The three-minute oscillations have also been observed at the transition region in the microwave band as a modulation of gyroresonant emission [Shibasaki, 2001] and in ultraviolet wavelengths [De Moortel et al., 2006]. Furthermore, the three-minute waves have been found to dominate the spectra at heights between the photosphere and corona [Jess et al., 2012]. Thomas et al. [1987] observed multiple peaks in the three-minute band (4.5-10 mHz) from both space and ground instruments. A similar range of excited frequencies is present in Reznikova et al. [2012]. An overview of magnetohydrodynamic waves and coronal seismology can be found in De Moortel and Nakariakov [2012].

2.1.2 Origin of the three-minute oscillations

Despite the multitude of observations of the three-minute oscillations, there is still some controversy over the exact origin of these waves. There are three major models for explaining the origin of the three-minute oscillation that occur above sunspot umbrae.

2.1.2.1 Excitation of the cut-off frequency

Fleck and Schmitz [1991] suggested that the three-minute oscillations are due to a basic physical effect: the excitation of waves at the cut-off frequency. They numerically modelled a piston driving waves at the photosphere and a simplified isothermal atmosphere that ignored many complexities including temperature gradients and nonlinearities. The model produced three-minute oscillations. Fleck and Schmitz [1991] also investigated a VALC profile with similar results. Their explanation was that waves above the cut-off frequency are free to propagate upwards, increasing in amplitude, whereas waves below the cut-off frequency are damped. This is however, insufficient to explain the observed amplification of the three-minute oscillations [Stangalini et al., 2012].

2.1.2.2 Wake of a propagating shock

It has also been suggested that the three-minute oscillations arise from the wake of propagating shock waves, [Wilson, 1997]. These shocks are also present in the 1D numerical simulations of Bard and Carlson [2010]. However, 1D simulations of propagating shock waves leads to unrealistic shock merging [Ulmschneider et al., 2005]. Furthermore, many

observations show a harmonic wave structure [Reznikova et al., 2012, Sych et al., 2011, Yuan et al., 2011] as opposed to the saw-tooth signal required for the shock wave model.

2.1.2.3 Chromospheric resonator

An alternate explanation for the existence of three-minute oscillations above sunspot umbrae is the presence of an acoustic chromospheric resonator. Above the chromosphere in the transition region and below it in the photosphere, there are large temperature gradients that provide the semi-permeable boundaries necessary for resonances of slow magnetoacoustic waves to occur inside the chromosphere [Zhugzhda, 2008]. When a wave encounters these large temperature gradients, part of the wave is transmitted and part is reflected. We note that the model set-up in the previously mentioned models [Bard and Carlson, 2010, Fleck and Schmitz, 1991] prohibits any chromospheric resonator since the waves are driven using a piston at the photosphere. Zhugzhda [2008] also investigated how frequencies above and below the cut-off frequency behave in this resonator by using a temperature that changes non-monotonically with height. Waves above the cut-off frequency are partially reflected due to the sharp temperature gradients at the photosphere and transition region in the sunspot atmosphere. Waves below the acoustic cut-off frequency cause the chromosphere to resonate between the transition region and the point at which the cut-off frequency drops below the wave frequency [Taroyan and Erdelyi, 2008]. The resonances cause oscillations that leak energy through the transition region into the corona. This causes linear waves to travel into the corona. Botha et al. [2011] performed numerical simulations of a chromospheric resonator with a perturbation in the form of a single pulse. Two such pulses were considered, two and five minutes, propagating along a magnetic field line above a sunspot umbra. The results numerically proved the existence of an acoustic resonator in 1D and the production of the familiar three-minute oscillations.

2.2 Objective

The overall aim of this study is to investigate numerically the behaviour of a chromospheric resonator. Numerical simulations have been performed where perturbation noise is applied to the upper convection zone and allowed to propagate along the magnetic field line above a sunspot umbra. The wave trains will be interpreted as slow magnetoacoustic waves propagating with the local sound speed [Roberts, 2006]. The applied noise is of the form $1/f^{\xi}$, where ξ determines the colour of the noise. Pink noise ($\xi = 1$) corresponds to solar granulation noise [Rabello-Soares et al., 1997].

This chapter investigates the effect of different stochastic noise signatures on the chromospheric resonator. A 1.5D numerical investigation of a magnetic field line directly above a sunspot umbra was performed to simulate the effects of different noise signatures and chromospheric temperature configurations on the coronal frequency spectra. The findings indicate a novel method of chromospheric seismology, where the chromospheric temperature configuration can be estimated based upon the frequency spectra present in the wave trains that escape from the resonating chromosphere into the corona.

2.3 Methodology

2.3.1 Numerical methods

The ideal non-linear compressible MHD equations are implemented numerically using Lare2D, as presented by [Arber et al., 2001], see Section 1.3. These equations presented in Section 1.2 reduce to:

$$\frac{\partial \rho}{\partial t} = -\nabla \cdot (\rho \mathbf{v}), \tag{2.1}$$

$$\frac{\partial \mathbf{v}}{\partial t} + \mathbf{v} \cdot \nabla \mathbf{v} = \frac{1}{\rho}\mathbf{J} \times \mathbf{B} - \frac{1}{\rho}\nabla P + \mathbf{g}, \tag{2.2}$$

$$\frac{\partial \mathbf{B}}{\partial t} = -\nabla \times \mathbf{E}, \tag{2.3}$$

$$\frac{\partial \epsilon}{\partial t} + \mathbf{v} \cdot \nabla \epsilon = -\frac{P}{\rho}\nabla \cdot \mathbf{v}, \tag{2.4}$$

$$\mathbf{E} + \mathbf{v} \times \mathbf{B} = 0, \tag{2.5}$$

$$\nabla \times \mathbf{B} = \mu_0 \mathbf{J}, \tag{2.6}$$

$$P = \frac{\rho k_B T}{\mu_m}, \tag{2.7}$$

$$\epsilon = \frac{P}{\rho(\gamma - 1)}. \tag{2.8}$$

Here, $\mu_m = 1.4 m_p$ where m_p is the mass of a proton.

The normalisation values for length, magnetic field, and density are $L_0 = 150 \times 10^3$ m, $B_0 = 0.12$ T, and $\rho_0 = 2.7 \times 10^{-4}$ kg m^{-3}. The normalisation values are based on chromospheric values. Gravitational acceleration is constant as 274 m s^{-2} for the majority of the domain, however above approximately 44 Mm the gravitational acceleration is gradually reduced to zero on the upper boundary. This is to allow for the specification of an open boundary and prevent reflections from the upper boundary. The lower boundary is specified as a velocity driver. The side boundaries are periodic.

The velocities along a uni-directional magnetic field line above the umbra, perpendicular to the photospheric plane, are considered. The magnetic field acts as a waveguide for slow magnetoacoustic waves propagating into the corona (see Section 1.4.1 for numerical proof). These slow waves propagate parallel to the magnetic field at the acoustic speed, which is independent of magnetic field strength (see Section 1.4.1). This allows us to choose in our 1.5D model a constant magnetic field strength of 10 Gauss, in line with the chromospheric strength of a sunspot umbral magnetic field. This also justifies the assumption of ideal plasma since a constant magnetic field strength leads to $\mathbf{J} = 0$ and hence resistive terms are never present since they are of the form $\eta\mathbf{J}$ (see Section 1.2).

The full equations are solved in the three Cartesian coordinates (x, y, z) with y taken as the vertical direction. The numerical grid contains 1024 cells in this direction. The two horizontal directions (x, z) are invariant with periodic boundary conditions, making the simulation 1.5D. There are four cells in the invariant x direction. A convergence test of doubling the grid resolution in y resulted in no new features hence 1024 cells are deemed sufficient. The grid spans the range -68 Mm to 68 Mm, leading to a vertical cell size of 132,927 m. The photosphere is positioned at the centre of the computational domain at $y = 0$. The large domain size is used to prevent boundaries from interfering with the resonator. The end time of each simulation is set as 10^4 seconds.

The numerical dissipation in the code was tested by launching a slow pulse in a uniform plasma and analysing the amount of deformation that occurs to the pulse [e.g. Yuan et al., 2015]. The following range of values were tested: $\rho = 10^{-5}, 10^{-11}$, and 10^{-12} kg m^{-3} and $T = 0.4$ MK, and 1 MK. The maximum amplitude and full width at half maximum were consistent to four and seven significant figures, respectively when calculated at the start and end of the domain. Therefore the numerical algorithm used here is not significantly dispersive.

2.3.2 Noise

The resonator will be perturbed by applying random noise in the upper convection zone, 68 Mm below the photosphere. Granulation noise follows a $1/f^{\xi}$ distribution where the power is proportional to the reciprocal of the frequency [Rabello-Soares et al., 1997]. Three types of noise will be considered; white (uniform distribution), pink $(1/f)$ and brown $(1/f^2)$. This allows investigation into the effect of different perturbations. The velocity signal applied at the source is therefore of the form

$$v(t) = \sum_{n=0}^{m} a_n \sin(n\pi t + p_n) \tag{2.9}$$

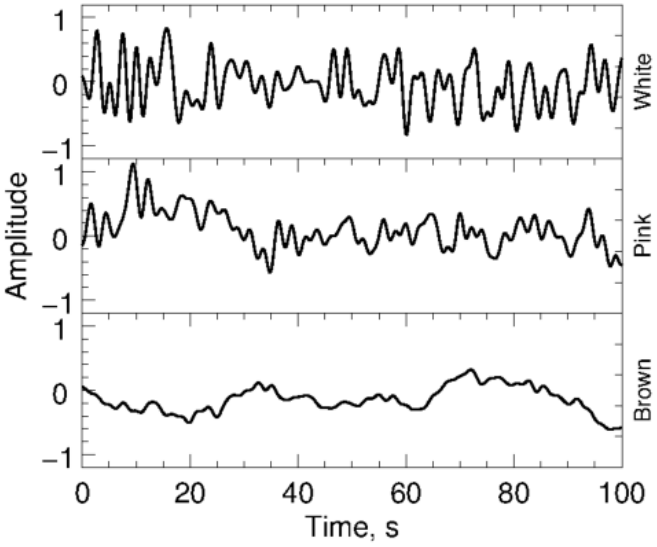

FIGURE 2.1: Example time series of the different noise sources, which are applied to the lower boundary as slow magnetoacoustic velocity perturbations.

where the constants a_n are determined by the noise colour and p_n is a random phase shift. m is the number of samples. For a perfectly resolved velocity signal $m = \infty$ however since this in not possible the number of sample is chosen as $m = 1024$.

White noise is the standard random noise where there is equal power in all frequencies. However since both pink and brown noise decline in power as the frequencies increase, these two are biased towards lower frequencies. Examples of the three types of noise are shown in Figure 2.1.

2.3.2.1 Generation of noise samples

It is of interest to determine the behaviour of the chromospheric resonator when driven by different frequency distributions. This section describes the process whereby noise sources with a specific power distribution can be generated.

Voss Algorithm One approach for generating pink noise was developed by Voss. This works by 'stacking' white noise such that the signal is biased towards the lower frequencies. Consider three dice: red, blue and green. Now the number of iterations is decided by the number of dice, $2^3 = 8$, which allows for numbers 000 to 111 in binary. Assign each dice to a column in the binary representation of the iteration number shown in Table 2.1.
Now the initial value is determined by the sum of the values on a roll of all three dice.

Iteration	red	blue	green
0	0	0	0
1	0	0	1
2	0	1	0
3	0	1	1
4	1	0	0
5	1	0	1
6	1	1	0
7	1	1	1

TABLE 2.1: Voss Algorithm Example

Between 000 and 001, only the value in the green column changes, therefore roll just this dice. The sum of the three dice is then the next value. Between 001 and 010, both the blue and green values change and hence roll both of these and the next value is the sum of all three dice. This continues until all iterations have been exhausted. The resultant signal is one of pink noise. This is due to the red dice representing a low frequency wave and the green dice representing a higher frequency wave.
It is obviously trivial to increase the number of iterations by increasing the number of dice, and replacing a dice with a white noise generator. This generates pink noise in an easy to understand and efficient manner however is difficult to expand for noise of different distribution, for example Brownian.

Filtering A more versatile way to generate noise of a chosen distribution is to generate a white noise signal then filter the spectra to have the desired distribution. The steps for this are given below:

1. Generate a white noise sample
2. Convert signal to spectral space using a FFT
3. Multiply the spectra by the desired frequency distribution
4. Convert the signal back to physical space

This is a very simple and versatile way to generate noise of a desired colour. The signal can then be smoothed and interpolated to create the velocity signal. At this stage, it is necessary to confirm that the new signal has the desired power spectrum. This is done by performing an FFT on the new signal and confirming that it is within acceptable bounds (± 0.1) of the target gradient. The main downside is that the process becomes computationally expensive to generate a signal resolved to high frequencies.

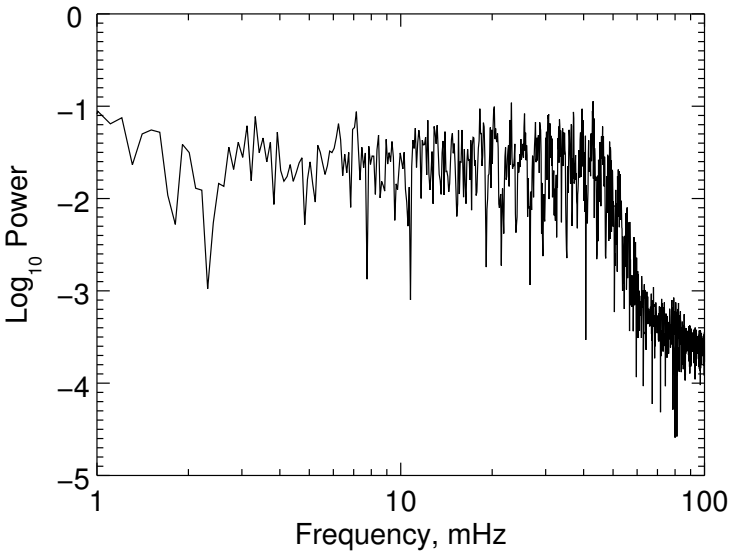

FIGURE 2.2: Example spectrum for a generated white noise sample. The noise is resolved to approximately 50 mHz. After this point the power rapidly drops for higher frequencies.

The filtering method was used to generate the noise samples used in this research due to its versatility.

2.3.2.2 Velocity initialisation

The filtering method was used to generate the noise samples used in this research due to its versatility. Due to the stochastic nature of noise, multiple samples of each colour were tested to ensure reliable conclusions can be deduced. To have a fully resolved spectrum would require infinite random values to be generated at the initial stage. However, this is not possible. Here 1024 random numbers are used and the signal is well resolved up to approximately 50 mHz. A signal resolved to a higher frequency, 100 mHz, was tested. There was no difference in the results and the lower cut-off is used throughout this paper, i.e. 50 mHz. An example of the frequency spectrum for white noise is given in Figure 2.2. The velocity is scaled to be between ± 1 m s^{-1} at the lower boundary, 68 Mm below the photosphere, allowing for the consideration of small perturbations. The largest Mach number obtained in the simulation is approximately 0.4.

2.3.3 Temperature Profiles

The coronal temperature profile is obtained from the VALC model by Avrett and Loeser [2008], with the chromospheric temperature being replaced by the investigated profiles.

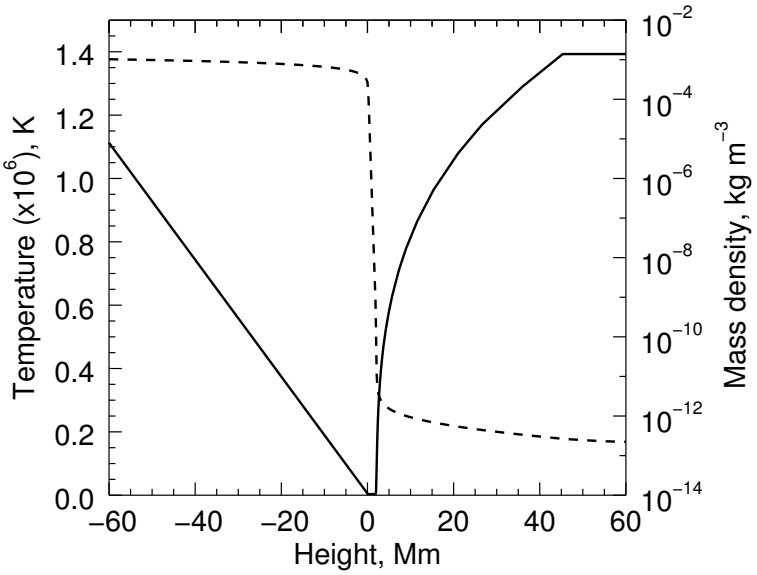

FIGURE 2.3: Initial temperature (solid line) and density (dashed line) profiles used in the simulation. The photosphere is located at height 0.

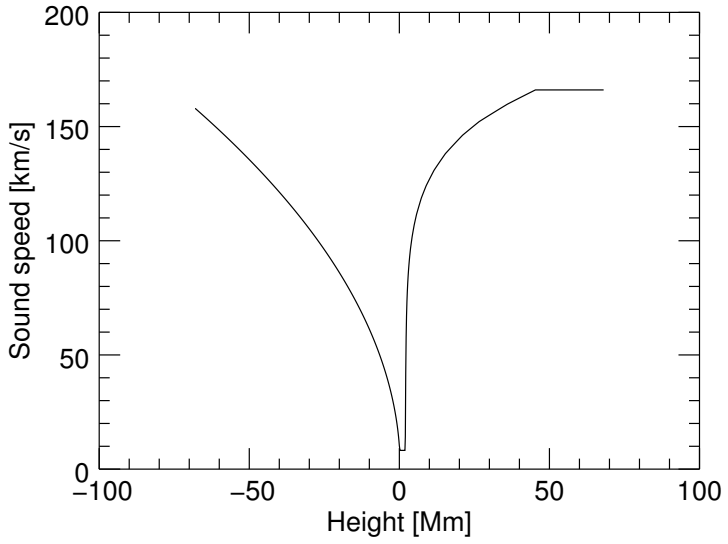

FIGURE 2.4: Sound speed corresponding to the domain in Figure 2.3

To prevent velocity perturbations being reflected from the upper boundary, it is necessary that the temperature gradient at the top of the computational domain is zero. Therefore, from approximately 44 Mm above the photosphere and higher the temperature is flattened. This has no effect on the simulation results and the data are investigated at points below this region. The temperature profile is shown in Figure 2.3.

For the convection zone, a polytrope temperature profile is used. The lower velocity boundary is specified directly from the input noise seed. By setting the lower boundary

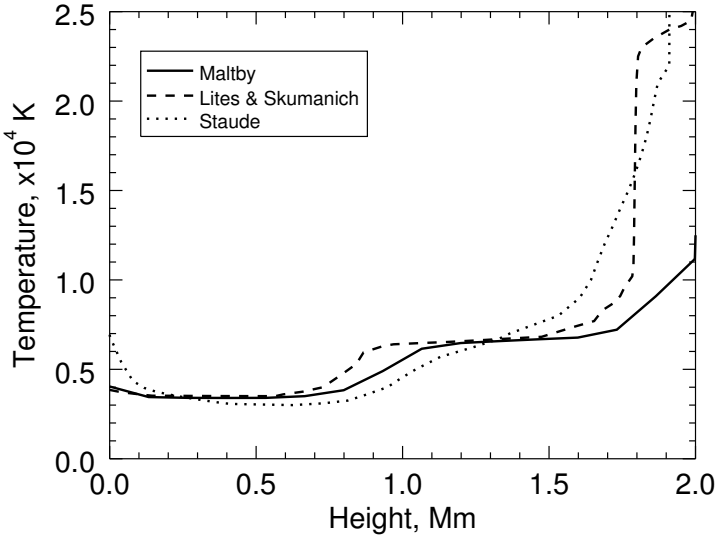

FIGURE 2.5: Different theoretical temperature profiles for the chromosphere above a sunspot: solid line from Maltby et al. [1986], dashed line from Lites and Skumanich [1982], and dotted line from Staude [1981].

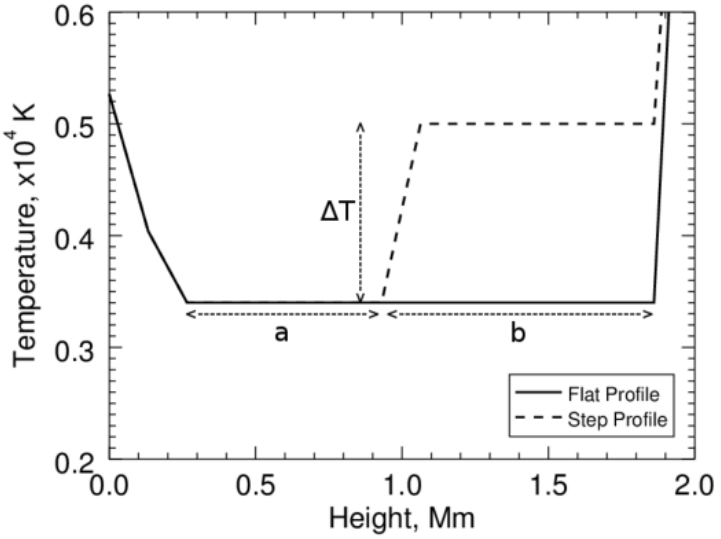

FIGURE 2.6: Flat and step chromospheric temperature profiles with the photosphere at 0 and the transition region at 1.8 Mm. This chromospheric profile is shown in relation to the photospheric and coronal temperature profiles in Figure 2.3. In the step profile, ΔT changes over two grid cells. The step profile is a simplification of the theoretical temperature models shown in Figure 2.5.

far away from the resonator, downwards propagating waves are damped due to the increasing density towards the boundary and do not reflect from the lower boundary. Upward-propagating waves increase in amplitude due to the decreasing density. Note that whilst we refer to this region as the convective zone, there are no convective motions in the simulation.

There are several theoretical models available for the structure of the chromosphere above a sunspot [Lites and Skumanich, 1982, Maltby et al., 1986, Staude, 1981] as shown in Figure 2.5. These theoretical models suggest that the chromospheric cavity size is between 1.5 and 1.8 Mm. Here two profiles are investigated, a flat and a step profile (Figure 2.6) and they have a chromospheric cavity size $a + b$. In the numerical model, a is the size of the lower chromospheric temperature plateau and b is the size of the upper chromospheric temperature plateau. The flat profile allows for consideration of an idealised scenario, whereas the step profile is closer to the theoretical models with a lower and an upper chromospheric temperature plateau, as well as a temperature jump at the mid-chromosphere.

At both the photosphere and transition regions there is a steep temperature gradient, as can be seen in Figures 2.3, 2.5 and 2.6. These act as semi-permeable boundaries that allow energy to be partially reflected and partially transmitted. The energy partially reflected back into the chromosphere results in resonance in the chromospheric cavity that exists between the photosphere and transition region [Botha et al., 2011, Zhugzhda, 2008].

In Botha et al. [2011], where a single pulse was used to energise the chromospheric cavity, the resonator found its natural frequencies. In the present study, a continuous noisy source of energy enters the chromospheric cavity. This results in a broad energisation of a range of frequencies, as will be discussed in Section 2.5. In addition, energisation is caused by the partial reflection and partial transmission of the energy content at the photosphere and at the transition region.

Multiple simulations were performed, varying the chromospheric cavity size and velocity source. This changes the energy content and energy distribution of the oscillations present in the resonator.

2.4 Transmission into the corona

The behaviour of the velocity perturbations at different points in the solar atmosphere is shown in Figures 2.7, 2.8 and 2.9. Figure 2.7 shows a snapshot of the velocity across the domain. Below the photosphere the velocity is too small to be seen on the plot. However

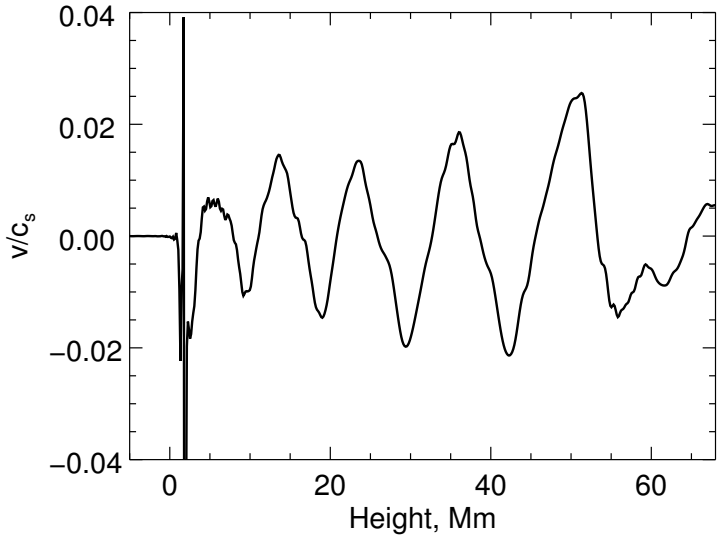

FIGURE 2.7: Snapshot of the evolution of velocity across the domain at one time instance. The source is located at −68 Mm and the photosphere is at 0 Mm. Large amplitude velocity is present in the chromosphere due to the high energy content of the resonating cavity. Wave trains propagating into the corona are reasonably well structured. Time evolution of velocity at different points is shown in Figure 2.8. For this plot a flat chromospheric temperature profile of depth 1.8 Mm was used with a white noise velocity source.

there are wave trains propagating both towards the resonator, from the velocity source applied at the lower boundary, and away from the resonator towards the lower boundary, due to downwards partially transmitted velocity perturbations.

A time series of the velocity perturbations measured at a point in the lower and upper chromosphere is shown in Figures 2.8 and 2.9. The wave trains propagating into the corona appear well structured, i.e. well resolved with no shocks forming, with several higher frequencies present. This is reflected in the frequency spectra.
Figure 2.8 shows the time evolution of the velocity at different spatial points. The velocity amplitude, with respect to the local sound speed, increases throughout the chromosphere. When energy is transmitted through the temperature boundary at the transition region, there is a decrease in power since the energy is partially reflected back into the chromosphere. Again the signal appears to be mostly regular with several higher frequencies present, identifiable from the small scale fluctuations. Note that the two coronal figures, (a) and (b) in Figure 2.8, show the same velocity perturbation shifted by time. This shows that once the signal has entered the corona, there are no significant changes to the velocity perturbation. There is no evidence of any shocks occurring and the signal is well resolved. The frequency regimes discussed in Section 2.5 are all present when sampled at various points in and above the transition region.

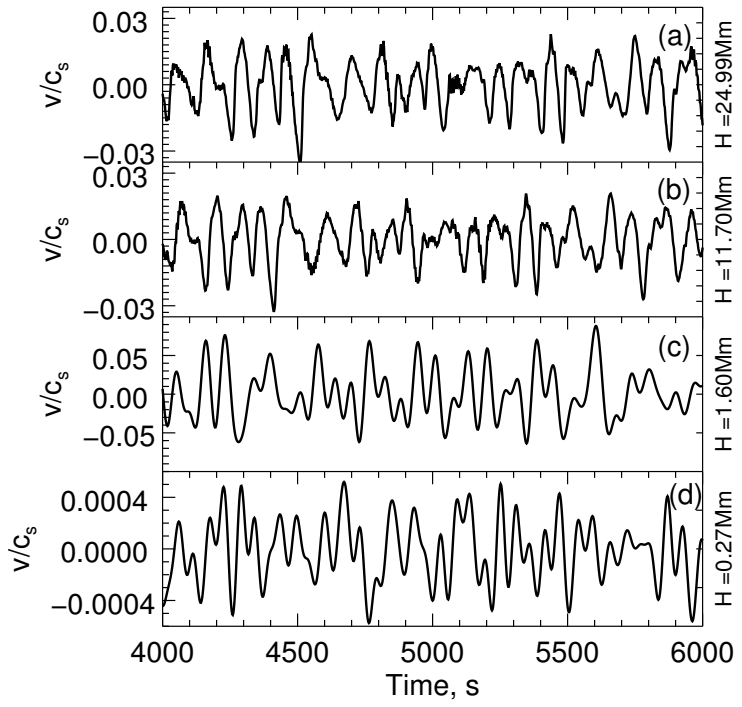

FIGURE 2.8: Plots of velocity/sound speed vs time for different heights H above the photosphere. (a) and (b) are in the corona, (c) is located in the upper chromosphere, (d) in the lower chromosphere. The model set up for this plot was a flat chromospheric temperature profile of depth 1.8 Mm with a white noise velocity source.

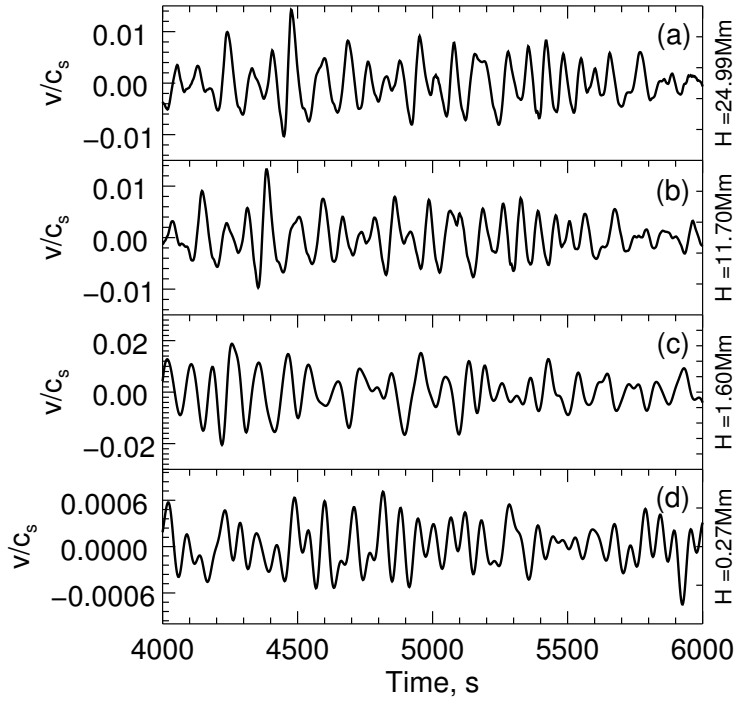

FIGURE 2.9: Plots of velocity/sound speed vs time for different heights H above the photosphere. (a), (b), (c) and (d) are at the same locations as in Figure 2.8. A step temperature profile was used with $a = b = 0.9$ Mm for both the upper and lower plateaux. The perturbation noise was white.

2.5 Coronal frequency regimes

An FFT was performed to analyse the frequencies present in the corona for each simulation. This involved considering the time series velocity fluctuations through a single point in space. A line has then been fitted to the FFT to quantify the relation between power and frequency using the well established method of least squares. The gradient of this line is then used to consider the effect the chromospheric temperature configuration has on the signal propagating through the corona. Velocity data are sampled at intervals of 0.25 seconds, leading to a Nyquist frequency of 2000 mHz.

The frequency for each simulation is sampled through time in the corona at a point 25 Mm above the start of the transition region. Four main regions are observed in the spectra for all the simulations, as shown in Figures 2.10 and 2.11 for the flat and step profiles respectively; all except the lower cut-off frequency are due to the resonating behaviour. There is a general trend of increased spectral power for larger chromospheric cavities. This is expected since there is a larger region for the resonances to oscillate in, which provides increased amplitude and hence higher power. Note also that there is a level of uncertainty present in the data due to the fact that the system is being driven by stochastic noise. This arises because the noise is generated using a finite number of samples resulting in slight deviations from the expected power at each frequency. At double the grid resolution, the four regimes were still present at the same frequencies.

Region I: Lower Cut-off Below approximately 4 mHz there is a very low power region (Figure 2.10, region I). This is due to the acoustic cut-off frequency ω_c that allows waves to propagate upwards with frequencies

$$\omega > \omega_c = \frac{c_s}{2H}\sqrt{1 + 2\frac{\partial H}{\partial z}} \tag{2.10}$$

where $H = c_s^2/(\gamma g)$, γ is the ratio of specific heats, c_s is the sound speed, and z is the height [Lacoste, 2004]. Typical values of the acoustic cut-off frequency are in the range 3.5 - 5.2 mHz [e.g., Bel and Leroy, 1977, McIntosh and Jefferies, 2006, Yuan et al., 2014].

See Section 1.4.2 for derivation.

Region II: Broad Peak Between approximately 4 and 17 mHz the power is relatively flat (Figure 2.10, region II). This corresponds to a broad band of frequencies with oscillation times of between approximately one-minute to four-minutes. Following the work of Beckers and Schultz [1972], several papers have investigated the three-minute oscillations above sunspot umbra. For example, Reznikova et al. [2012] present spectra for

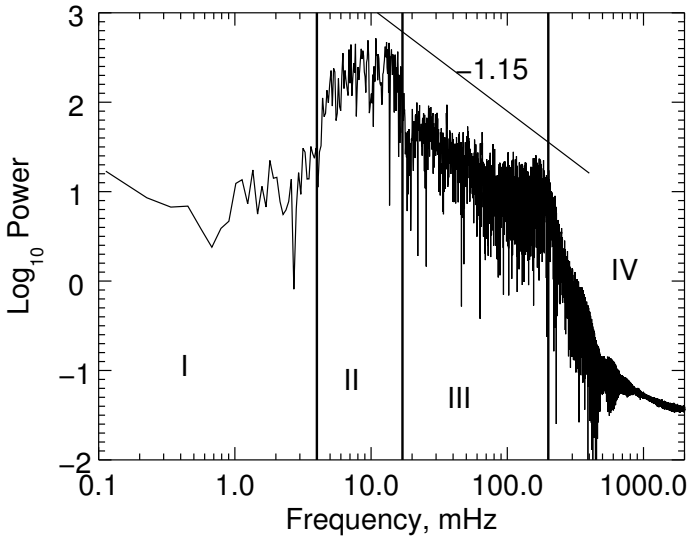

FIGURE 2.10: Four frequency regimes present in the spectra. I is the lower cut-off due to the acoustic cut-off frequency (below 4 mHz). II is the broad peak (4-17 mHz). III is the gradient decline (17-200 mHz). IV is the upper cut-off (above 200 mHz). This spectrum was generated for a flat chromospheric profile of depth 1.8 Mm with a white noise velocity source. The line indicates the gradient of the power in region III, which is -1.15 in this case.

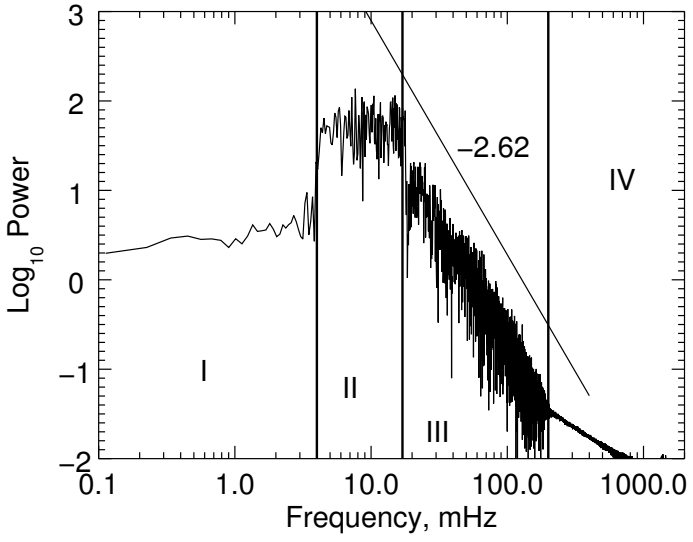

FIGURE 2.11: Four frequency regimes present in the spectra. Regions I, II, III and IV are the same as in Figure 2.10, generated for a step chromospheric profile with upper and lower plateau depths of $a = b = 0.9$ Mm and a white noise velocity source. ΔT is 2600 K. The line indicates the gradient of the power in region III, which is -2.62 in this case.

oscillations above sunspot umbrae through various filters which show an excited range of frequencies between approximately 6-8 mHz. Thomas et al. [1987] makes reference to a three-minute band of frequencies between 4.5 and 10 mHz containing multiple peaks.

This broad peak is present in the same frequency range regardless of temperature configuration or perturbation noise. No discrete harmonics are visible in the spectra. This does not mean that the harmonics are not present; they are not visible due to the power distribution in the frequency range where the harmonics are situated.

Region III: Gradient Decline The next region (Figure 2.10, region III) between 17 and 200 mHz, is a region where the power is proportional to $1/f^{\alpha}$, which corresponds to a linear decline of gradient α when plotted on log-log axes. This region is found to vary in gradient when the temperature profile is modified and provides the diagnostic tool for the main conclusions drawn in this paper. This is discussed in more detail in the Sections 2.6.1 and 2.6.2. Confidence intervals were calculated to ensure the fitted line was representative of the data. The standard deviation was small in all cases, ranging from 0.041 to 0.052, resulting in very narrow confidence intervals, identical to 3 decimal places. For one such line, the 95% confidence interval is -0.9649 to -0.9646, with the calculated value being -0.9647.

Region IV: Upper Cut-off Above approximately 200 mHz (Figure 2.10, region IV) the power drops significantly. The cut-off prevailed at the same frequency with a higher resolved input signal indicating that this upper cut-off is due to neither the input signal (Section 2.3.2) nor the sampling rate (Section 2.5). This is a fluid model which does not account for the ion-gyrofrequency. However the ion-gyration frequency is approximately $\Omega_i = 9.6 \times 10^4$ rad s^{-1} [Priest, 2014]. This is far larger than the frequencies simulated in this model, therefore the obtained frequencies are not beyond the physical limitations of the fluid model. This suggests a physical phenomena for the upper cut-off unidentified at present. Due to the high frequency where the cut-off occurs, it cannot be resolved in observations at the present time. It may also be due to numerical dissipation; higher frequency waves should be damped more.

2.6 Varying the chromospheric temperature configuration

2.6.1 Flat Profile

Initially the temperature configuration of the chromosphere was assumed to be uniform, as shown in Figure 2.6 with $\Delta T = 0$. This was to investigate the behaviour in an

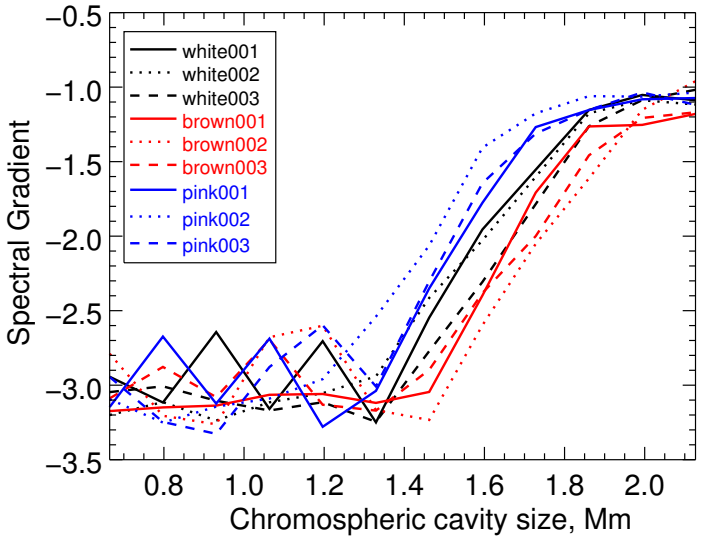

FIGURE 2.12: Gradients vs chromospheric cavity size for three samples of each noise colour. The gradients were obtained in region III of Figure 2.10.

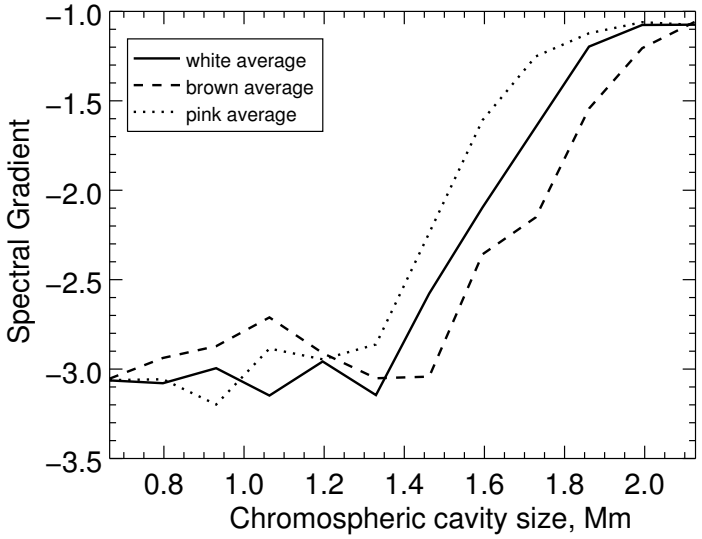

FIGURE 2.13: Gradients vs chromospheric cavity size for three samples averaged across each noise colour. The gradients were obtained in region III of Figure 2.10.

idealised scenario. Here the parameter space consists of the chromospheric cavity size ($a+b$ in Figure 2.6) and the perturbation noise colour. Three noise samples for each noise colour were used and a range of chromospheric cavity sizes between 0.66 and 2.13 Mm were tested. The gradient of the aforementioned frequency range (Figure 2.10, region III) was calculated for each simulation. Note that due to the stochastic nature of noise, different samples of the same noise colour create slightly different results, indicated by the variations present in Figure 2.12. Multiple seeds were tested for this reason.

For clarity, the gradients were averaged for each noise colour and are shown in Figure 2.13. This effectively removes some of the uncertainty present when considering noise. The full set of results is shown in Figure 2.12, showing the extent of randomness. The variation in the gradient is approximately ± 0.5 for narrow chromospheres of cavity size less than 1.3 Mm, whereas for large chromospheres of cavity size larger than 1.8 Mm there is virtually no variation in gradient across samples.

For narrow chromospheric cavities, less than 1.3 Mm, all three noise colours appear to have the same output gradient in their spectra, as shown in Figures 2.12 and 2.13. There is a sharp change in output gradient for chromospheric cavity sizes starting from around 1.3-1.4 Mm and ending at approximately 1.8 Mm. Here the gradient rapidly goes from steep, $\alpha \approx -3$, to relatively flat $\alpha \approx -1$. Since this large change in gradient is present, it may be possible to estimate the depth of the chromosphere from the spectra sampled in the corona at 25 Mm above the transition region.

The dependence of the power gradient on the chromospheric cavity size can be explained by considering the energy content of the chromosphere. As the chromospheric cavity size increases, the total energy content of the resonating waves increases. This allows for energy to be more evenly distributed among the higher frequencies when partially transmitted into the corona. For a thinner chromosphere, there is a low total energy content and as such only the lower frequencies become energised. As the chromosphere cavity increases in size, the energy content increases and there is more energy in the higher frequencies, relative to the lower frequencies, i.e. a decrease in the slope of the power gradient in the FFT spectra (Figure 2.13).

With regards to noise, there does not appear to be a significant difference between noise colours. Whilst the location of the sharp gradient change in the spectra measured for narrow chromospheres appears slightly different in Figure 2.13 for different noise colours, there is no distinct relationship and the variation in the location of the sharp change is small, occurring between approximately 1.3 and 1.4 Mm of chromospheric thickness. Therefore the discrepancy is most likely due to the stochasticity present.

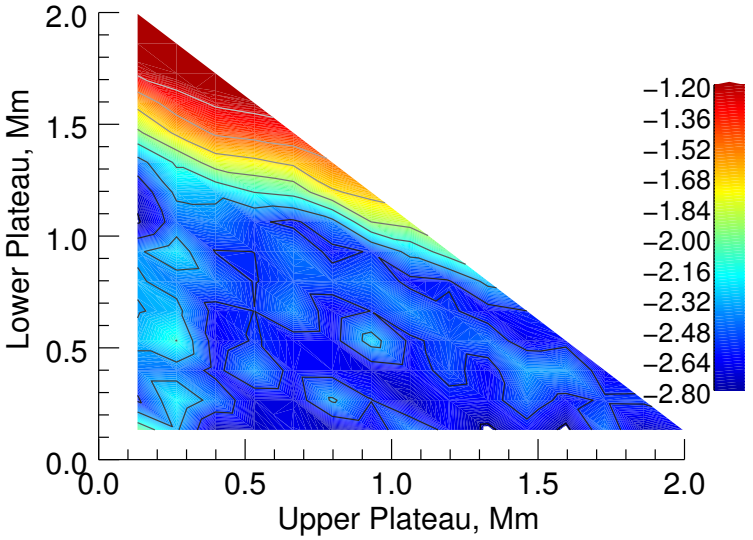

FIGURE 2.14: Contours of the gradient in the obtained coronal spectra (region III of Figure 2.10) generated by white noise and the step temperature profile. The lower plateau sizes are given by values of a and the upper plateau sizes by b in Figure 2.6. The black marker on the vertical axis indicates the steep gradient change for the flat profile, as seen in Figure 2.13.

For large chromosphere depths, above 1.8 Mm, the output gradient becomes fairly constant for all three noise colours, as shown in Figures 2.12 and 2.13.

2.6.2 Step profile

Next, the chromospheric temperature configuration is replaced with a step profile. This consists of two uniform temperature regions or plateaux, a and b, separated by a small linear temperature jump, ΔT, that occurs over 2 grid cells as shown in Figure 2.6. This is similar to theoretical chromospheric temperature models (Figure 2.5) and provides a more realistic configuration. Thus the parameter space here consists of 4 variables: lower plateau size a, upper plateau size b, temperature jump ΔT, and noise colours. In this section, the temperature jump will be fixed at 2600 K since this agrees with the theoretical models (Figure 2.5). Varying the temperature jump will be investigated in Section 2.6.3.

The depth of both the lower (a) and upper (b) plateau varied in the range 0.13 Mm $\leq a, b \leq$ 2.0 Mm, under the constraint that the total depth 0.8 Mm $\leq a + b \leq$ 2.13 Mm. This provides a maximum total chromospheric cavity size of approximately the largest value from the theoretical models, i.e. 2 Mm as shown in Figure 2.5. The minimum chromospheric cavity size is 0.8 Mm. The three types of noise were used as in Section 2.6.1, however on this occasion only one sample of each colour was used. The gradient

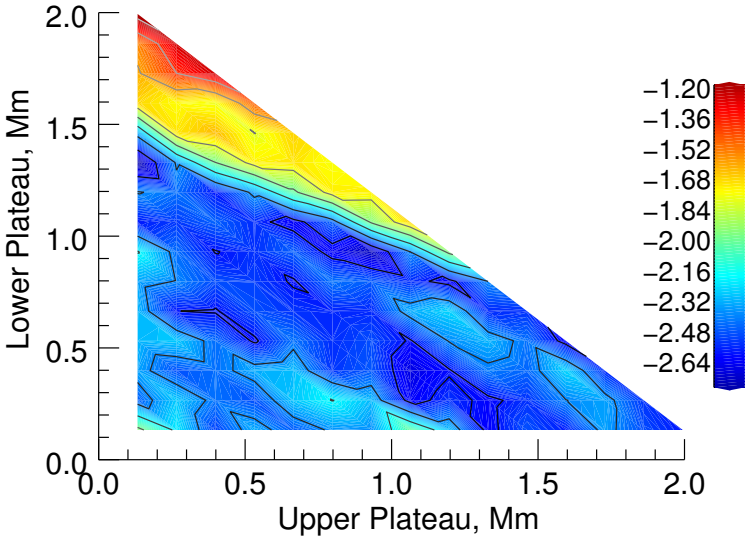

FIGURE 2.15: Contours of the spectral gradient for different temperature profiles when driven by brown noise. Plot configuration is the same as in Figure 2.14

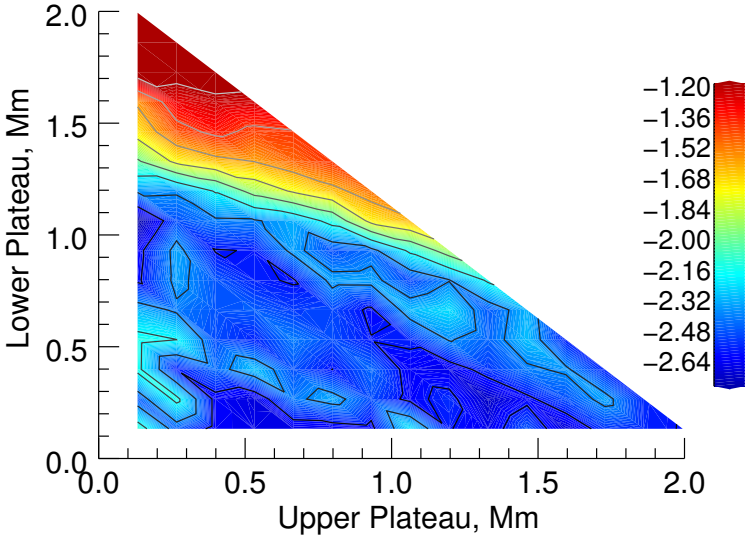

FIGURE 2.16: Contours of the spectral gradient for different temperature profiles when driven by pink noise. Plot configuration is the same as in Figure 2.14

of the coronal spectra was calculated as before in region III of Figure 2.11. The results can be seen in Figures 2.14, 2.15 and 2.16 for white, brown and pink noise respectively.

A similar trend is present here as with the flat profile: there is a steep change in spectral gradient between two regions of near-constant spectral gradient, as shown in Figure 2.13. The location of the steep gradient change in Figures 2.14, 2.15 and 2.16 is independent of the noise source. An interesting feature is that the location of the steep spectral gradient change varies with plateau sizes. The location of the sharp change approximately follows the equation $a = -0.5b + 1.5$ for lower plateau size a and upper plateau size b. As the size of the upper plateau (b) increases, the size of the lower plateau (a) required for the sharp gradient change decreases but at a slower rate. This implies that the dimension of the lower plateau a is more important in producing this steep change than the dimension of the upper plateau b. The marker on the vertical axis in this plot indicates the location of the steep change for the flat profile.

For a small lower plateau , there is near constant spectral gradient, similar to the results from the flat profile, Figure 2.12. In Figure 2.14 there is some variation present which is due to the stochastic element of these simulations. One would expect that averaging over several samples of the same noise colour would result in a smoother result, as with the flat profile, Figure 2.13.

As in the case of the flat profile, there is very little difference in the location of the sharp gradient change between the results for different noise colours. Any discrepancies are of the same order as those found for the flat profile (Section 2.6.1). It can be seen that the trend for the flat profile (Figure 2.13) continues the trend present for the step profile, Figures 2.14, 2.15 and 2.16.

2.6.3 Varying the mid-chromospheric temperature jump

A set of simulations was performed to investigate the importance of the temperature jump ΔT between the two uniform regions. For this, only a few chromospheric cavity sizes were tested, 0.6 Mm $\leq a + b \leq$ 1.2 Mm, and three temperature jumps were considered: $\Delta T = 1600$, 2600 and 3600 K. The results are shown in Figure 2.17. There appears to be no significant difference between the temperature jumps, indicating that the variable ΔT is less important than the total chromospheric cavity size $a + b$.

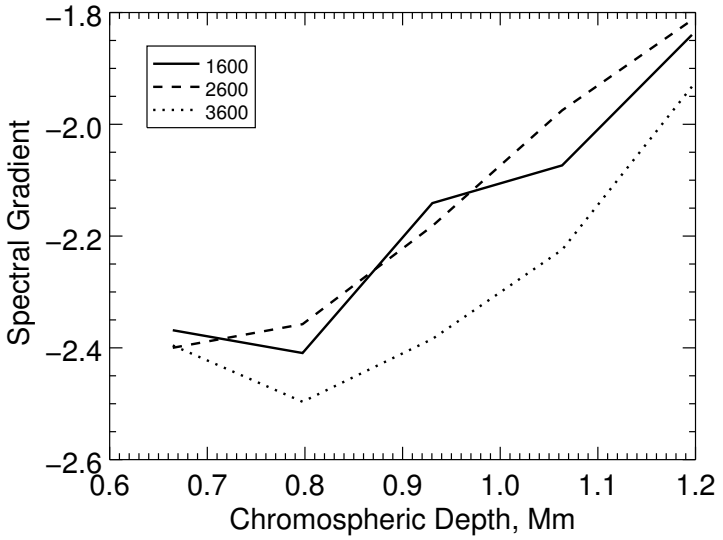

FIGURE 2.17: Gradients of the spectra (Figure 2.10, region III) obtained with different temperature jumps at the mid chromosphere, i.e. with different values of ΔT as shown in Figure 2.6: 1600K, 2600K, 3600K. The chromospheric cavity size $a+b$ increases with $a = b$.

2.7 Chromospheric seismology

The steep change in spectral gradient can be clearly seen in Figures 2.10 and 2.11. Regions I and II in these figures are very similar. The diagnostic in this paper is demonstrated by considering region III of these two plots. In Figure 2.10 the chromospheric temperature profile leads to a shallow gradient, whereas the temperature configuration in Figure 2.11 leads to a steep gradient. One can clearly see the stark differences between these two plots for region III.

The results obtained give rise to a new potentially useful diagnostic for chromospheric temperature configurations. Given the velocity spectra in the corona, it is possible to give upper and lower limits to the chromospheric cavity size. This diagnostic arises from the presence of the steep change in gradient present in all cases considered here, visible in Figures 2.13 and 2.14. For example, consider a case where the spectral gradient is steep. From Figure 2.14 it can be seen that the size of the chromospheric cavity is bounded above by the steep gradient change, which follows the line $a = 0.5b + 1.5$. This implies limits on the size of the lower plateau $0 \leq a \leq 1.5$ Mm and upper plateau $0 \leq b \leq 3$ Mm, subject to the constraint that $a + 0.5b \leq 1.5$.

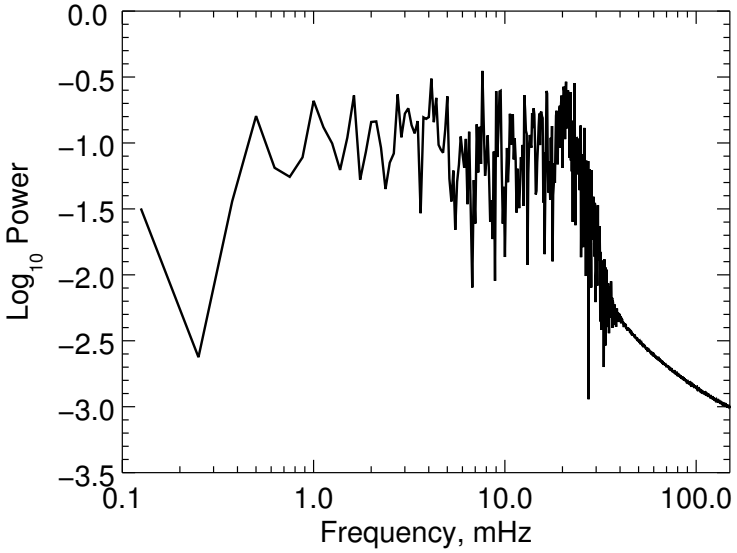

FIGURE 2.18: Frequency spectrum sampled at the photosphere, i.e. at height 0.

2.8 Spectral shape and its height above the photosphere

In addition to the spectra in the corona, the photospheric spectra were also analysed for white noise. There is a reasonably flat spectra followed by a sudden drop at approximately 20 mHz, as shown in Figure 2.18. Again this sudden drop in power was found to be independent of the input wave resolution. A possible explanation for this is that the downwards propagating waves due to the resonator dwarf the driven upward waves in power at this point. Note that this does not mean the upward propagating waves are not present, merely that they are not obvious in the FFT since the waves propagating from the resonator are far more powerful.

2.9 Conclusions

This chapter investigated numerically the oscillations above sunspot umbrae. The velocity perturbations drive a resonating temperature cavity between the photosphere and transition region. Multiple simulations were performed where both the chromospheric temperature profile and perturbation noise were varied. The resultant coronal velocity signature was then analysed. Different colours of noise were found to have very little effect on the output spectra. However, a strong trend is present where the gradient in the frequency spectra of the coronal velocity perturbations varies with regards to chromospheric cavity size: as the chromosphere cavity increases in size, the spectral gradient becomes shallower.

The coronal spectra can potentially be used as a diagnostic for the chromospheric cavity size. The sharp change in gradient present in Figures 2.13, 2.14, 2.15 and 2.16 allows for limits to be estimated for the sizes of the lower and upper uniform temperature regions or plateaux (a and b in Figure 2.6). These limits can be further reduced by estimating a maximum and minimum total chromospheric cavity size ($a + b$).

It is inherently difficult to measure the chromospheric cavity size directly. This work provides a solution by analysing the coronal waves above sunspots for different chromospheric cavity sizes via a numerical simulation. The results presented in this chapter show that the gradient of the coronal frequency spectra is directly correlated with the chromospheric cavity size. Thus, a novel diagnostic was presented for indirectly estimating the chromospheric cavity size above sunspot umbrae for the Sun and other stars.

Chapter 3

Line-of-sight integration

3.1 Resonance

The first application of LOS integration is on the chromospheric resonances presented in Chapter 2. The resonances produced a coronal velocity signature, on which LOS integration is performed to investigate the observational signatures in the corona created as a result of the chromospheric resonances above sunspot umbrae.

Here, the simulations are 1.5D so the LOS integration is performed along a line producing a single value at each time. The intensity is calculated using the following equation:

$$I = \int_a^b R(T) n_e^2 dy, \tag{3.1}$$

where I is the resultant line intensity, n_e is the number density, $R(T)$ is the thermal response function for temperature T, and y is the length along the line. The SDO/AIA response functions were generated using version V6 available in ssw-idl [Boerner et al., 2012]. Note that the simulation mass density ρ is proportional to the electron number density n_e.

This integration was performed from the transition region to the corona. This was performed numerically using the trapezium rule. The temporal resolution here is one sample every two seconds. This corresponds to a Nyquist frequency of 250 mHz. The response function is recalculated at each time step to account for temperature fluctuations. The integration was performed with a lower bound as the start of the transition region to remove the chromospheric foot-point. Only the flat profile driven by white noise has been considered. The line-of-sight integration was performed for chromospheric cavity sizes between 0.66 and 2.13 Mm.

3.1.1 SDO/AIA response functions

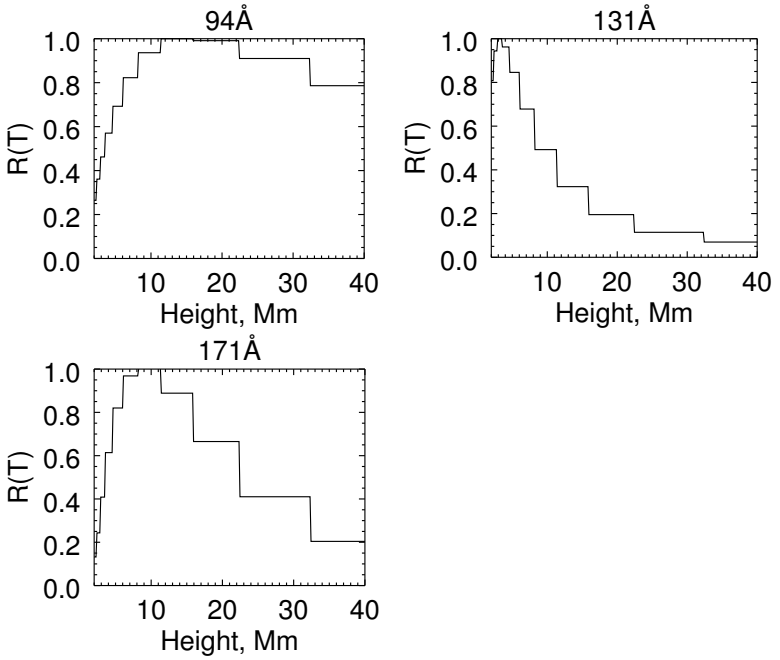

FIGURE 3.1: Normalised response function $R(T)$ plotted against height using three SDO/AIA filters at time $t = 0$. This is recalculated at each time iteration for the LOS integration to account for temperature variations. The corresponding initial temperature profile is shown in Figure 2.3.

The initial response function $R(T)$ as a function of height is shown in Figure 3.1 for three SDO/AIA filters (94, 131, and 171 Å). The SDO/AIA response functions were generated using the most recent version V6 available in ssw-idl [Boerner et al., 2012]. LOS integration was performed on the three samples of white noise, varying the chromospheric cavity size between 5 and 2.13 Mm for the three SDO/AIA filters shown in Figure 3.1. The three SDO/AIA filters give similar results, hence we only discuss the behaviour for the 171 Å channel. The wave structure does not change in the corona (Figure 2.7) so different spectral lines produce similar intensity spectra in the corona.

Figure 3.2 shows the resultant frequency spectra of the line intensity using the 171 Å filter for chromospheric cavity sizes of 0.66, 1.20, 1.60 and 2.13 Mm. The spectra demonstrate the acoustic cut-off for frequencies less than 4 mHz, similar to the spectra obtained from a point source (Figures 2.10 and 2.11, region I). As the chromospheric cavity size increases, the power of the underlying noise becomes less dominant and the highest frequency in the excited range decreases. In other words, the bandwidth containing the excited frequencies becomes narrower. For example, in Figure 3.2 the excited range of frequencies for a chromospheric cavity size of 1.595 Mm is between approximately 4 and 18 mHz whereas for a chromospheric cavity size of 2.127 Mm the range is between 4 and 13 mHz.

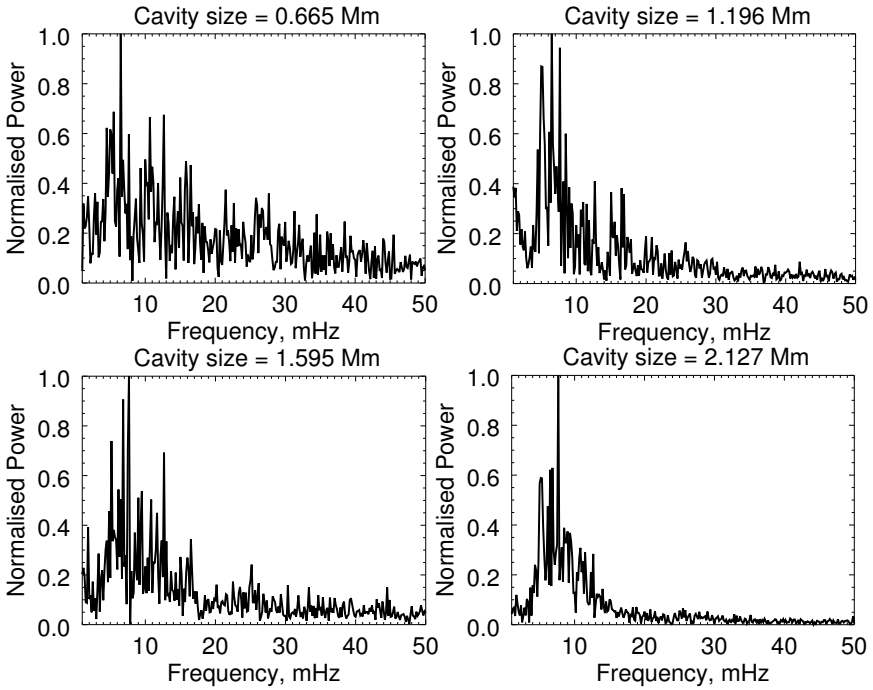

FIGURE 3.2: Line of sight integration of the coronal velocity perturbations for 171 Å for four different sizes of the chromospheric cavity. The power spectra are normalised to their respective maximum values for chromospheric cavity sizes (a+b in Figure 2.6) of the temperature profile given by 0.67, 1.20, 1.60 and 2.13 Mm respectively.

A line of the form $1/f^{\alpha}$ can be fitted to the LOS spectra in the range 20-50 mHz, with α representing the log-log gradient. For the single point analysis there was a trend present where the gradient depended on the chromospheric cavity size. However only a weak trend is present in the gradients for the 94 and 171 Å filters. No discernible trend was present for the 131 Å filter. Variations in α between different samples of white noise are large with respect to the total change in α. Therefore it would be difficult to accurately determine the chromospheric cavity size given α.

3.1.2 Narrow band contribution functions

Four narrowband lines which are observable by Hinode/EIS were tested: Mg V (276.58 Å), Si VII (275.36 Å), Fe X (184.54 Å), and O V (248.46 Å). Furthermore, two SOHO/-SUMER lines were tested: Ne VIII (770.84 Å) and Mg X (624.97 Å). The lines were generated using Chianti V7 [Dere et al., 1997, Landi et al., 2013] and the generated contribution function $C(T)$ was used in place of $R(T)$ in Equation (3.1). There was still no quantitative trend present in the resultant spectra. The contribution function $C(T)$ using Hinode/EIS and SOHO/SUMER for the initial temperature profile can be seen in Figures 3.3 and 3.4.

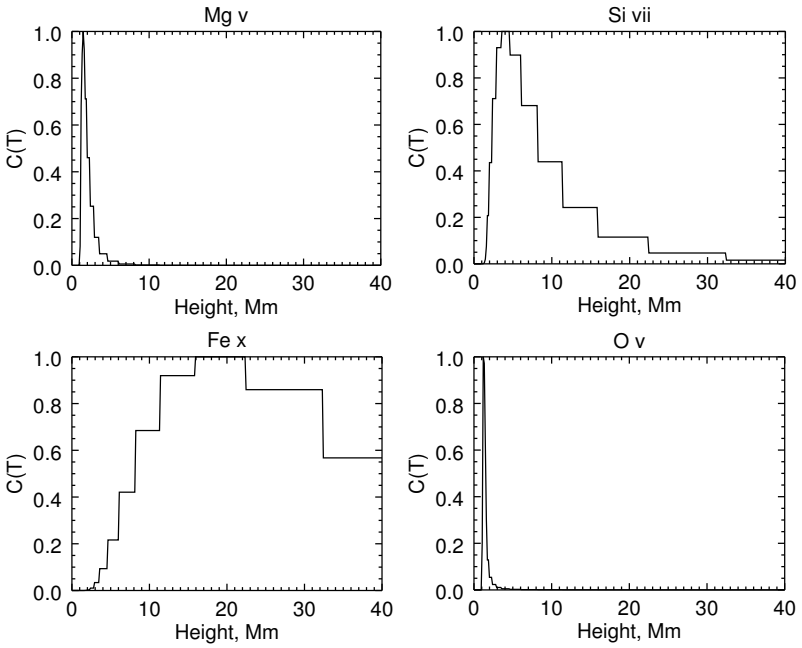

FIGURE 3.3: Normalised contribution function $C(T)$ plotted against height using for Hinode/EIS filters at time $t = 0$. This is recalculated at each time iteration for the LOS integration to account for temperature variations. The corresponding initial temperature profile is shown in Figure 2.3.

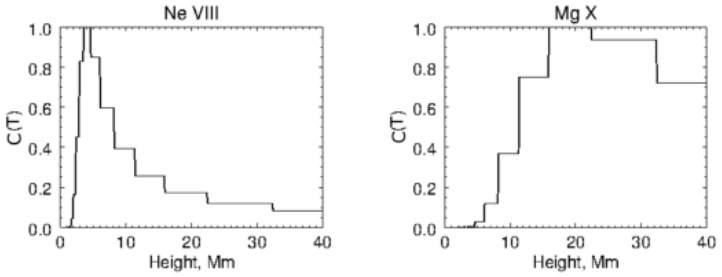

FIGURE 3.4: Normalised contribution function $C(T)$ plotted against height using for SOHO/SUMER filters at time $t = 0$. This is recalculated at each time iteration for the LOS integration to account for temperature variations. The corresponding initial temperature profile is shown in Figure 2.3.

The SDO/AIA response functions were generated using version V6 available in ssw-idl (Boerner et al 2012). Contribution functions $C(T)$ are generated for other instruments using CHIANTI V7 (Dere et al 1997, Landi et al 2013).

3.1.3 LOS integration vs single point analysis

The LOS spectra (Figure 3.2) are different to the frequency spectra in the single point analysis, see Figures 2.10 and 2.11 in Chapter 2. The primary difference in the frequency spectra is the range of frequencies present in the broad peak. The lower limit of this region is the same, indicating that the acoustic cut-off frequency is detectable in both

cases. The upper limit of the broad peak was fixed for the single point analysis, however varies in the LOS spectra.

The LOS integration gives different results compared to the single point analysis. Possible explanations are as follows:

1. The integration of a sinusoidal function depends on the depth of the LOS integration and the periodicity of each individual component of the signal. As such, the power of the individual frequencies is modified non-uniformly by performing the LOS integration. This results in a different power distribution compared to the single point analysis.

2. The spectral lines/filters have a finite width covering a temperature range. This is in contrast to the single point analysis that isolates a single temperature value. The same holds for the mass density, ρ.

3. The distribution of the frequency spectra changes with height in the transition region where the temperature gradients are large. As one moves into the corona, the variation in the shape of the frequency spectra decreases. Any spectral lines/filters including contributions from the transition region will be affected. The single point analysis results discussed in this paper are obtained in the corona. Therefore, the weighted transition region will enhance the differences between the single point analysis and the LOS integration.

3.1.4 Angle of LOS integration

In the 1.5D model the LOS integration is performed parallel to the magnetic field lines (note that the magnetic field lines are uniform and perpendicular to the solar surface). Performing the integration perpendicular to the magnetic field will yield the single point result (since it is invariant in this direction). Integrating at an angle produces the same results as integrating parallel to the magnetic field line, since, even though the path length appears longer, it intercepts the same discrete values in the same order. A sketch of this is in Figure 3.5.

3.1.5 Comparison with observations

The frequency spectra obtained in Figure 3.2 are very similar to observational papers as can be seen in Tian et al. [2014]; an excited range of frequencies is present between approximately 4.5 and 10 mHz [Reznikova et al., 2012, Thomas et al., 1987, Tian et al.,

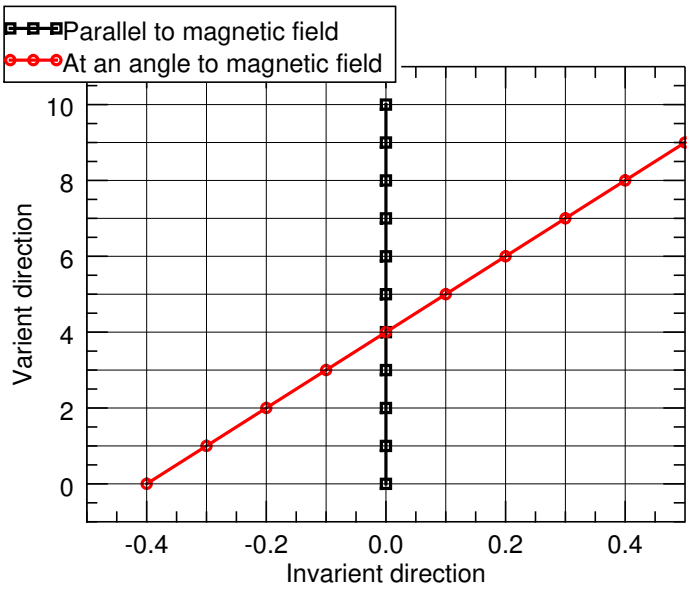

FIGURE 3.5: Sketch of different angles of integration in 1.5D. Both the circles and the squares would yield the same data.

2014]. For wider chromospheres, this is more distinct and the excited range is reasonably narrow. However for smaller chromospheres the LOS spectra are far more noisy and whilst there are a few strong peaks, the power does not decay rapidly, as can be seen in Figure 3.2. The bandwidth of the LOS frequency spectra can be used to estimate the chromospheric cavity size, as was discussed in Section 3.1.1. For example the 4.5 to 10 mHz range observed by Thomas et al. [1987] would indicate a chromospheric cavity size of greater than 2.13 Mm.

3.2 Kink-unstable flux rope

The second line-of-sight study is performed on the 3D numerical MHD simulation of Botha et al. [2011] looking at a kink-unstable coronal flux rope with thermal conduction. The simulation was performed using Lare3D [Arber et al., 2001]. This initial condition is a force-free equilibrium that is unstable to an ideal MHD kink instability, as in Hood et al. [2009], that satisfies the equation

$$\nabla \times \mathbf{B} = \alpha(\mathbf{r})\mathbf{B}$$

Inside the loop the magnetic field is specified as

$$B_\theta = \lambda r(1-r^2)^3, \tag{3.2}$$

$$B_z = \sqrt{1-\frac{\lambda^2}{7}+\frac{\lambda^2}{7}(1-r^2)^7-\lambda^2 r^2(1-r^2)^6}, \tag{3.3}$$

$$\alpha = \frac{2\lambda}{B_z}(1-r^2)^2(1-4r^2). \tag{3.4}$$

Outside the loop, the magnetic field is specified as

$$B_\theta = 0, \tag{3.5}$$

$$B_z = \sqrt{1-\frac{\lambda^2}{7}}, \tag{3.6}$$

$$\alpha = 0. \tag{3.7}$$

where $\lambda = 1.8$

The model also includes Braginskii thermal conduction. This introduces a heat flux term $\nabla \cdot \mathbf{q}$ and the energy equation becomes:

$$\rho\frac{D\epsilon}{Dt} - \nabla\cdot\mathbf{q} + P\nabla\cdot\mathbf{v} - \eta j^2 = 0 \tag{3.8}$$

with a heat flux vector $\mathbf{q}$ defined as

$$\mathbf{q} = (\kappa\hat{\mathbf{B}}\cdot\nabla T)\hat{\mathbf{B}} \tag{3.9}$$

where $\hat{\mathbf{B}} = \mathbf{B}/B$ and $\kappa = 10^{-11}T^{5/2}$. This is the Braginskii thermal conduction parallel to magnetic field lines. The effect of including this is a reduced local temperature since thermal energy is conducted along the magnetic field lines. The radiative cooling time is of order hours for the coronal values used in the simulation, whereas the cooling time due to thermal conduction is of order minutes [Botha et al., 2011].

Anomalous resistivity in the numerical code is triggered when the current exceeds a critical value. The initialisation parameters are taken from an observation by Srivastava et al. [2010], with temperature and mass density constant at $T = 0.125$ MK and $\rho = 1.67 \times 10^{-12}$ kg m^{-3}. The loop structure is that of a straight cylinder, placed in a Cartesian numerical grid with the foot points located at $z = 0$ and $z = 80$Mm. Surrounding the loop is a straight constant magnetic field orientated along the loop axis. The maximum number of twists is 6 full turns. The boundaries in the x, y-plane (perpendicular to the loop) at ± 8 Mm are reflective. On the z boundaries at $0, 80$ Mm, the velocity is fixed at zero. Full details of the simulation can be found in Botha et al. [2011].

3.2.1 Evolution of the instability

During the initial linear phase, the initial magnetic field twist grows, resulting in the formation of current sheets. The loop then enters the non-linear phase where the current sheets reconnect, releasing energy, and the magnetic field becomes less twisted. The simulation is dominated by magnetic pressure (low plasma-β), plasma thermal pressure plays a minimal role. The initial temperature is uniform. There is an increase in temperature at the reconnection sites when the kink instability triggers reconnection. The temperature spreads through the loop and is enhanced when secondary reconnection events are triggered. The increased temperature results in an increased pressure gradient which acts to drive flows parallel to the magnetic field, which can then trigger subsequent reconnection events.

A plot of the maximum temperature and mass density along the cross section of the loop is shown in Figure 3.6. The temperature maximum in the simulation is approximately 12 MK that occurs at time $t = 348$ seconds, shortly after the loop enters the non-linear kink phase. Following this, the temperature lowers and has a maximum value of approximately 4 MK at time t=522 seconds. Late in the simulation, there is an increase in density at the footpoints of the loop due to plasma flows away from the centre of the domain. This resulted in footpoint brightening at late times when the intensities were calculated using SDO/AIA and TRACE response function [Botha et al., 2012].

3.2.2 Hinode/EIS

Three Hinode/EIS lines are considered: O V (248.46 Å), Fe X (184.54 Å), and Fe XV (284.16 Å). Wavelengths and temperature peaks for these spectral lines are shown in Table 3.1. The contribution functions for these lines are synthesised using Chianti v7 [Dere et al., 1997, Landi et al., 2013], and are plotted in Figure 3.7. Theses lines are

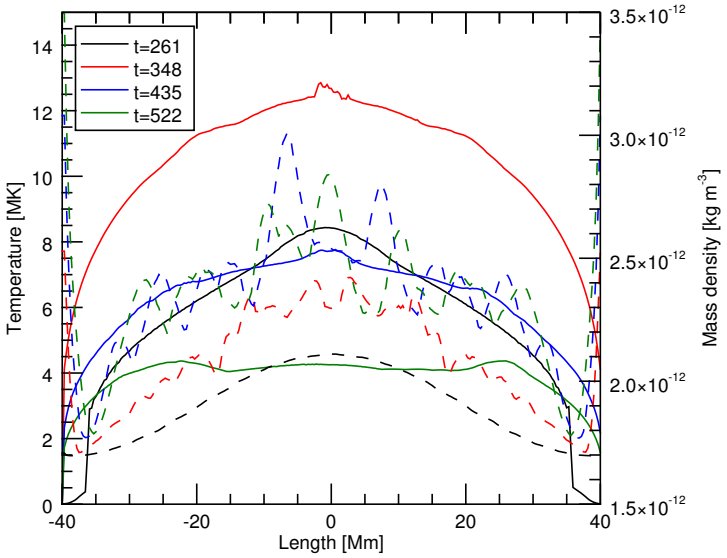

FIGURE 3.6: Maximum temperature (solid) and density (dashed) profiles along the loop length z. Each value is the maximum value sampled across the xy plane, i.e. the cross section of the loop.

Spectral line	Wavelength (Å)	Peak temperature log(T)	Counts
O V	248.46	5.4	300
Fe X	184.54	6.05	1000
Fe XV	284.16	6.35	4720

TABLE 3.1: Hinode/EIS spectral lines. The photon counts are calculated based on the maximum contribution of the line using $n_e = 1.0 \times 10^9$ cm^{-3} and a 50 second exposure time.

chosen to consider the intensity across a range of temperatures. The Fe XII (195.12 Å) spectral line was also tested however the results were very similar to the results from the Fe X line so have been omitted. The background temperature of the simulation is 0.125 MK. The peak temperature in the simulation is approximately 12 MK however this rapidly cools down to a peak temperature of approximately 4 MK towards the end of the simulation.

The intensity is calculated as the integral along a line-of-sight of density squared times the contribution function, i.e.

$$I = \int n_e^2 C(T) dl \tag{3.10}$$

where n_e is electron number density, T is temperature, $C(T)$ is the contribution function of the line, and l is the distance along the line-of-sight.

Integration is considered along the three Cartesian coordinates x, y, z. A cartoon of the three Cartesian angles is shown in Figure 3.8. Note that in the cartoon the x and y angles show the same image. This is because the cartoon is rotationally symmetric. The

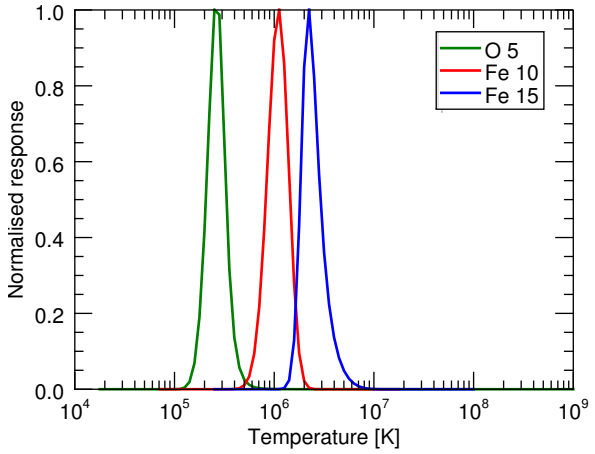

FIGURE 3.7: Contribution functions for the different spectral lines considered in this paper.

simulation is rotationally asymmetric so the x and y views have different intensity maps. This layout of integration angles is used consistently throughout this section.

The z view of the loop is through the footpoints. This is a non-physical view however it is useful in understanding the physics of the system and the distribution of heating throughout the loop.

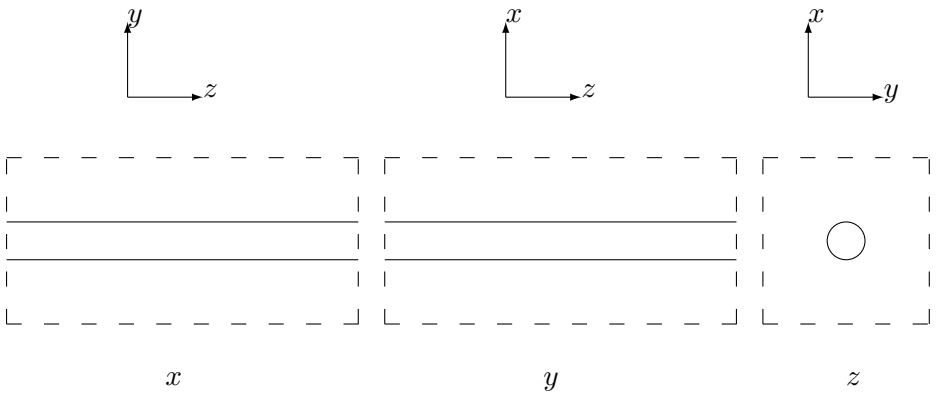

FIGURE 3.8: Cartoon illustrating the loop observed along Cartesian coordinates x, y, z. Note that the simulation is asymmetric so the intensity maps will show different images when integrated over x and y.

3.2.3 Simulation resolution intensities

First the simulation resolution intensities are calculated. These are at numerical resolution ($\delta x = \delta y = 0.125$ Mm, $\delta z = 0.3125$ Mm), with no temporal integration or spatial degradation. A time series of the intensities observed integrating along each of the Cartesian coordinates x, y, z is shown for the O V, Fe X and Fe XV spectral lines in Figures 3.9,

3.10 and 3.11 respectively. The figures demonstrate the behaviour of the loop though time in the different spectral lines. In all figures a dark colour indicates high intensity. Contour levels are fixed for each column. Time $t = 261$ seconds corresponds to the end of the linear growth phase of the kink instability. At this time the x and y lines clearly show a highly twisted loop in all three spectral lines.

Between $t = 261$ and 290 seconds the kink instability breaks down generating a large amount of small scale structure in all three lines at time $t = 290$ seconds. During this time the interior magnetic field is reconnecting and the loop begins to expand radially. The average intensity decreases during this time frame for all three spectral lines.

After this, between $t = 348$ and $t = 406$ seconds the average intensity starts to rise in all three lines. This corresponds to loop starting to reconnect with the exterior field. The Fe XV line increases most indicating strong heating due to the reconnection with the exterior field. The O V line also demonstrates an increase in intensity. From Figure 3.9, it is clear that this is occurring on the edge of the loop and is due to the heat spreading out through the domain. This is also present in the Fe X lines (Figure 3.10) although to a lesser degree.

At late times, $t \geq 450$ seconds, the Fe X line shows strong footpoint brightening that is not present in the O V spectral line. The Fe XV line demonstrates high intensity throughout the loop at late times. From Figure 3.6, this is the temperature is redistributed inside the loop such that the Fe XV spectral line is activated.

Integrating from the z direction yields a top-down view of the loop, essentially showing the growth of the loop and interior temperature. It also shows that the majority of the activity is occurring on the outer surface of the loop. After time $t = 348$ seconds the Fe XV line starts to show some interior structure in the top view. Interior structure is present in the x and y intensity maps after time $t = 464$ seconds in the Fe X and Fe XV lines but not in the O V. This is because the temperature inside the loop it too hot to activate the O V line. Instead, the O V line shows the loop conducting heat radially outwards.

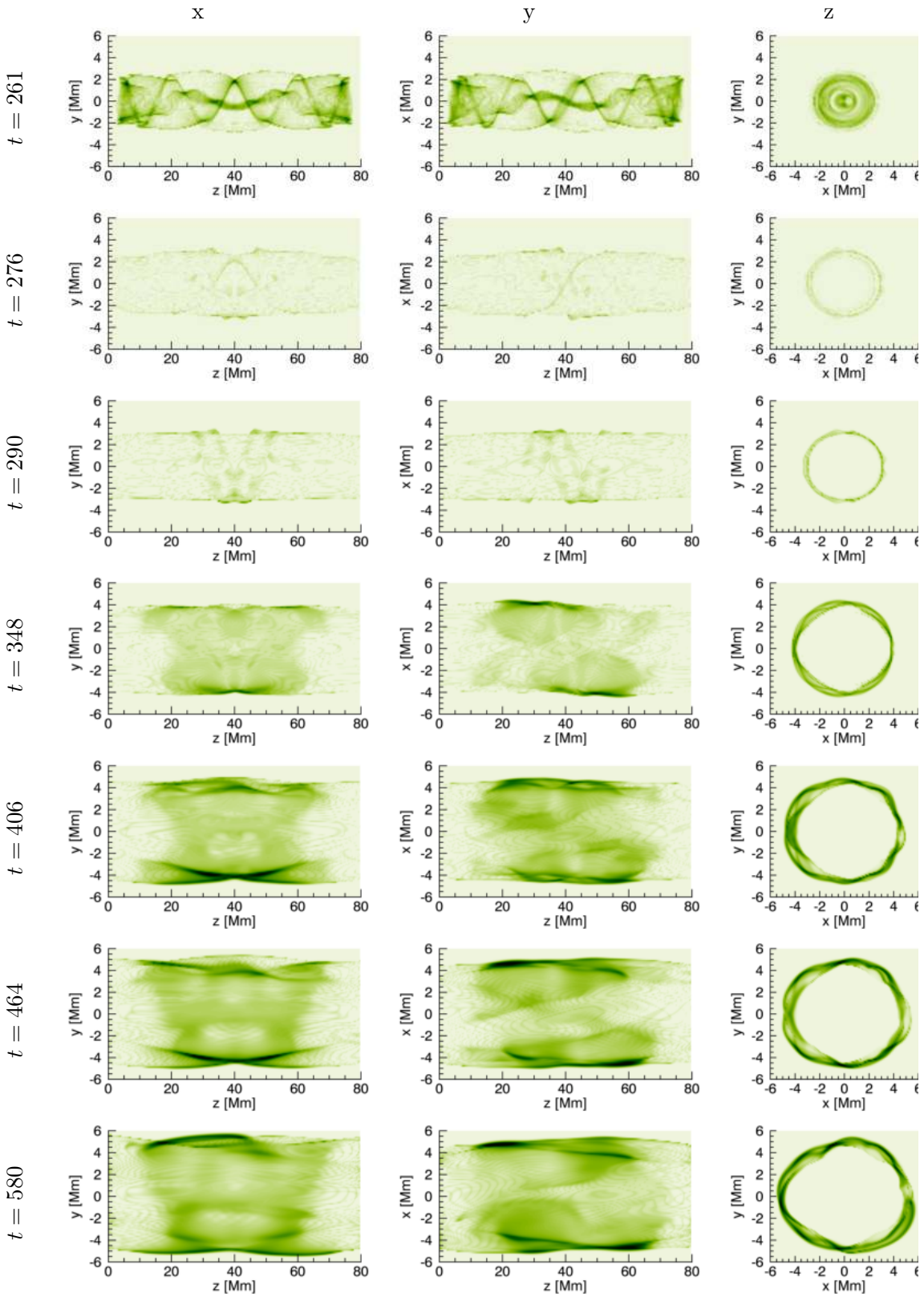

FIGURE 3.9: Simulation resolution intensities using the O V spectral line of Hinode/EIS. Dark indicates high intensity. Contour levels are consistent in each column. Time is in seconds.

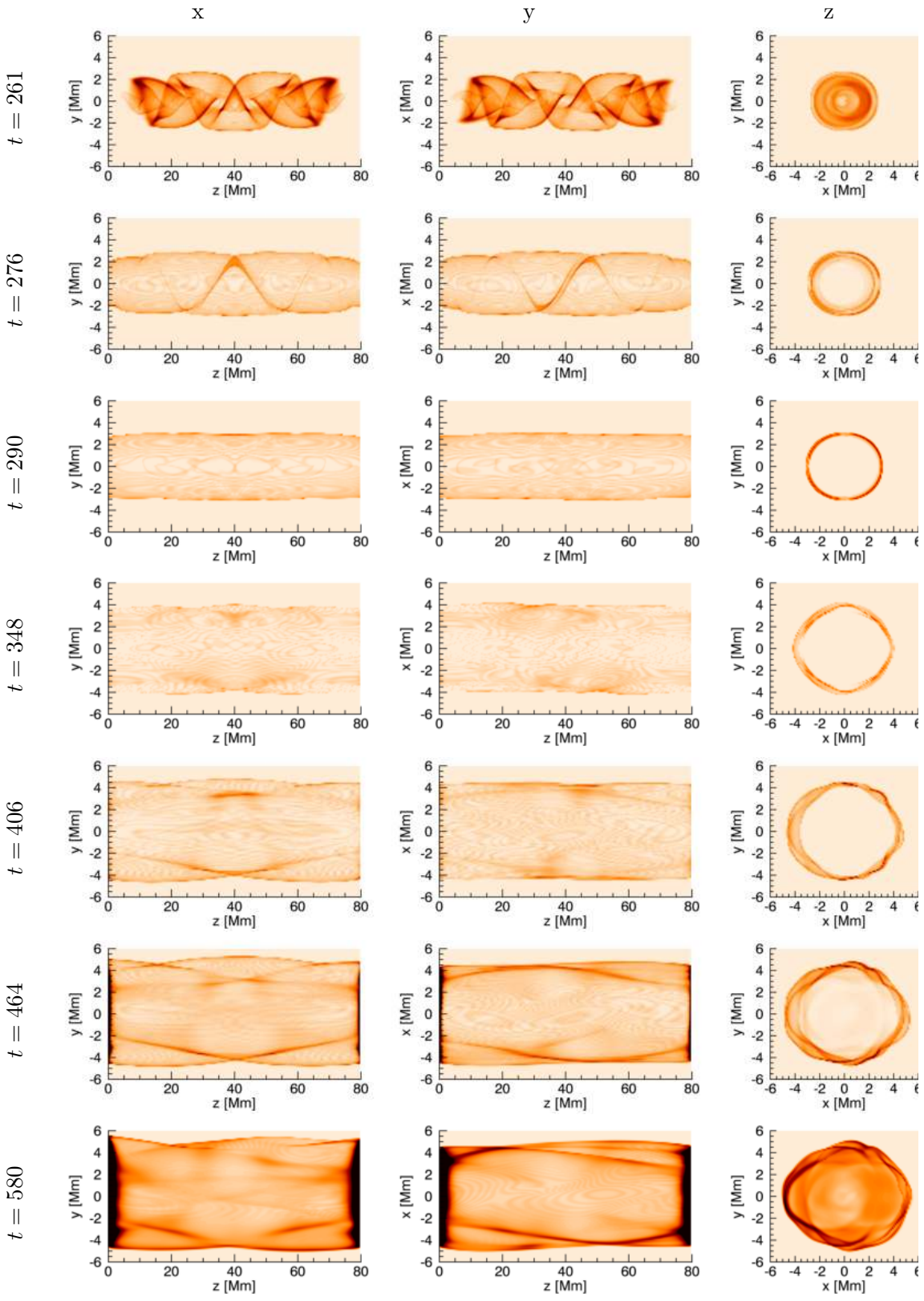

FIGURE 3.10: Simulation resolution intensities using the Fe X spectral line of Hinode/EIS. Dark indicates high intensity. Contour levels are consistent in each column. Time is in seconds.

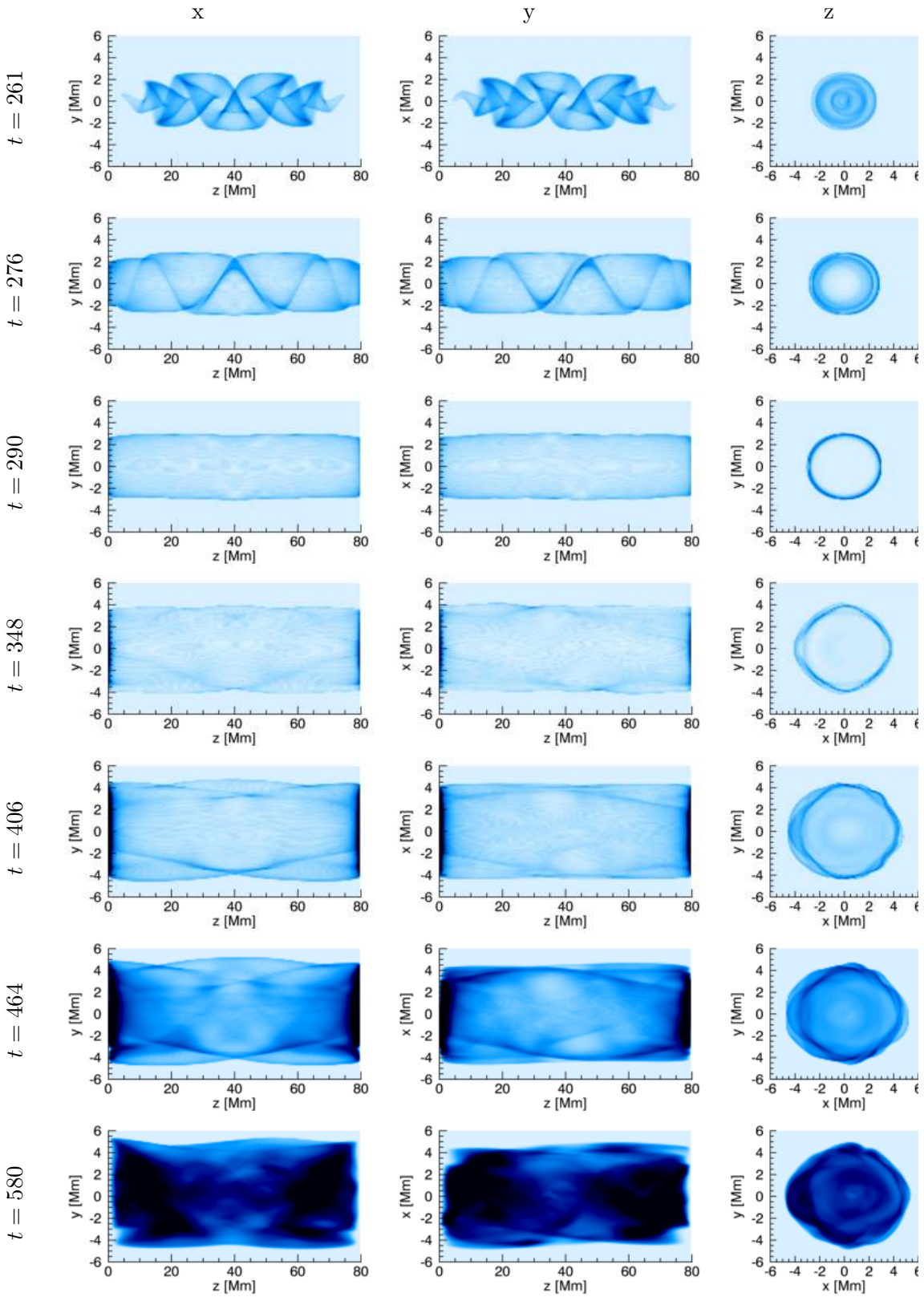

FIGURE 3.11: Simulation resolution intensities using the Fe XV spectral line of Hinode/EIS. Dark indicates high intensity. Contour levels are consistent in each column. Time is in seconds.

3.2.3.1 Spatially degraded intensities

Next the intensities are spatially degraded to the Hinode/EIS pixel size of approximately 1 arcsecond^2. Figure 3.12 and 3.13 show the simulation resolution and the spatially degraded intensity maps at time $t = 261$ and $t = 348$ seconds for the Fe x spectral line. The spatially degraded intensities lose some of the small scale features but still capture the larger structures present in the simulation resolution intensity maps. This applies similarly to the other spectral lines.

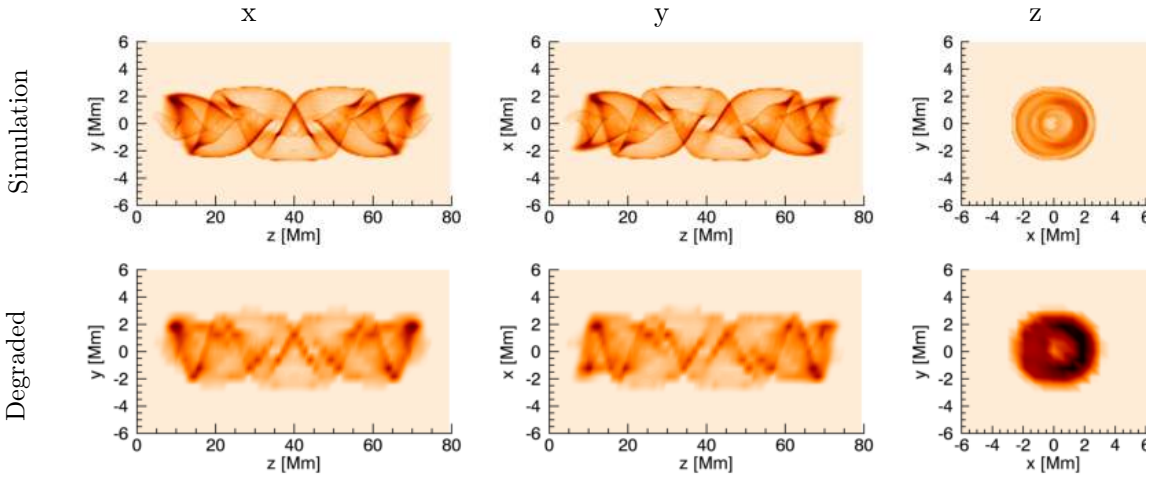

FIGURE 3.12: Simulation intensities vs. spatially degraded intensities using Fe x spectral line of Hinode/EIS at time t=261 seconds. The simulation intensities are at the numerical resolution. Degraded intensities have a spatial resolution of approximately 1 arcsec.

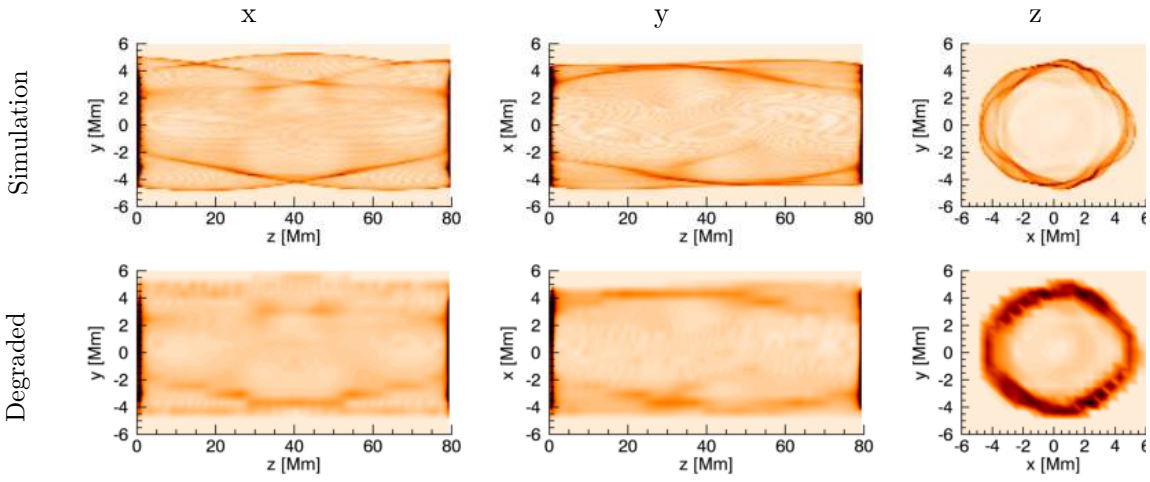

FIGURE 3.13: Simulation intensities vs. degraded intensities using Fe x spectral line of Hinode/EIS at time t=464 seconds. Spatial degredation is the same as in Figure 3.12

3.2.3.2 Intensity raster

Finally one can reconstruct the raster image that would be observed by Hinode/EIS. This involves scanning a 1 arcsecond slit for approximately 50 seconds then advancing the slit. This results in an image that is advancing in time as you move in space. There are two main types of moving rasters: dense and sparse. For the dense raster, the slit is advanced to the next position at the end of exposure. The sparse raster has a jump of 3 arcseconds between exposures. This means the rasters cover a greater proportion of the loop however leave gaps. We consider the slit moving parallel to the loop length, and moving perpendicular to the loop length. A cartoon of this is shown in Figure 3.14, with the arrow denoting the movement of the slit.

Parallel Performing the integration with the slit moving parallel to the loop length (Figure 3.14a), the raster cannot capture the full length of the loop due to the length of the simulation. Multiple rasters using both the sparse and dense modes using Fe X are shown in Figure 3.15. For the dense raster, six different rasters were synthesised starting at different points along the loop length. For the sparse raster, three were created.

The dense rasters all look fairly similar. The increase in intensity towards the radial edge of the loop is present. The loop growth is also observable. However, these dense raster only observe a small fraction of the loop length and therefore are unable to capture larger structures. A small amount of interior structure is present towards the end of the rasters.

For the sparse raster, the same increase in intensity towards the edge of the loop and loop growth are observable. Here, since more of the loop is captured, some larger interior structure is present.

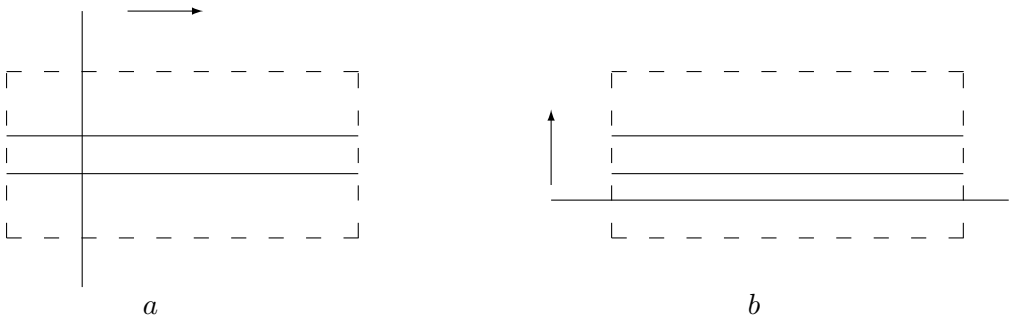

FIGURE 3.14: Cartoon illustrating the movement of the slit for the two types of raster: moving parallel to the loop length a, and moving perpendicular to the loop length b.

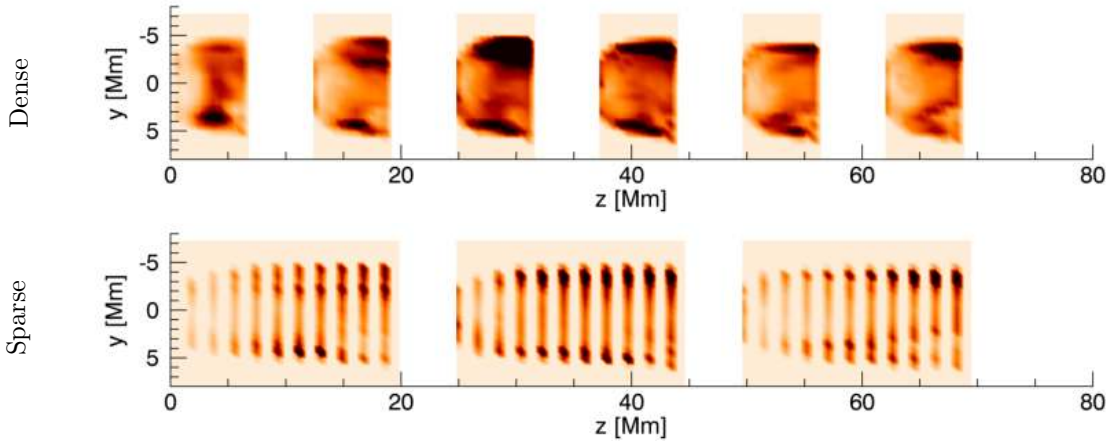

FIGURE 3.15: Dense (top) and sparse (bottom) intensity rasters integrated in x-direction for the Fe X spectral line. Slit moves left to right, as is Figure 3.14a. Several rasters are generated starting at different points along the loop. Each raster has the same time frame. The exposure time of the slit is 50 seconds.

Perpendicular Moving the slit perpendicular to the loop, shown in Figure 3.16, most of the loop is captured. These are shown in Figure 3.16 for the three spectral lines considered. By comparing the intensity, one can observe the loop heating and cooling across the different spectral lines. The Fe XV is the hottest spectral line and demonstrates an increase in intensity in the interior of the loop, followed by a decrease in intensity. At the same time, the O V and Fe X spectral lines demonstrate a steady increase in intensity in the interior of the loop. This signifies the loop decreasing in temperature and activating the cooler spectral lines. However, it is difficult to comment on the growth of the loop from these perpendicular intensity rasters. Footpoint brightening is present in the Fe X and XV spectral lines. This is due to the density accumulating at the numerical boundaries, as can be seen in Figure 3.6.

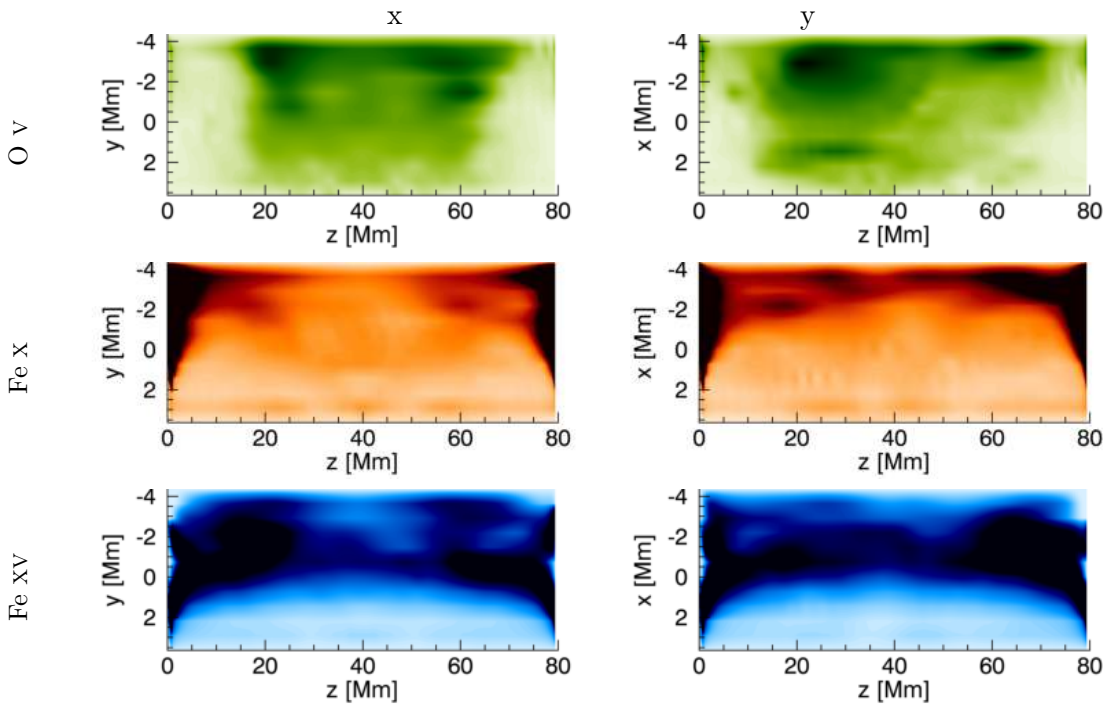

FIGURE 3.16: Intensity rasters integrated in x-direction with slit moving perpendicular to loop length, as in Figure 3.14b. Exposure time is approximately 50 seconds. The full loop is captured in these rasters.

3.2.4 Sit-and-stare

One can also consider the slit remaining stationary and observing the same section of the loop at different times. For this, a point along the loop length is chosen and is repeatedly scanned for the exposure time of 50 seconds. The resultant time-distance plot for the Fe X line are shown in Figure 3.17. Three points along the loop length were chosen: left (20Mm), centre (40Mm) and right (60Mm). Two key features are present when the loop is observed in this way.

The first feature is the distribution of intensities. After a few exposures, the intensity forms a peak at the edges of the loop in all spectral lines at all locations throughout the loop, Figure 3.17. This corresponds to the heating seen at the edge of the loop after time $t = 464$ seconds in Figure 3.10 for the simulation resolution intensity maps.

The second feature is the growth of the loop. The loop width can be measured at each exposure for the three spectral lines considered here. Figure 3.18 shows the loop width at different times. Multiple slit locations along the loop are plotted, and whilst there is some variation in loop width, the variation is fairly small and not related to the spatial location of the slit within the loop. We see a staggered rise in the loop width across the spectral lines. The loop width in the cooler O V line increases first, followed by the Fe X and finally the hotter Fe XV line. This is due to a combination of parallel thermal

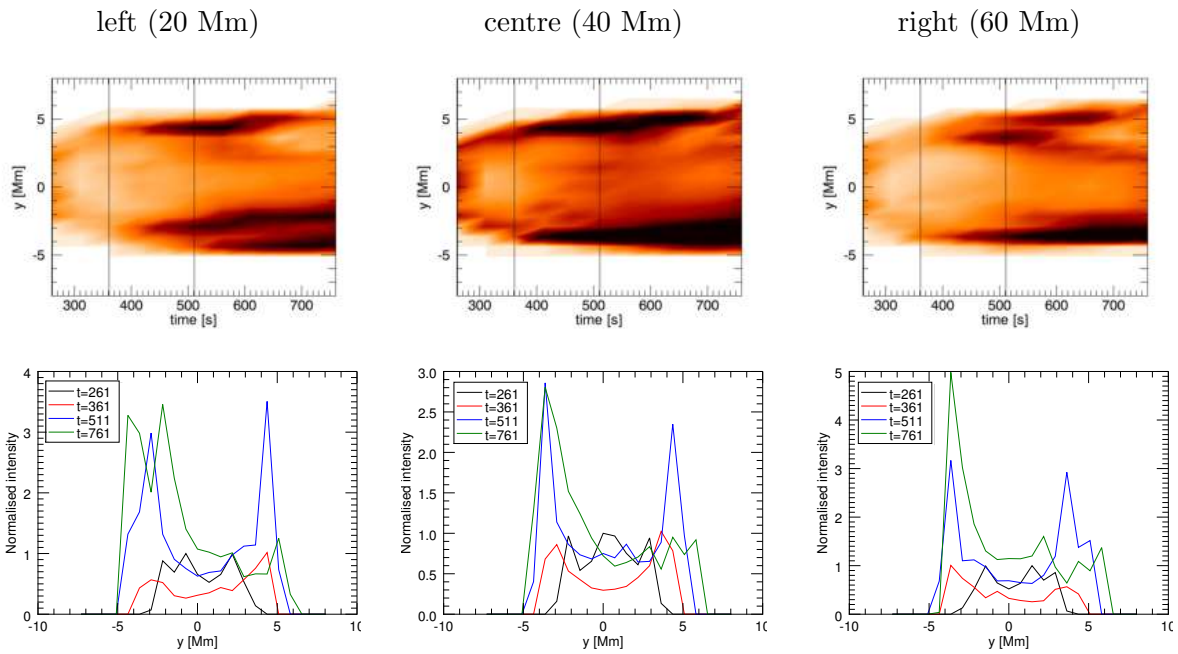

FIGURE 3.17: Time-distance plots using the Fe X spectral line integrated in the x-direction with the slit stationary at $z = 20$ Mm (left), 40 Mm (centre) and 60 Mm (right) along the loop axis . The bottom row of figures is snapshots of the intensity at different times. These times are 261,361, 511 and 761 seconds, as indicated by the black lines in the time-distance plots.

conduction and reconnection acting to effectively spread heat radially outwards [Botha et al., 2011]. This results in the cooler lines being activated further away from the loop centre so the loop appears wider in the cooler spectral lines. The red line in Figure 3.18 respresents the loop width measured using the simulation resolution results. The loop width from the raster is an overestimate of this. The raster works by summing up the intensities over the exposure time. This means that the largest value of the loop width during this time frame determines the width of the loop in the raster. This is further modified by the spatial degradation that sums up the intensities in a block of 1 arcsecond^2. These effects contribute most when the loop is growing rapidly, i.e. when the kink instability enters the non-linear phase. After time $t \approx 400$ seconds, the loop growth occurs at a slower rate and the loop width from the raster is closer to the simulation resolution.

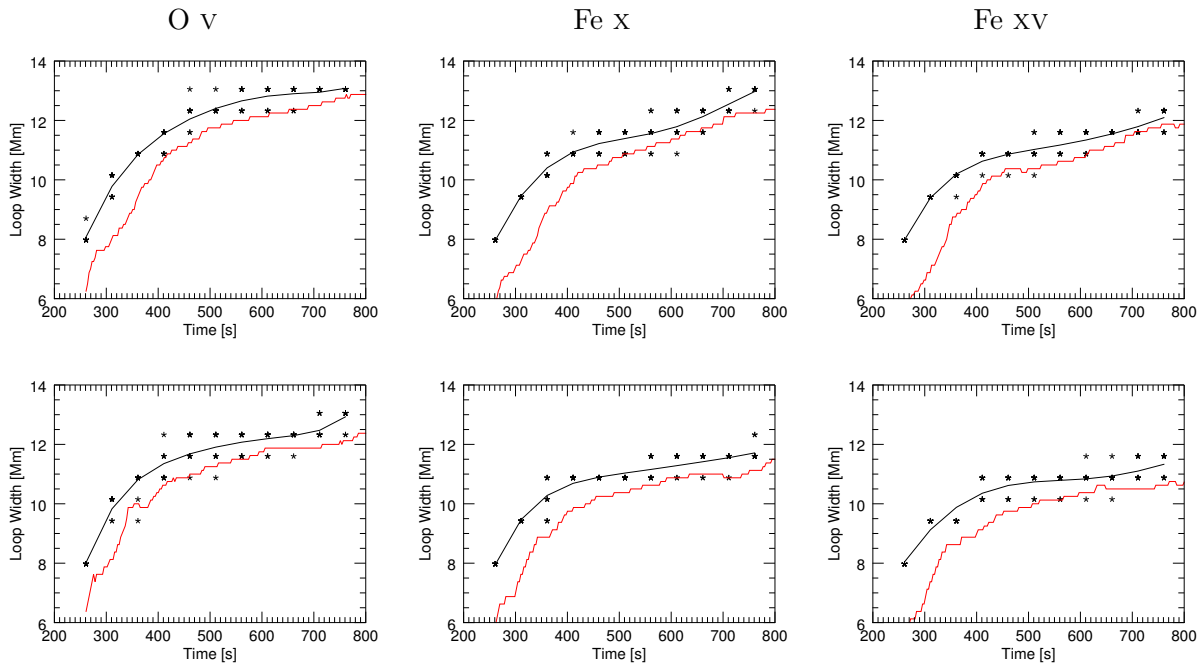

FIGURE 3.18: Loop width vs time for the different spectral lines using the sit-and-stare mode of Hinode/EIS integrated in the x-direction (top) and y-direction (bottom). The width was measured at 10 different locations and plotted as crosses (note that many of the crosses have the same width values). A best-fit polynomial (black line) overlays the measures points. The red line is the loop width obtained directly from the intensities at the numerical resolution.

3.2.5 Doppler velocities

Doppler velocities D can be calculated according to Equation (1.70)

Contour plots of the Doppler velocities at simulation resolution are shown in Figures 3.19, 3.20 and 3.21 for the O V, Fe X and Fe XV spectral lines respectively. The contour colour is between $\pm$ 100 km s^{-1} in all plots. Histograms of the Doppler velocities in the range $\pm$30 km s^{-1} for the contour plots are shown in Figure 3.22. Magnetic fieldlines are aligned in the z-direction so velocity is guided in this direction. This results in larger velocities in the z-direction compared to the x-direction and y-direction.

The Doppler maps show that there is a burst in velocity as the kink instability breaks at time $t = 261$ seconds. The x and y views of the loop show very little Doppler shift between $t = 276$ and $t = 290$ seconds. The z view of the loop for the Fe X spectral line shows a multitude of small bright-points in the time frame $276 \leq t \leq 348$ seconds. These are indicative of small scale reconnection events occurring inside the loop, i.e. interior magnetic field reconnecting. These localised bright-points are only present in large quantities in the Fe X spectral line, suggesting a temperature of approximately 1

MK. The hotter Fe XV and cooler O V lines show interior flows in the z-direction but very few small bright-points. This means they occur is a very narrow temperature range.

At time $t = 348$ seconds there is a sudden increase in Doppler velocity in all three lines, from all integration angles. This is when the loop starts to reconnect with the exterior magnetic field. The majority of activity occurs on the outside of the loop as shown in the z view. The histogram of the Doppler velocities at this time (Figure 3.22) shows an increase in the counts for faster velocities and also shows a bimodal low velocity peak forming in all the lines around the zero point, in the x and y views of the loop. These bimodal peaks disappear by time $t = 580$ seconds.

The histograms of the Doppler velocity (Figure 3.22) show the distribution in the range ± 30 km s^{-1}. Between time 261 and 290 seconds the loop becomes less active, as was seen in the Doppler and intensity maps. Following this, at time 348 seconds, the loop begins to reconnect with the exterior field and becomes more active, resulting in an increase in Doppler velocities in the range ± 30 km s^{-1}. At this time a bimodal peak appears in the histogram at around ± 3 km s^{-1}. As time advances this peak eventually disappears.

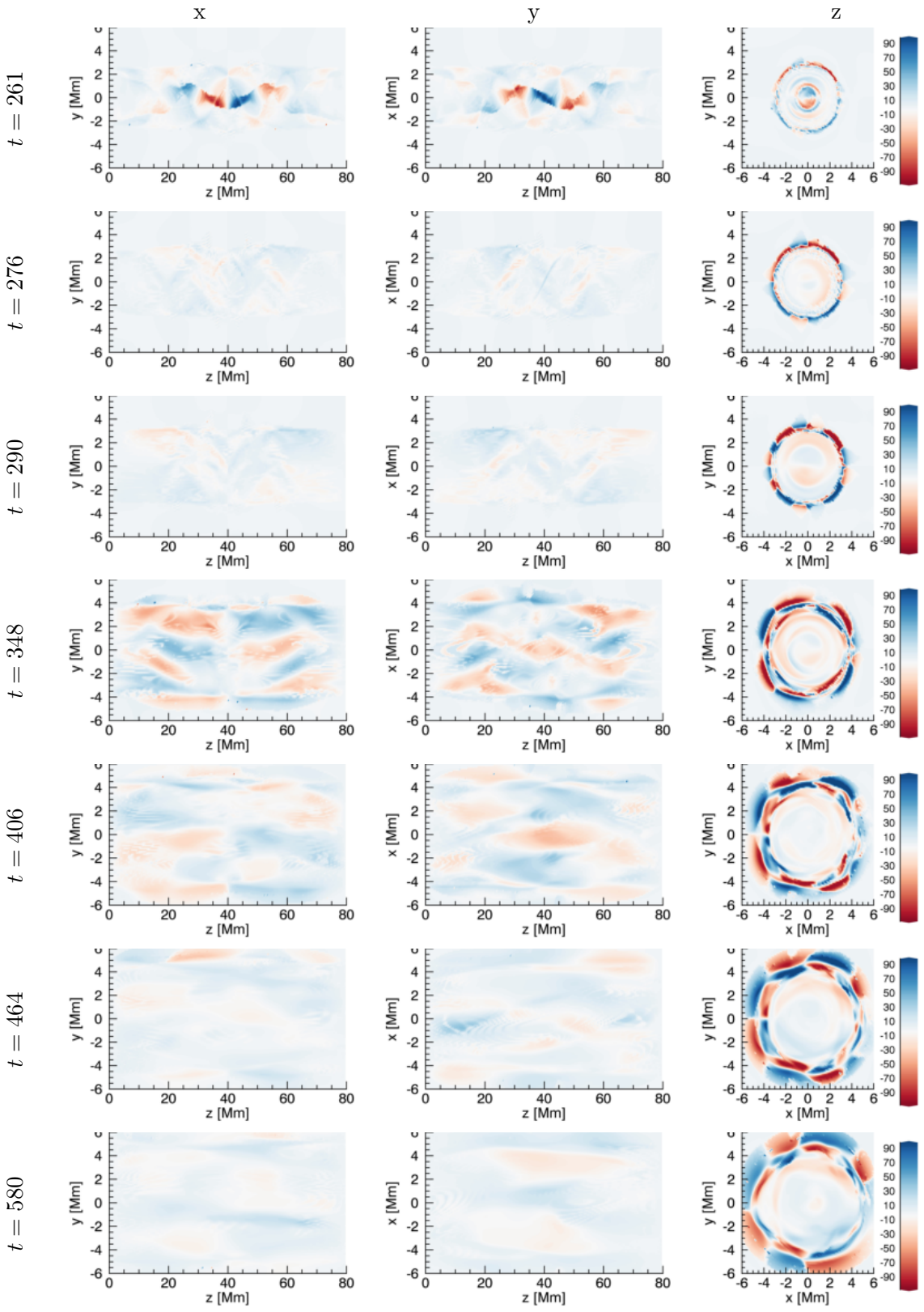

FIGURE 3.19: Simulation resolution Doppler velocities using the O V spectral line of Hinode/EIS. Colour scale is between ±100 km s^{-1}. Time is in seconds.

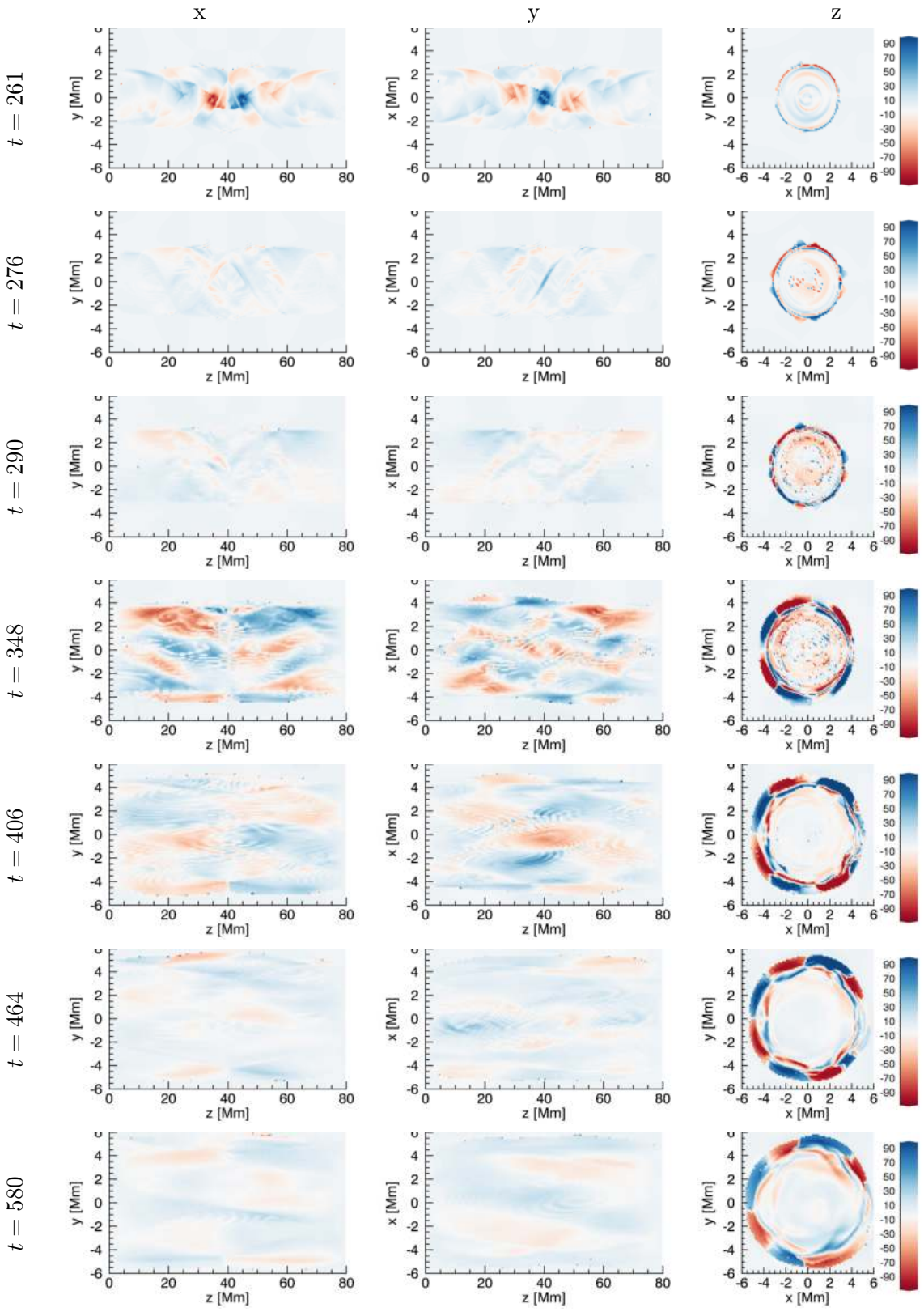

FIGURE 3.20: Simulation resolution Doppler velocities using the Fe X spectral line of Hinode/EIS. Colour scale is between ±100 km s^{-1}. Time is in seconds.

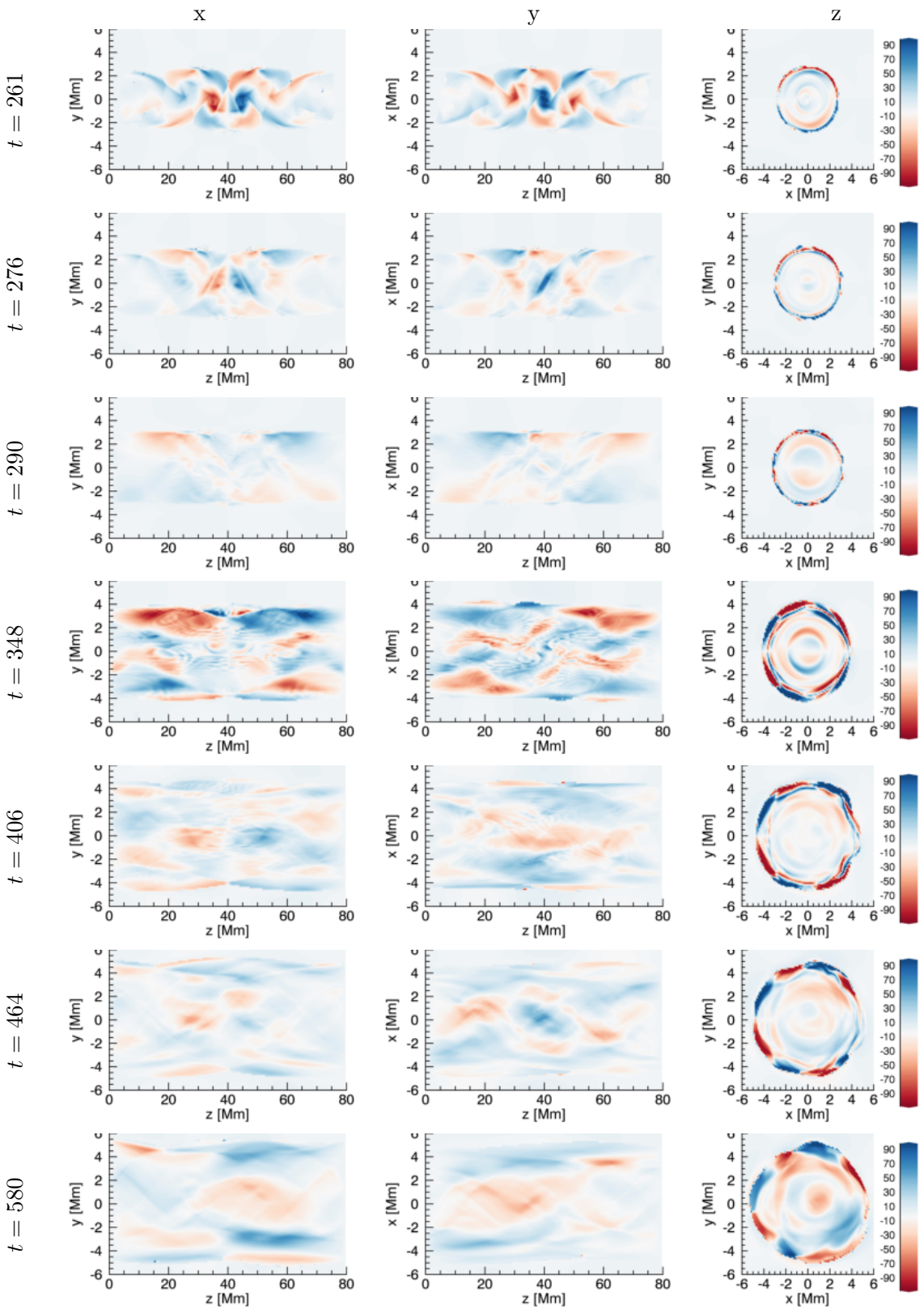

FIGURE 3.21: Simulation resolution Doppler velocities using the Fe XV spectral line of Hinode/EIS. Colour scale is between ±100 km s^{-1}. Time is in seconds.

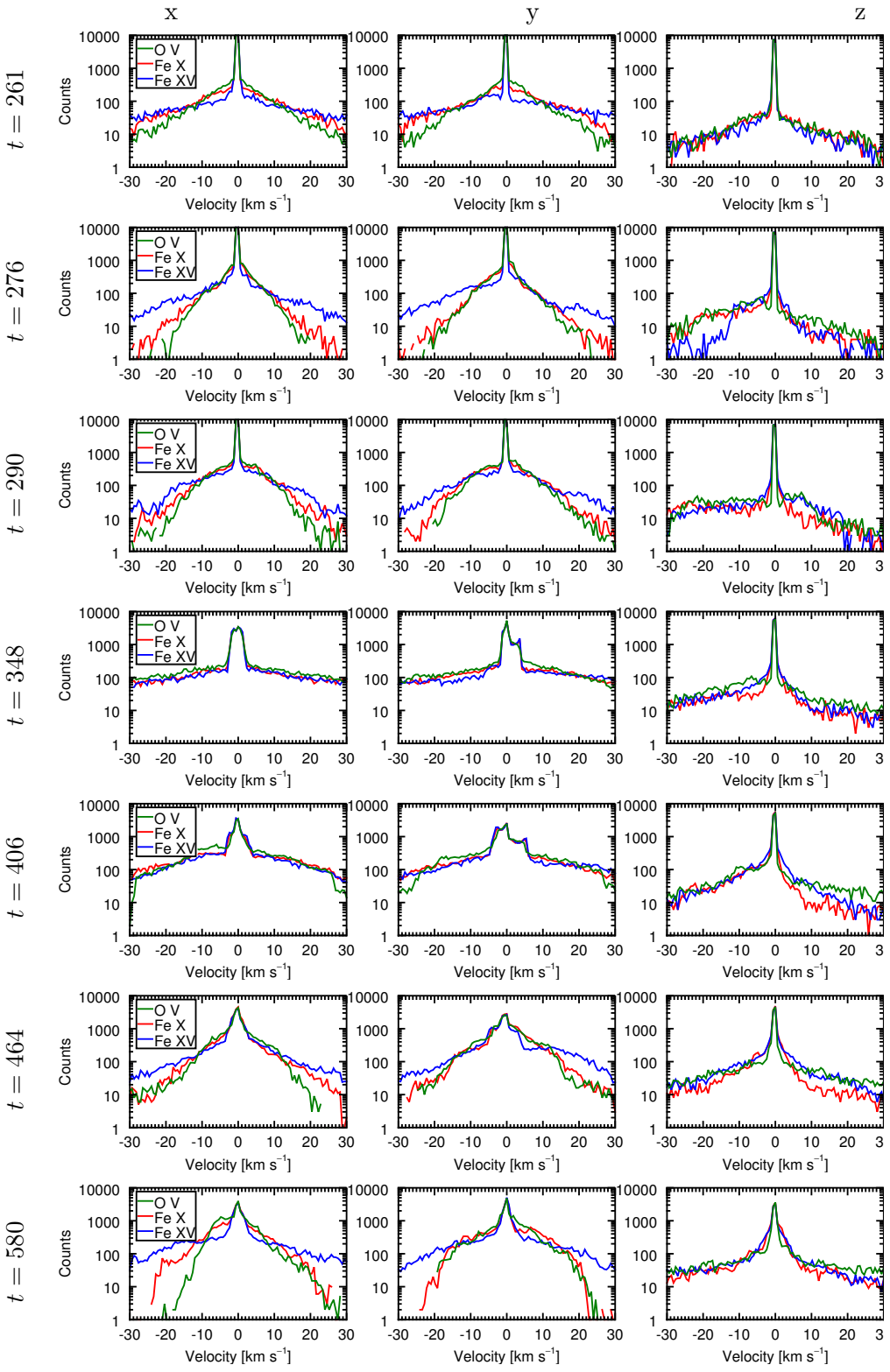

FIGURE 3.22: Histograms of simulation resolution Doppler velocities using the O V, Fe X and Fe XV Hinode/EIS spectral lines. x-axis shows the Doppler velocity between ± 30 km s^{-1} and the y-axis shows the counts. Time is in seconds.

3.2.6 Doppler shift raster

Rasters of the Doppler velocities can be calculated, as before, with a pixel size of approximately 1 arcsecond^2 and an exposure time of 50 seconds. With the slit moving parallel to the loop length (Figure 3.14a) only a small section of the loop is observed. For this reason several rasters have been created, using both the dense and sparse modes, starting at different points along the loop length. These are shown for the Fe X line in Figure 3.23. The contour shows velocity in the range ± 50 km s^{-1}. The dense raster shows that the Doppler shifts are largest towards the centre of the loop, and reduce towards the boundaries.

The dense raster located near the centre of the loop shows oppositely directed Doppler velocities. This type of signal may be observationally interpreted as a rotation of the loop however this is not the case. Velocity in the simulation is guided along the magnetic field lines. In the simulation the magnetic field is twisted and thus the velocity is twisted. The velocity component v_x in this twisted region is approximately ± 55 km s^{-1}, see Figure 3.24. This velocity magnitude pairs up well with the magnitude of Doppler velocity observed using the dense raster near the centre of the loop. Therefore these oppositely directed Doppler velocities do not indicate a rotation of the loop itself, rather they show velocity following a twisted magnetic field.

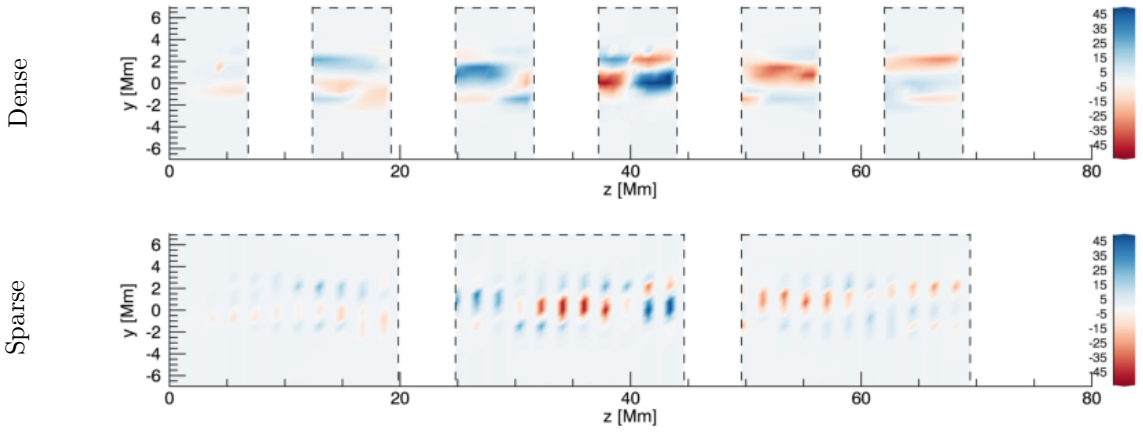

FIGURE 3.23: Dense (top) and sparse (bottom) Doppler rasters with the slit advancing parallel to the loop length (Figure 3.14a), integrated in x-direction for the Fe X spectral line. The colour bar is between ± 50 km s^{-1}.

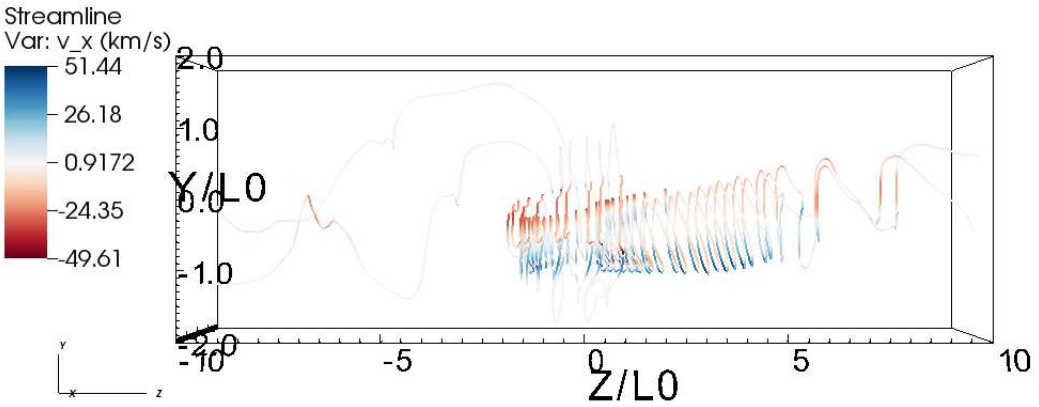

FIGURE 3.24: Velocity streamlines from the simulation, contoured by the v_x component of velocity. This is analogous to the Doppler velocity in Figure 3.23. Streamlines were chosen to highlight the velocity propagating upwards along a twisted magnetic field.

3.2.7 Sit-and-stare Doppler shifts

A stationary slit is also investigated. Three points along the loop length are considered: left (z =20 Mm), centre (z =40 Mm) and right (z =60 Mm). The time-distance contours, histograms of the Doppler velocities at specific times, and histograms of the time-distance contour are all shown in Figure 3.25.

It is difficult to say much about the nature of the loop from the sit-and-stare Doppler velocities. Histograms of the Doppler velocities at different times show that as time advances, the velocities become smaller. There is also a reduction in the peak at $v = 0$ as time advances. This is because the peak at $v = 0$ is essentially the number of counts outside the loop. As the loop expands, it fills more of the domain reducing this peak at $v = 0$.

The histograms of the time-distance plot show that the loop is slightly more blue shifted when observed on the $z > 40$ side of the loop, and slightly more red shifted when observed on the $z < 40$.

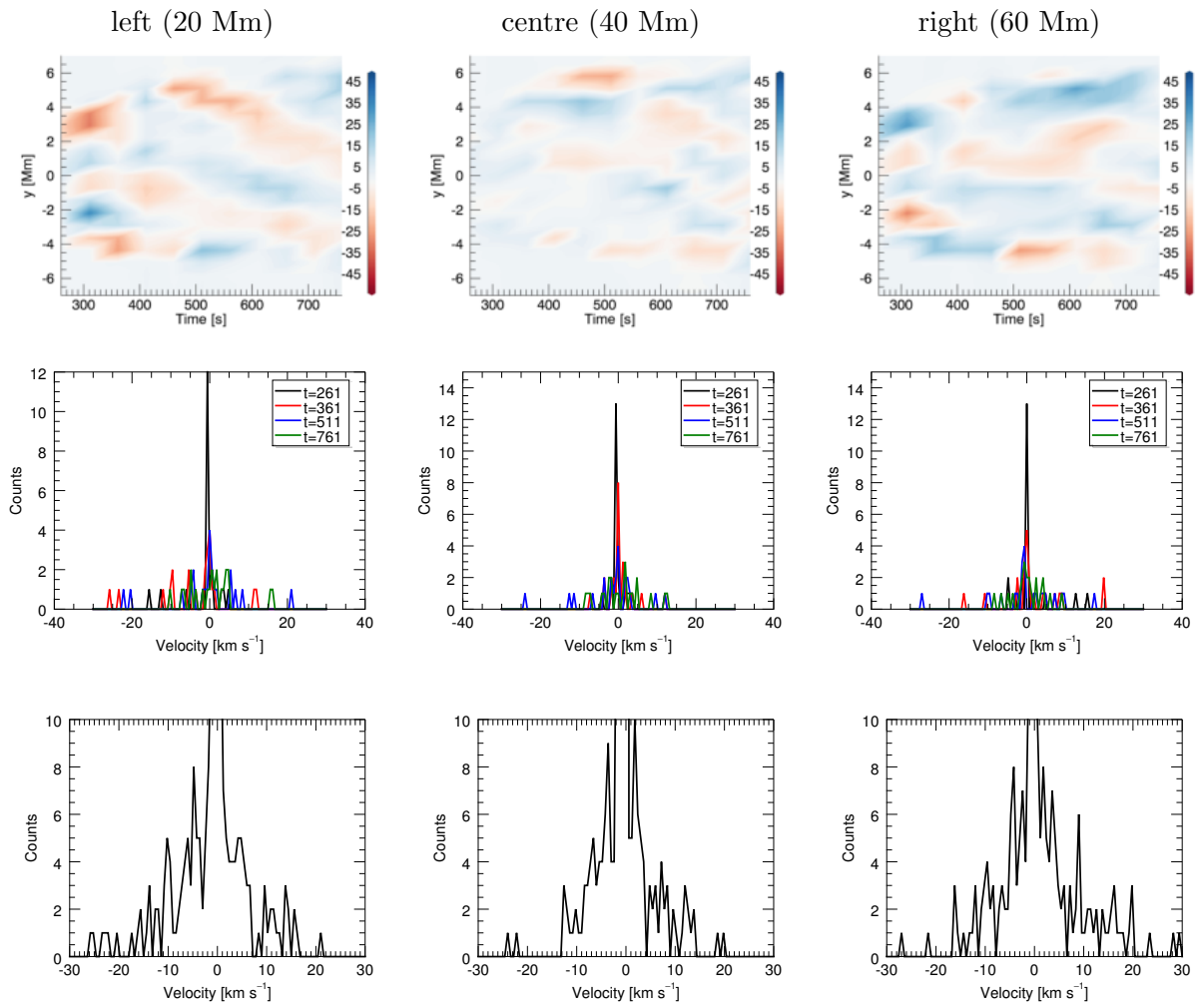

FIGURE 3.25: Doppler velocities using a sit-and-stare mode and the Fe X spectral line. Three points along the loop are tested: left (20 Mm), centre (40 Mm) and right (60 Mm). The first row is a time distance plot of the Doppler velocities. The contour levels are between ± 50 km s^{-1}. The second row is histograms of the Doppler shifts at a few different times. The third row is a histogram of the entire time-distance contour.

3.2.8 Viewing angle

Observing the loop from a different angle yields a different intensity map. Figure 3.26 shows a sketch of the different angles considered. The simulation resolution intensities using these angles at two different times are shown in Figure 3.27 for the Fe X spectral line.

The intensity maps show different viewing angles highlight different structure in the loop. In particular, the different views show the brightening towards the loop edge in a different way. However, when the rasters were performed, these differences became negligible and looked very similar to the rasters in Figure 3.15.

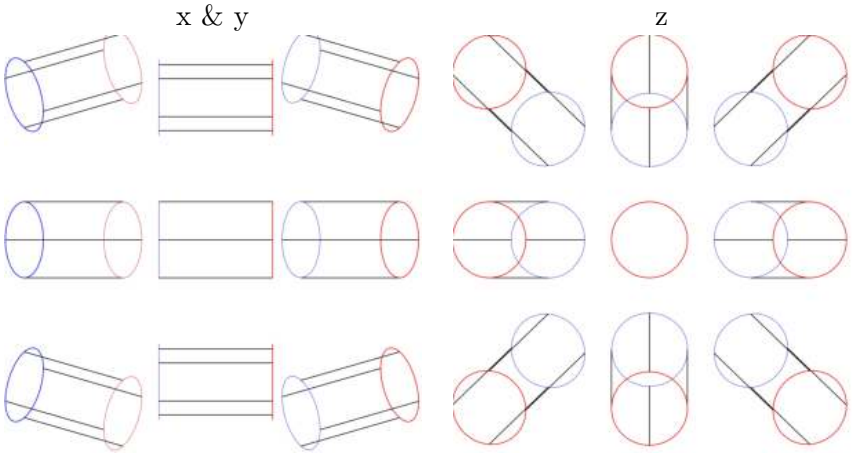

FIGURE 3.26: Sketch of different angles for the line-of-sight integration. The red circle represents the top of the loop. The blue circle represents the bottom of the loop. Angles vary by ±30 degrees. The central sketches are the same views as in Figure 3.5. The x and y views show angles around the side of the loop. The z views show angles around the top of the loop.

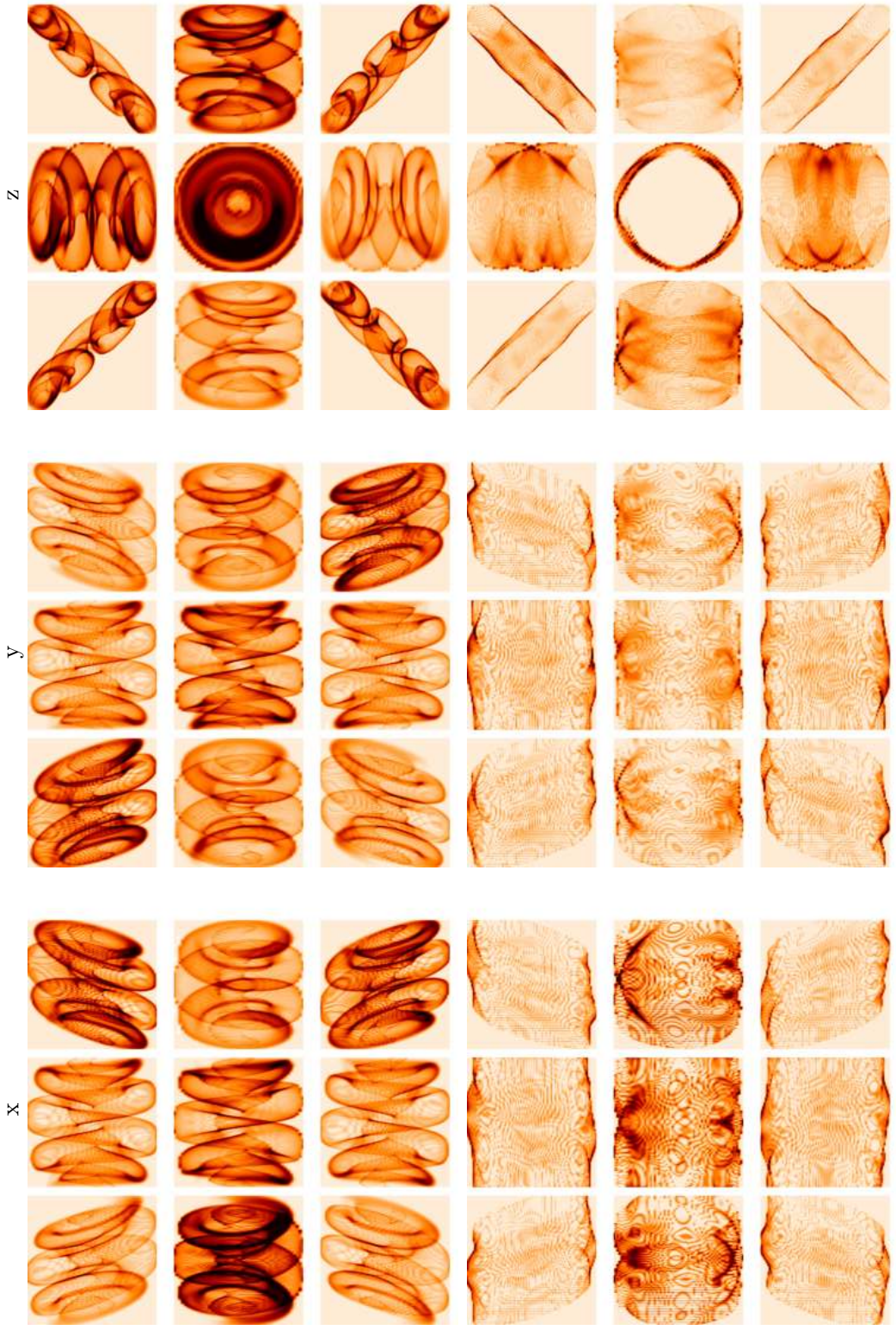

FIGURE 3.27: Simulation resolution intensities using Fe X from different angles of integration shown in the sketch Figure 3.26. Time is in seconds. The central images show the x, y and z views of the loop as seen in Figure 3.10.

3.2.9 Conclusions

Synthetic intensities have been calculated using several Hinode/EIS spectral lines for a 3D numerical simulation of a kink-unstable coronal flux rope. The investigated spectral lines are the O V, Fe X and Fe XV lines with temperature peaks of $\log(T) = 5.4$, 6.05 and 6.35.

Dense and sparse rasters When rasters were created moving the slit along the loop length only a small proportion of the loop was present in the raster. With the dense raster, there was not much difference in the intensity map for different points along the loop. One can see the growth of the loop and the increase in intensity on the loop edge and a small amount of interior structure is present towards the end of the rasters. However, it is difficult to discern any large scale structures. With the sparse raster, a large scale interior intensity brightening can be detected.

Sit-and-stare Placing the slit at a fixed location along the loop, the growth of the loop becomes much more apparent. The width of the loop is plotted against time for the different spectral lines. The growth is largest in the cooler O V line and smallest in the hotter Fe XV line. This is because a combination of parallel thermal conduction and reconnection act to effectively spread heat radially outwards [Botha et al., 2011], activating the cooler lines first. The loop growth is fairly rapid initially then becomes slower as the loop begins to relax. It is found that this is an overestimate of the loop width, compared to the simulation resolution results. The spatial degradation forces intensities into blocks of 1 arcsecond, and the time integration detected the largest width in the time frame as the loop edge. When the loop is changing rapidly, e.g. $t = 261$ seconds, this results in an overestimate of the loop by approximately 2 Mm. After time $t \approx 400$ seconds, the loop growth is far less rapid and the loop width observed by the raster is closer to the simulation resolution results.

Doppler velocities The dense raster located at the centre of the loop observed oppositely directed Doppler velocities. This corresponds to the velocity being guided along a twisted interior magnetic field in the simulation. The observed Doppler velocity in the raster is comparable to the simulation velocity component in the line-of-sight. With the sit-and-stare mode, histograms of the Doppler velocities show that as time increases there is a decrease in the peak at $v = 0$. This is because as the loop expands it fills the domain, reducing the number of counts at $v = 0$. The maximum magnitude of the Doppler velocities becomes smaller as time increases. This is due to the loop becoming less active.

Summary There are several qualities of a kink-unstable coronal flux rope that can be detected observationally using Hinode/EIS, namely the growth of the loop, the increase in intensity towards the edge of the loop, and the reduction in maximum Doppler shift as time advances. However, the exposure time of Hinode/EIS is too large to capture the small, transient features present in the simulation.

3.2.10 DKIST/DL-NIRSP

One can also generate intensity maps based on the contribution functions from future instruments. Intensity and Doppler shifts have been calculated for several lines from the off-limb coronal mode of the DKIST/DL-NIRSP (Daniel K Inouya Solar Telescope/D-iffraction limited - Near Infrared SpectroPolarimeter) [Keil et al., 2010]. Information regarding this observing mode of DKIST/DL-NIRSP can be found in Appendix A. The lines we will be considering are shown with their wavelengths and temperature peaks in Table 3.2, and the temperature response function is in Figure 3.28. The synthesised response from the Fe XI and the Si X spectral lines is very similar so the intensities using the Fe XI spectral line are omitted.

	Wavelength (Å)	Temperature peak (log(T) K)
S IX	12523.48	6.05
Fe XI	7894.03	6.15
Si X	14305.00	6.15
Fe XIII	10749.00	6.25

TABLE 3.2: DKIST/DL-NIRSP lines

DKIST/DL-NIRSP will have a pixel size of 0.5 arcsecond squared, a field-of-view (FOV) of 28×19 arcsecond, and a time exposure of approximately 22 seconds. A mosaic can be made by moving the FOV along the loop after each exposure to create additional tiles of the same size FOV.

3.2.10.1 Mosaic configuration

When using the DKIST/DL-NIRSP contribution functions, we will not consider the full loop. Instead we consider three mosaic tiles of the same FOV as the instrument. The location of these tiles is shown in Figure 3.29. The three tiles are located around the centre of the loop. We will refer to these are 'left', 'centre' and 'right' tiles.

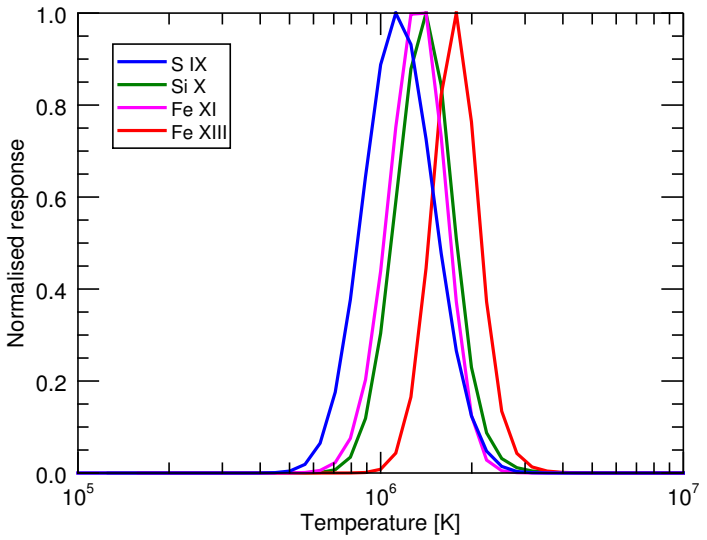

FIGURE 3.28: Contributions functions for the synthesised spectral lines of DKIST/DL-NIRSP.

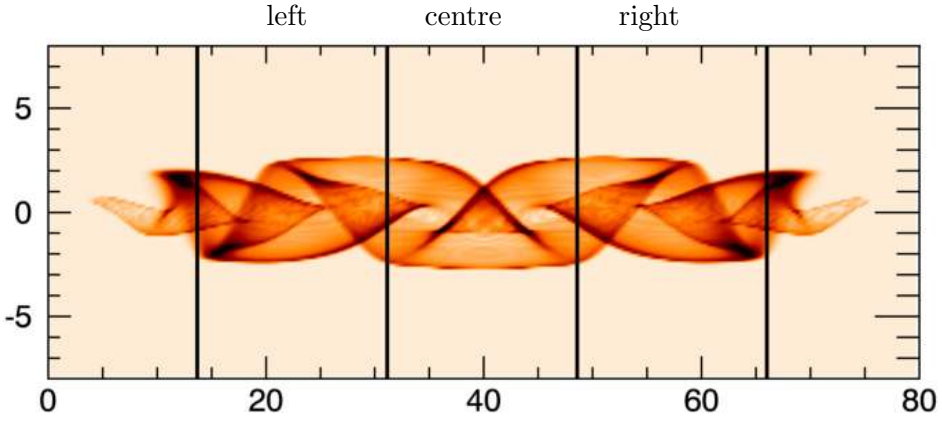

FIGURE 3.29: A contour of the intensity of the loop at time $t = 261$ seconds using the Fe XIII spectral line. The four black lines make the edge of the three mosaic tiles investigated in this section.

3.2.10.2 Tile in mosaic mode

A moving mosaic is constructed by creating three panels at the instrument FOV. Time is integrated to match the exposure time of DKIST/DL-NIRSP. The three panels are located at the centre of the loop, and adjacent to it. The mosaic scans left to right such that time advances left to right. Each tile has an exposure time of 22 seconds. After the right tile is scanned, the mosaic sequence restarts at the new time on the left tile. These are shown for the S IX, Si X and Fe XIII spectral lines in Figures 3.30, 3.31 and 3.32 respectively.

A considerable amount of structure is present in all spectral lines. Initially the structures in the loop are very short lived so cannot be traced from one mosaic tile to the next. Later on in the simulation, the structures are relatively longer lived and can be traced across multiple tiles. The growth of the loop is clearly identifiable across the tiles.

There appears to be little difference between the intensity maps for different spectral lines. This is because lines have a reasonably similar temperature range and are all activated by heating/cooling plasma. When an event occurs, it generates heat then cools. This temperature evolution can lead to an observational response with progressively cooler spectral lines. If this phenomena occurs in a time frame that is smaller than the exposure time, then all three spectral lines are activated simultaneously. Differences in the intensity maps show more general heating/cooling and are more apparent towards the end of the simulation where the loop is becoming less active.

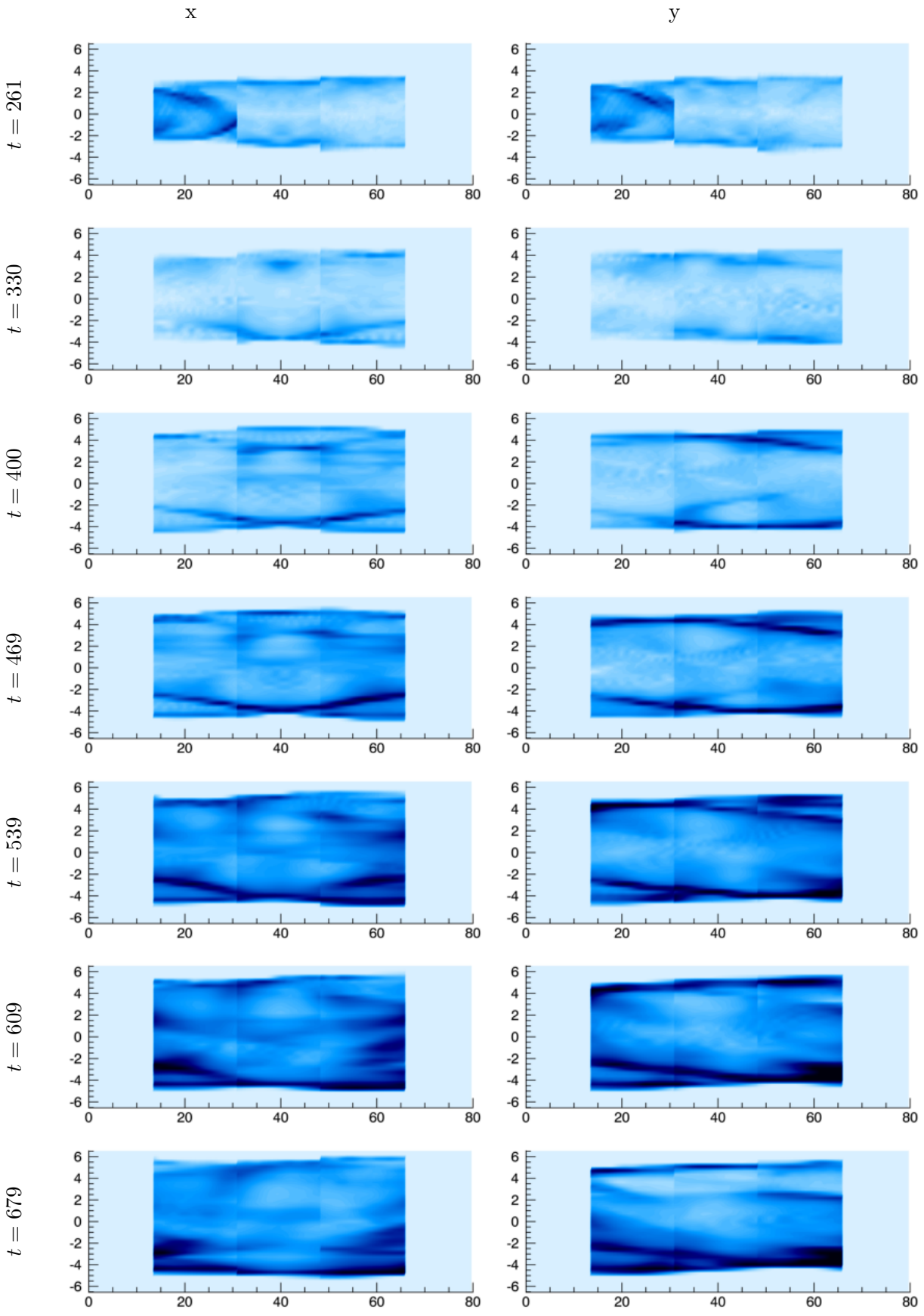

FIGURE 3.30: Intensities S IX using a moving mosaic. The time indicates the starting time of the exposure on the left tile. Time is in seconds.

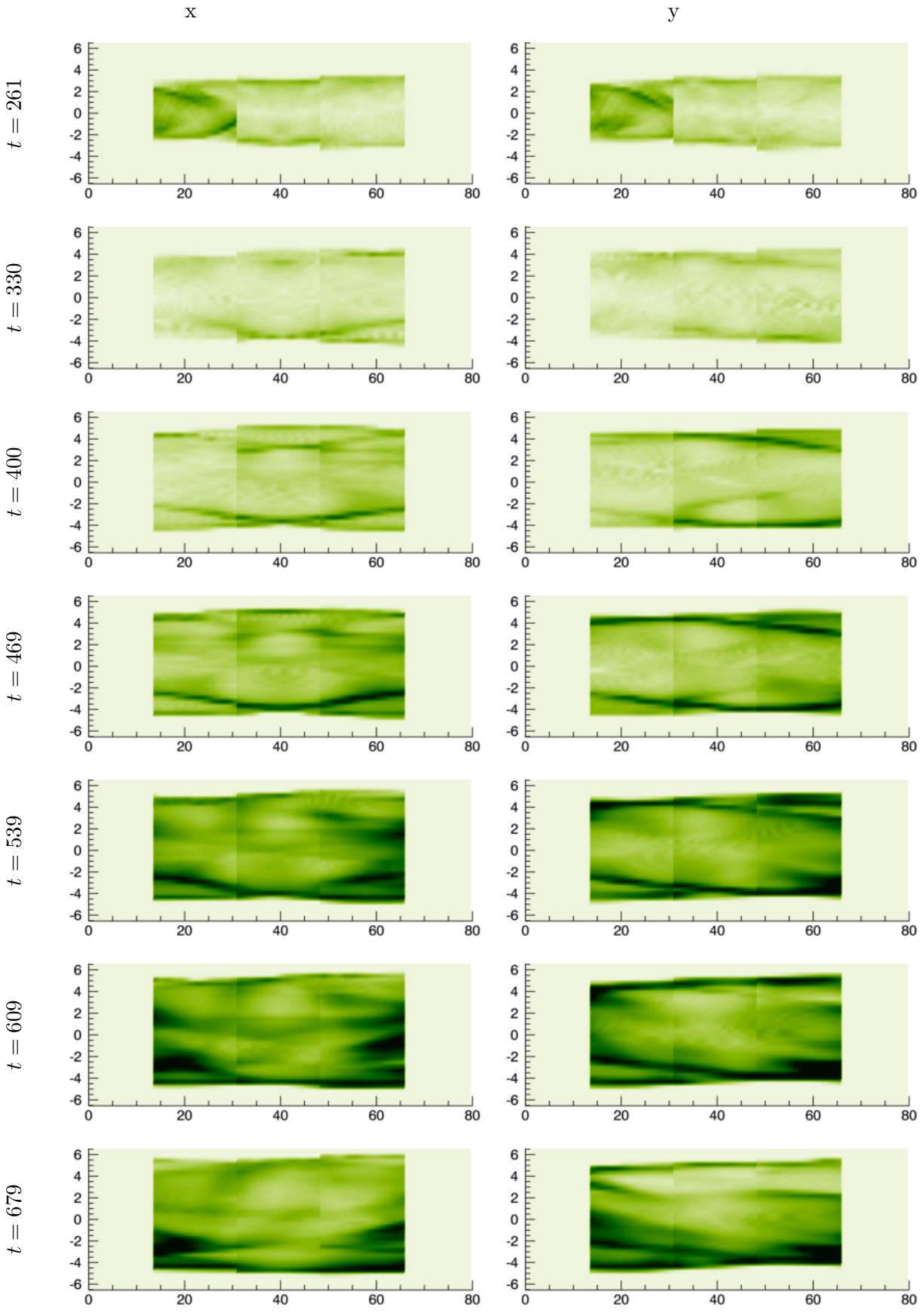

FIGURE 3.31: Intensities Si X using a moving mosaic. Time is in seconds.

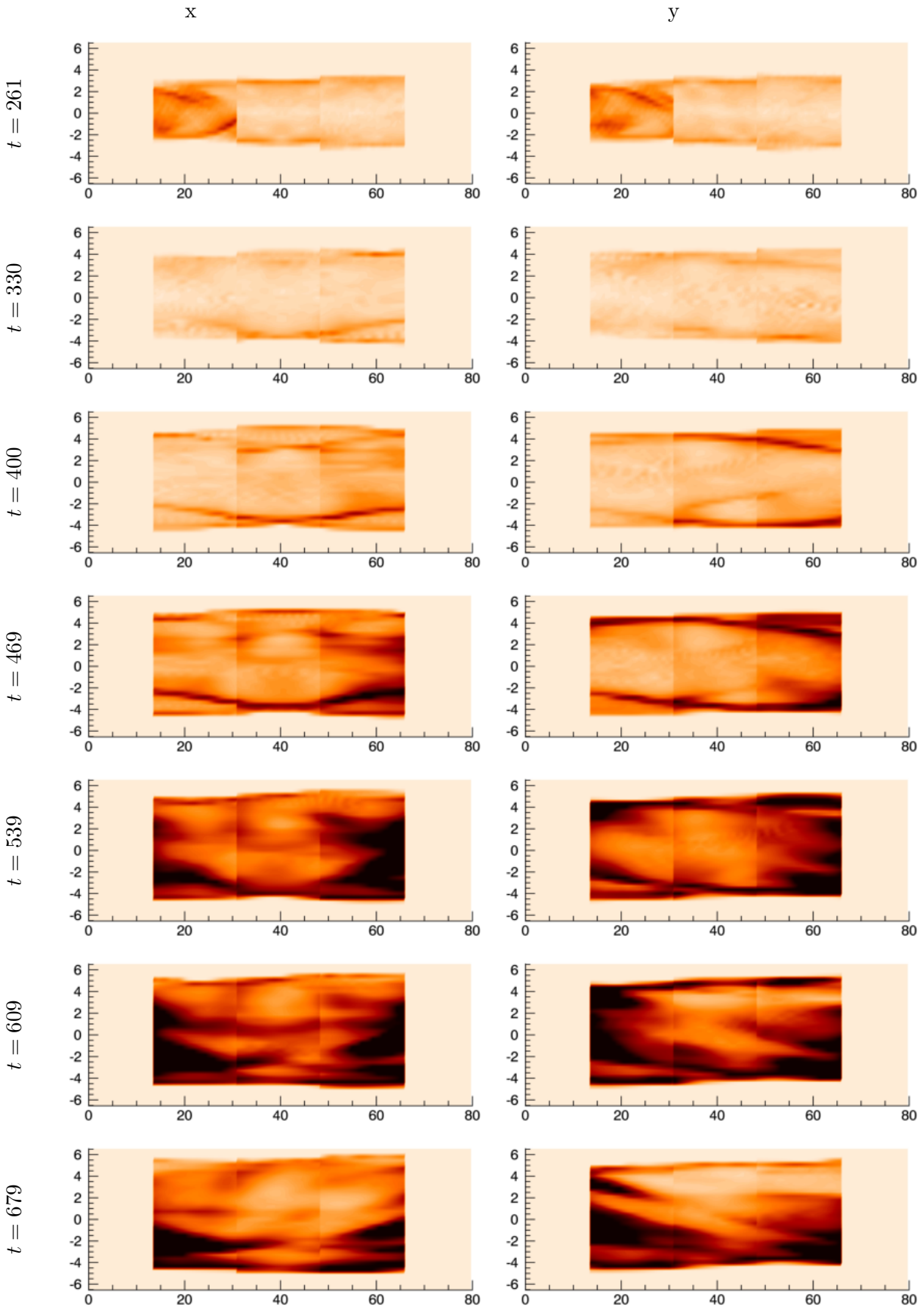

FIGURE 3.32: Intensities Fe XIII using a moving mosaic. Time is in seconds.

3.2.10.3 Tile in sit-and-stare mode

Now the sit-and-stare mode of the instrument will be investigated. The intensity maps using the central tile are shown in Figure 3.33 for the S IX (blue), Si X (green) and Fe XIII (red) spectral lines when integrated in the x-direction (left) and y-direction (right). Note that only selected times are shown.

Again there does not appear to be much qualitative difference between the intensity maps for the different lines. This is because the time averaging acts to average out many of the heating/cooling events.

The relatively low exposure time for the FOV manages to capture some of the small scale transient phenomena present in the simulation, including the breakdown of the kink-unstable loop. Interior structure is also present and the evolution of the loop can be clearly seen in the intensity maps.

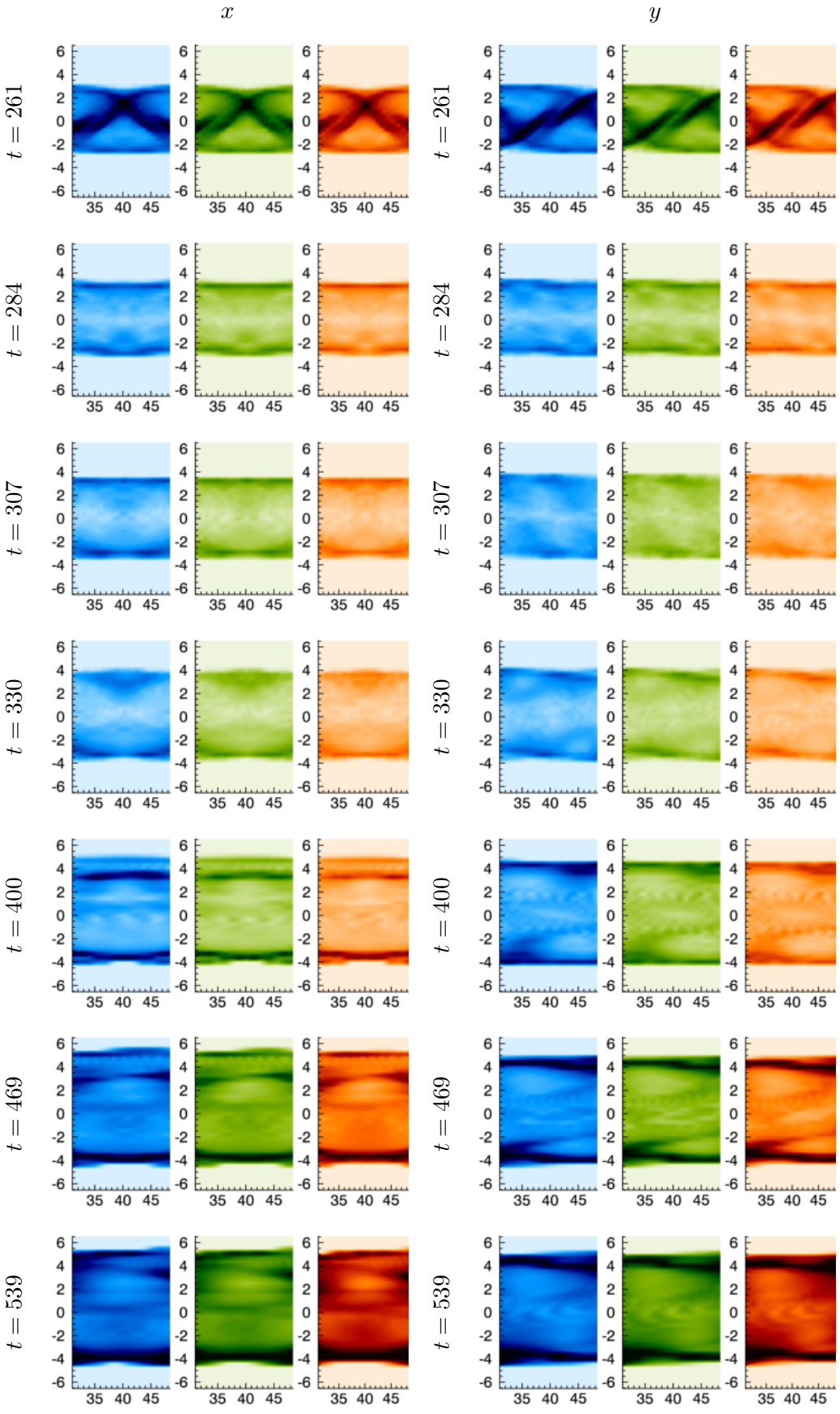

FIGURE 3.33: Intensities sit-and-stare using S IX (blue), Si X (green), and Fe XIII (red) integrated in x-direction (left) and y-direction (right). Mosaic tile is located in the centre of the loop. Note that only selected times are shown. Time is in seconds.

3.2.10.4 Conclusions

The future DKIST/DL-NIRSP instrument appears to be capable of capturing the behaviour of a kink-unstable flux rope. The moving slit detects the initial twist of the loop and features can be tracked across tiles for late times. The sit-and-stare intensities give a large amount of information about the loop in both time and space, showing many small scale features.

3.3 Summary

This chapter investigated using LOS integration to synthesise the observational signature of the coronal velocity signature as a results of the chromospheric resonator, and a coronal kink-unstable flux rope.

3.3.1 Resonator

The chromospheric resonator investigated in Chapter 2 created a coronal velocity signature that is directly correlated with the size of the chromospheric cavity. LOS integration was performed to investigate the observational signatures created by the resonances using several response functions from SDO/AIA and contribution function from Hinode/EIS and SOHO/SUMER.

It was found that the LOS velocity spectra contained different properties to the single point analysis performed in Chapter 2. As the chromospheric cavity increased in size, the broadband of excited frequencies became narrower. This provides a potentially useful diagnostic for indirectly measuring the chromospheric cavity size.

3.3.2 Kink-unstable coronal flux rope

LOS integration was also performed to generate the observational signatures from a 3D simulation of a kink-unstable coronal flux rope using Hinode/EIS.

The main results using Hinode/EIS were:

1. The growth in loop radius was observed in the intensity maps using both a moving raster and the sit-and-stare mode. Comparing the measured width in the sit-and-stare mode to the width measure in the simulation resolution results we find that the loop width is overestimated in the sit-and-stare intensity maps.

2. The dense raster of Doppler velocities located near the centre of the loop showed oppositely directed magnetic fields. This corresponds to velocity being guided along a twisted magnetic field line in the simulation.

3. The exposure time of Hinode/EIS is too long to capture small scale transient phenomena in the loop.

When observing the loop using the expected DKIST/DL-NIRSP spectral lines, there was a large amount of small scale structure present in the intensity maps. This is due to the small exposure time and high resolution. The growth of the loop is clearly visible in both the moving mosaic and the sit-and-stare mode.

Future work involves analysing the intensity and Doppler velocity as observed by the selected spectral lines to predict the observational signatures of a kink-unstable coronal flux rope using the DKIST/DL-NIRSP instrument.

Chapter 4

Onset of 2D Magnetic Reconnection at Different Atmospheric Heights

The final branch of this thesis investigates the early behaviour of a 2D magnetic reconnection event and how this changes under photospheric, chromospheric and coronal conditions. Waves and flows are ubiquitous in the solar atmosphere and can encounter current sheets, triggering reconnection. This is modelled by the external velocity driver used in this chapter, which allows the early behaviour of magnetic reconnection to be studied in a naturalistic manner. This work has been submitted for publication as Snow et al. [2016].

4.1 Introduction

Magnetic reconnection is a topological restructuring of a magnetic field caused by the change in connectivity of its field lines [Priest and Forbes, 2000]. In this process, the magnetic energy is converted into kinetic energy and thermal energy of the plasma. Reconnection plays an important role in many dynamical phenomena in the solar atmosphere including the photosphere, e.g. Ellerman bombs [Ellerman, 1917, Nelson et al., 2013, Reid et al., 2016], the chromosphere, e.g. penumbral microjets [Katsukawa et al., 2007] and calcium jets [Morita et al., 2010, Shibata et al., 2007], and the corona, e.g. x-ray jets [Savcheva et al., 2007, Shibata et al., 1992] and flares [Moore et al., 2001]. Comprehensive reviews of magnetic reconnection can be found in Pontin [2012], Yamada et al. [2010], Zweibel and Yamada [2009].

There are several models for reconnection which can be separated broadly into two categories: slow and fast. The model for Sweet-Parker reconnection [Parker, 1957, Sweet, 1958] has a long diffusion region between oppositely directed magnetic fieldlines. The rate at which the magnetic fields diffuse predicts an Alfvén Mach number proportional to the inverse root of the Lundquist number, i.e. $M_A = S^{-1/2}$ (derivation shown in Section 1.6.1). In astrophysical plasmas, the Lundquist number can be many orders of magnitude larger than unity, resulting in a very small Alfvén Mach number M_A, hence the name slow reconnection. Slow reconnection is not sufficient to explain observed solar phenomena. Improvements have been made on the Sweet-Parker model to create fast reconnection models, e.g. Petschek [Petschek, 1964] and flux pile-up models [Priest and Forbes, 1986]. The Petschek model achieves fast reconnection by including two pairs of slow-mode shocks which act to carry flow away from the diffusion region. This results in a diffusion region that shortens as the inflow rate increases (see Section 1.6.2 for derivation). Flux pile-up models have a rise in magnetic field energy entering the diffusion region and a slow-mode expansion. In the flux pile-up models, the diffusion region becomes long and thin, and the reconnection rate can exceed the maximum Petschek reconnection rate [Priest and Forbes, 1986]. Reconnection papers typically initiate reconnection using an interior trigger, that is various perturbations specified as initial conditions that are centred on the current sheet. These include invoking locally enhanced resistivity or small velocity perturbations inside the current sheet. This directly influences the reconnection process and prohibits study of the early behaviour.

The evolution of a tearing-mode unstable reconnection event has been studied via the incompressible Taylor problem, where a small boundary perturbation is applied to a stable slab plasma [as reviewed in Bhattacharjee, 2004]. This is typically referred to as forced/driven reconnection. The linear and non-linear phases of this process can be studied to analyse the evolution of a reconnection event, and the formation of current sheets and magnetic islands [Wang and Bhattacharjee, 1992]. Numerical simulations have been performed to study the Taylor problem [Fitzpatrick, 2003] yielding results consistent with analytical solution [e.g. Hahm and Kulsrud, 1985]. This is different from the problem investigated in this chapter; we use a different type of driver and a different initial magnetic field profile.

In the solar chromosphere, the temperature and density configuration allow both neutral and ionised particles to exist, hence the plasma is partially ionised (Section 1.6.3). This results in Cowling resistivity that acts perpendicular to magnetic field, in addition to Spitzer resistivity. Previous work investigating partial ionisation includes flux emergence [Arber et al., 2007, Leake and Arber, 2006], wave dissipation [Leake et al., 2005, Zaqarashvili et al., 2013], tearing mode instabilities [Leake et al., 2012, Zweibel, 1989], chromospheric current sheet collapse [Arber et al., 2009] and formation [Brandenburg

and Zweibel, 1994], and the evolution of slow mode shocks [Hillier et al., 2016]. For partially ionised coalescing loops it has been shown that the inclusion of ionisation increases the amount of magnetic flux reconnected but due to the change in ion pressure, the reconnection rate remains unchanged [Smith and Sakai, 2008]. The effects of partial ionisation can also be used to explain the existence of penumbral microjets [Sakai and Smith, 2008]. For strong chromospheric magnetic field strengths, the length scale of a tearing mode instability can become comparable to the kinetic length scales that are thought necessary for fast reconnection [Singh et al., 2015]. For chromospheric reconnection the Hall term ($\mathbf{J} \times \mathbf{B}$) in Ohm's law can generally be neglected [Malyshkin and Zweibel, 2011].

In this chapter, 2D reconnection is triggered using a sub-Alfvénic velocity driver specified perpendicular to the Harris current sheet, far away from the centre of the domain. This external driver allows us to study the early onset of magnetic reconnection in a naturalistic manner. Reconnection start-up and development is investigated in photospheric (weakly ionised), coronal (fully ionised) and chromospheric (partially ionised) atmospheric conditions. In order to fully understand the differences between chromospheric, coronal and photospheric reconnection, a baseline model is presented and analysed, and then a parameter study is performed. This allows the effects of each parameter to be studied independently.

4.2 Computational set-up and initial conditions

Simulations have been performed using Lare3d [Arber et al., 2001] in the (y, z) Cartesian plane, with an invariant x-direction. Lare3d solves the compressible, resistive MHD

equations given by

$$\frac{\partial \rho}{\partial t} = -\nabla \cdot (\rho \mathbf{v}), \tag{4.1}$$

$$\frac{\partial \mathbf{v}}{\partial t} + \mathbf{v} \cdot \nabla \mathbf{v} = \frac{1}{\rho}\mathbf{J} \times \mathbf{B} - \frac{1}{\rho}\nabla P, \tag{4.2}$$

$$\frac{\partial \mathbf{B}}{\partial t} = -\nabla \times \mathbf{E}, \tag{4.3}$$

$$\frac{\partial \epsilon}{\partial t} + \mathbf{v} \cdot \nabla \epsilon = -\frac{P}{\rho}\nabla \cdot \mathbf{v} + \frac{\eta}{\rho}J^2 + \frac{\eta_\perp}{\rho}J_\perp^2, \tag{4.4}$$

$$\mathbf{E} + \mathbf{v} \times \mathbf{B} = \eta \mathbf{J} + \eta_\perp \mathbf{J}_\perp, \tag{4.5}$$

$$\nabla \times \mathbf{B} = \mu_0 \mathbf{J}, \tag{4.6}$$

$$P = \frac{\rho k_B T}{\mu_m}, \tag{4.7}$$

$$\epsilon = \frac{P}{\rho(\gamma - 1)} + (1 - \xi_n)\frac{\chi_i}{\bar{m}}, \tag{4.8}$$

$$\eta_\perp = \frac{\xi_n^2 \mathbf{B}^2}{\alpha_n}, \tag{4.9}$$

$$\mu_m = \frac{\bar{m}}{2 - \xi_n}, \tag{4.10}$$

where α_n is the effective neutral collisional rate.

The neutral fraction ξ_n is calculated using the modified Saha equation [Athay and Thomas, 1961]. The neutral fraction is a function of density and temperature, i.e. $\xi_n = \xi_n(\rho, T)$, as implemented in Lare3D by Leake et al. [2005]. The modified Saha equation and its implementation is shown in Section 1.6.3. Spitzer resistivity η is uniform across the domain.

A sketch of the computational domain is shown in Figure 4.1, where the damping region is indicated by the shaded region. The initial magnetic field is specified using a Harris current sheet defined as

$$B_y(z) = \tanh(z)$$

where B_y is the magnetic field component in the (y, z) Cartesian plane. $B_z = 0$ initially. The maximum current is in the centre of the domain indicated by the dashed line at $z = 0$ in Figure 4.1.

For a uniform temperature the pressure balance equation can then be solved analytically (as shown in Section 1.6.4) to find the equilibrium density as

$$\rho = \frac{\rho_0}{\beta}\cosh^{-2}(z) + C$$

for initialisation density ρ_0 and plasma-β. The normalised C is chosen as unity.

Grid size is $\Delta y = 0.0625$ by $\Delta z = 0.03125$ with the domain spanning $-16 < y < 16$ and $-8 < z < 8$. The grid resolution is 512×512 cells. A grid convergence test was performed and there are no significant quantitative or qualitative changes in the output for increased resolution therefore 512×512 is sufficient. The simulation domain in dimensionless units is 32×8 (neglecting the damping regions). This corresponds to a physical extent of 320×80 km. This domain size is sufficiently large any shocks produced in the simulation do not reach the outflow boundaries. The small physical extend of the simulation also allows us to consider an isolated parameter regime in the solar atmosphere, neglecting variations with height.

The boundaries at $y = \pm 16$ are zero gradient.

The reconnection is triggered by sub-Alfvénic velocity drivers specified far away from the centre of the current sheet at $4 \leq z \leq 8$ and $-8 \leq z \leq -4$. Both velocity drivers are of the form

$$v_z(y) = Ae^{-y^2/3}. \tag{4.11}$$

This velocity propagates across the domain dragging magnetic field energy towards the centre of the domain and triggers the reconnection.

When the velocity fronts meet, a fast-mode reflection occurs. It propagates towards the driven boundary and if left untreated bounces off the upper boundary and back into the reconnection region causing unwanted phenomena. To limit the influence of the reflection on the simulation, a damping region is specified between $-8 \leq z \leq -4$ and $4 \leq z \leq 8$. One can damp out the unwanted perturbation by acknowledging the velocity in this region has two components, the driver v_d and the perturbation v_p, i.e. $v = v_d + v_p$. Kinetic energy damping is applied to v_p only and the driven velocity is applied uniformly between $-8 \leq z \leq -4$ and $4 \leq z \leq 8$. v_p is damped according to:

$$v_p = 0.5|1 - cos(0.25\pi(|z| - 4))|. \tag{4.12}$$

This gradually reduces the kinetic energy of the perturbation component of velocity towards the $z = \pm 8$ boundaries of the simulation domain. In this damping region, $v_z(y, 4 \leq z \leq 8)$ is calculated according to Equation (4.11).

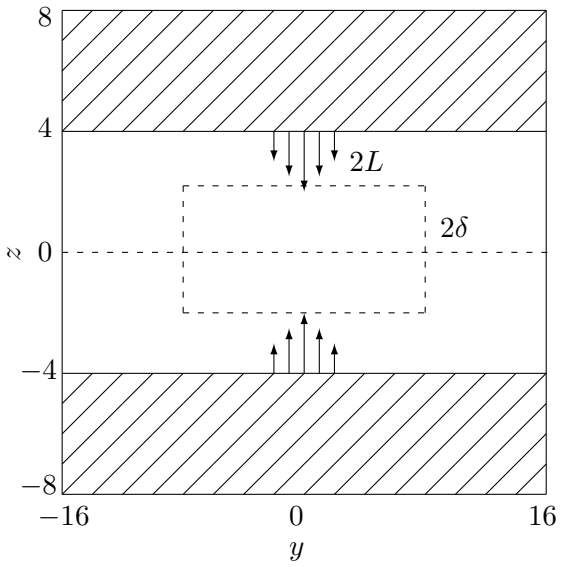

FIGURE 4.1: Sketch of the computational domain. y ranges between ± 16, z ranges between ± 8. The drivers are defined for $|z| \geq 4$, denoted by the arrows. Shaded region indicates the damping zone, where perturbation kinetic energy is damped. A reconnection region of width 2δ and height $2L$ is fitted to the domain. The line $z = 0$ is the location of the Harris current sheet.

4.3 Diagnostics

4.3.1 Reconnection region

A reconnection region of width 2δ and length $2L$ can be fitted to the domain, see Figure 4.1. δ is estimated by looking at the half width at half maximum (HWHM) of the current density $\mathbf{J}$. L is estimated by the point along the centre line ($z = 0$) at which the outflow velocity is maximum.

4.3.2 Electric field

The electric field $\mathbf{E}$ is calculated using Ohm's law, Equation (4.5). In our computational domain there is only one non-zero component of $\mathbf{E}$ in the x-direction, i.e. $\mathbf{E} = (E_x, 0, 0)$. The electric field can be separated into a diffusion term $\eta\mathbf{J} + \eta_\perp \mathbf{J}_\perp$ and an advection term $\mathbf{v} \times \mathbf{B}$. Note that the only non-zero component of $\mathbf{J}$ is J_x. This is equivalent to $J_\perp$ for our 2D simulation.

4.3.3 Energy flux

The reconnection process converts magnetic energy ϵ_M to kinetic energy ϵ_K, and can result in heating, signified by a rise in internal energy ϵ_I. It is therefore important to

calculate these quantities.

The kinetic energy is calculated by $\epsilon_K = \frac{1}{2}\rho v^2$. The flux of this through the reconnection region is calculated by $\int v_y \epsilon_K dz + \int v_z \epsilon_K dy$ along the boundaries of the reconnection region. The Ohmic heating is calculated by ηJ^2.

Internal energy ϵ_I is defined by Equation (4.8). However the ionisation energy term is only important when there is large variation of the neutral fraction ξ_n in the domain. This is not the case for our simulations. Internal energy can therefore be rewritten as

$$\epsilon_I = \frac{P}{\rho(\gamma - 1)} = \frac{k_B T}{\mu_m(\gamma - 1)}. \tag{4.13}$$

Total internal energy can be investigated by integrating ϵ_I over the area of the reconnection region $\epsilon_{I(total)} = \int\int \epsilon_I dy dz$. Because the reconnection region changes in size during the simulation, a more meaningful quantity is to divide this by the size of the reconnection region to get the average internal energy in the reconnection region, i.e. $\epsilon_{I(average)} = \epsilon_{I(total)}/4\delta L$.

4.4 Baseline model (coronal environment)

A baseline model will be considered first to provide a reference point. The case chosen will be a coronal type atmosphere driven with a sub-Alfvénic velocity. The key parameters for this study are in Table 4.1. Note that the Lundquist number S is the Lundquist number on the driven boundary. This is the largest value of S in the domain. The plasma-β is also the value on the driven boundary.

Parameter [Units]	Symbol	Value
Plasma-β		0.002
Length Normalisation [m]	l_0	10^4
Temperature [K]	T	10^6
Resistivity [Ωm]	η	10^{-6}
Time normalisation [s]	Δt	24
Alfvén Mach number	$M_{A(driver)}$	0.003
Lundquist number	S	2.5×10^{10}

TABLE 4.1: Baseline parameters. Note that the Lundquist number above is the maximum value in the domain which occurs on the driven boundaries. In the reconnection region the maximum Lundquist number is $S < 10^7$.

The process can be separated into three phases: reflection (Figure 4.2), development (Figure 4.3) and reconnection (Figure 4.4). In this section each phase is discussed in

order to understand the evolution of the system. More quantitative analysis of the baseline model is provided in subsequent sections.

4.4.1 Reflection phase

The driven velocity propagates from $z = \pm 4$ at the local fast-mode speed towards the current sheet located at $z = 0$. The equilibrium Alfvén speed decreases towards the centre of the domain because the pressure increases and the magnetic field strength decreases. The initial sound speed is constant across the domain because the temperature is constant. The fast-mode speed is a function of the Alfvén speed and the sound speed and decreases towards the centre of the domain. This means that the driven wave steepens as it approaches the centre of the Harris current sheet. The velocity amplitude of the driver is chosen to prevent this wave steepening into a shock. When these wavefronts hit the centre of the Harris current sheet they trigger a pair of fast-mode reflection that propagate backwards towards the drivers (Figure 4.2). The majority of the kinetic energy of the fast-mode reflection is damped out in the damping region.

4.4.2 Development phase

In the wake of this fast-mode reflection, the current increases and the reconnection region begins to form (Figure 4.3). There is a small amount of outflow at the start of this phase, however there is no electric field increase associated with this. Therefore this is only a fluid process as a result of the driver as opposed to a magnetic process. Towards the end of this phase, there is a stable outflow and magnetic field lines begin to reconnect.

4.4.3 Reconnection phase

For late times, there is clear acceleration of the plasma exiting the reconnection region (Figure 4.4). The reconnection reaches a linear phase in terms of reconnection region size, with L increasing linearly with time and δ decreasing linearly with time. The reconnection event has qualities of both Sweet-Parker and Petschek models. The reconnection region is elongated and narrow like in Sweet-Parker reconnection, however there are weak slow-mode shocks that form on the interface between the inflow and outflow flow regions similar to Petschek. The inflow velocity is constant at late times, however the magnetic field entering the reconnection region is increasing. This creates a reconnection process that behaves like the flux-pile up model of Priest and Forbes [1986]. A contour of the perturbation current $J_x - J_x(t = 0)$ and streamlines of normalised magnetic field at time $t = 600/\Delta t$ are shown in Figure 4.5.

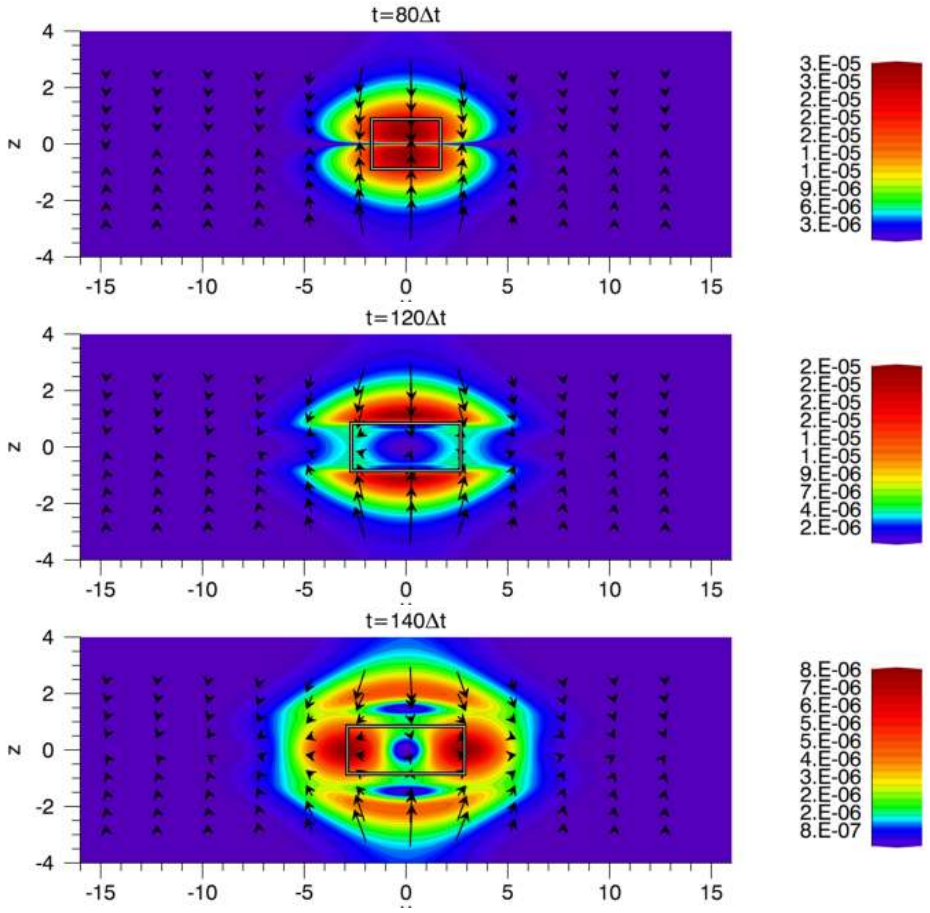

FIGURE 4.2: Fast-mode reflection shown in kinetic energy at times 80Δt, 120Δt and 140Δt for the baseline coronal atmosphere. The white box frame denotes the reconnection region.

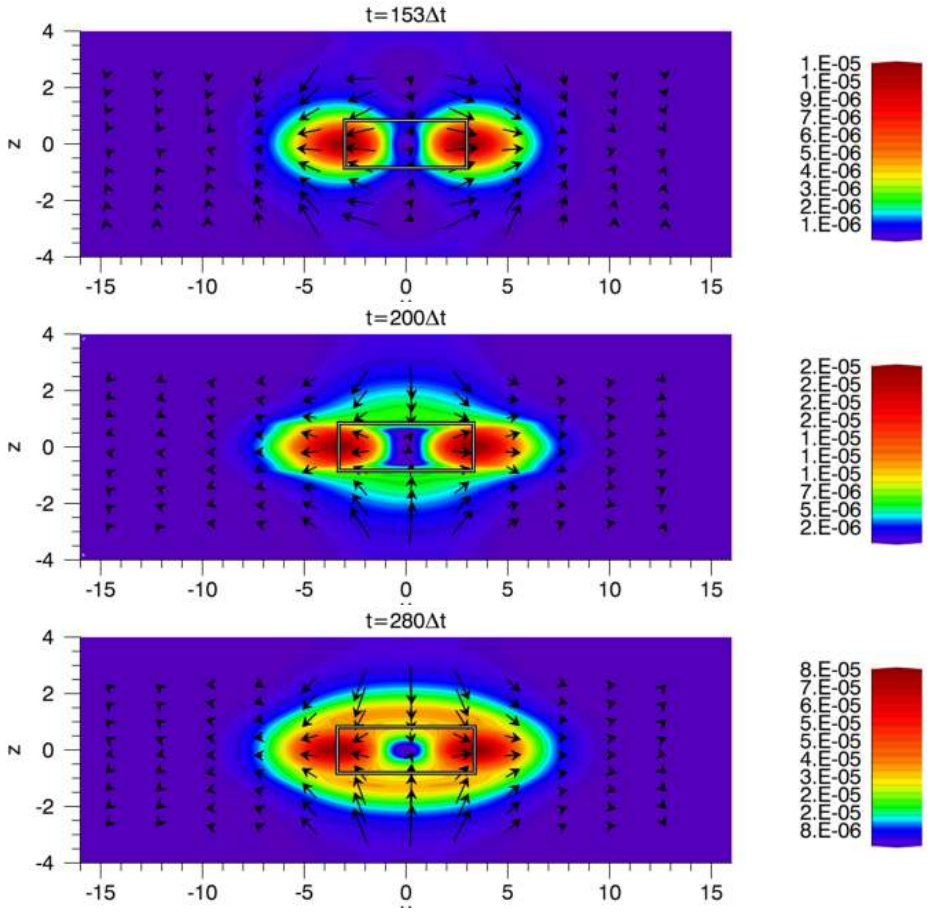

FIGURE 4.3: Development phase shown in kinetic energy at times 153Δt, 200Δt and 280Δt for the baseline coronal atmosphere. The white box frame denotes the reconnection region.

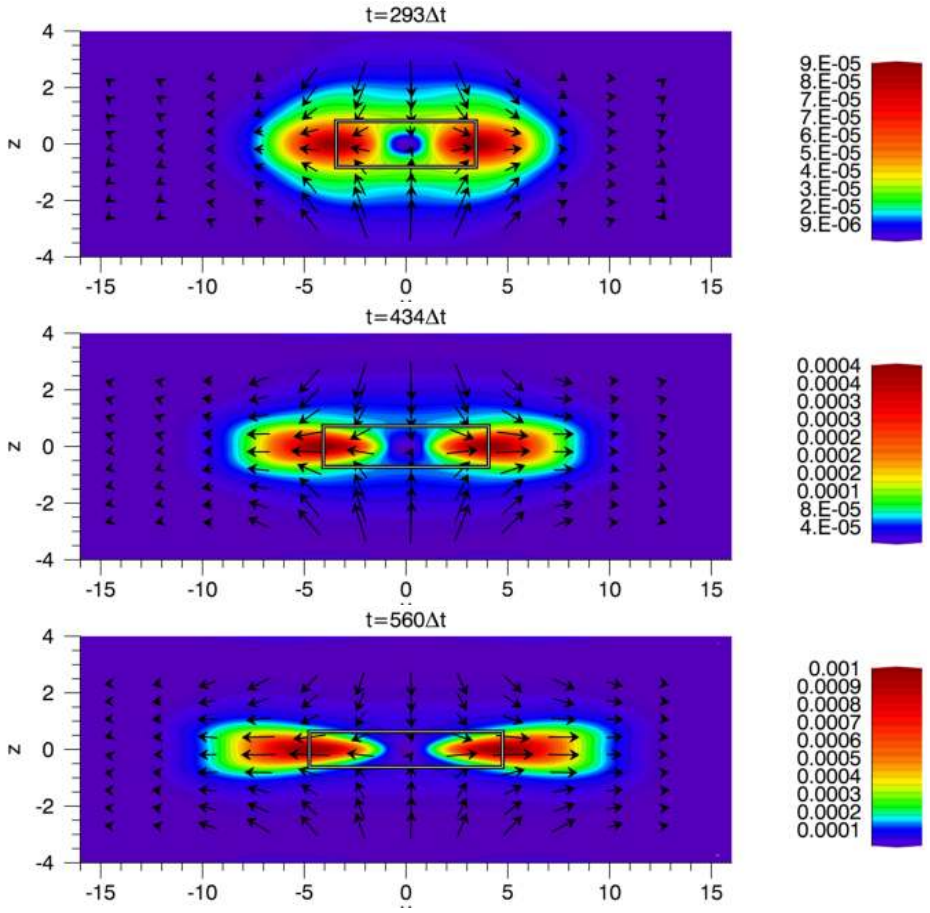

FIGURE 4.4: Reconnection phase shown in kinetic energy at times 293Δt, 434Δt and 560Δt for the baseline coronal atmosphere. The white box frame denotes the reconnection region.

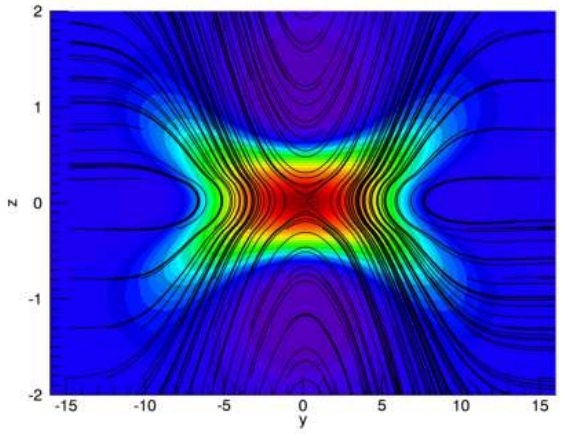

FIGURE 4.5: Coloured contour of the perturbation current density $J_x - J_x(t = 0)$ (red represents a large change, blue represents a small change) and streamlines of the normalised magnetic field at time $t = 600/\Delta t$.

4.5 Velocity dependence

Now that the baseline coronal model has been presented, variations from this can be considered. First the dependence on the magnitude of the velocity driver will be considered. Three different velocity magnitudes have been tested. The velocities have been chosen to prevent shocks occurring on the inflow. The driver Alfvén speed is shown is Table 4.2. The high driver considered here is the same as the baseline case in the previous section.

Driver name	Alfvén Mach number
High	0.003
Medium	0.001
Low	0.0003

TABLE 4.2: Driver Alfvén Mach numbers for the velocity dependence test.

4.5.1 Reconnection region

The half-width δ and half-length L of the reconnection region are shown in Figure 4.6. After the initial development phase, the half-length L of the reconnection region increases and the half-width δ decreases. All tested driver velocities influence L similarly until approximately $t = 400\Delta t$. There seems to be two linear post-development phases in the diffusion half-length L. The first between $250\Delta t$ and $350\Delta t$ during which all velocities yield the same growth rate for L. However after $t = 400\Delta t$ the high driver demonstrates a steeper growth rate for L.

The diffusion half-width δ decreases linearly after $t = 250\Delta t$. The low driver velocity does not appear to affect δ.

4.5.2 Electric field

The maximum electric field in the reconnection region shows a significant difference between the three different velocity drivers in terms of magnitudes. However, all have reasonably similar behaviour during the reflection and reconnection phases, see Figure 4.7. There appears to be a sudden change in magnitude of the electric field that is dependent on the magnitude of the velocity driver. The electric field increases by approximately 4, 2 and 1 orders magnitude for the high, medium and low drivers respectively. By looking at the components of the electric field at the location of the maximum electric field in Figure 4.7(b), one can see that the steep gradient change occurs in the $\mathbf{v} \times \mathbf{B}$ term. This

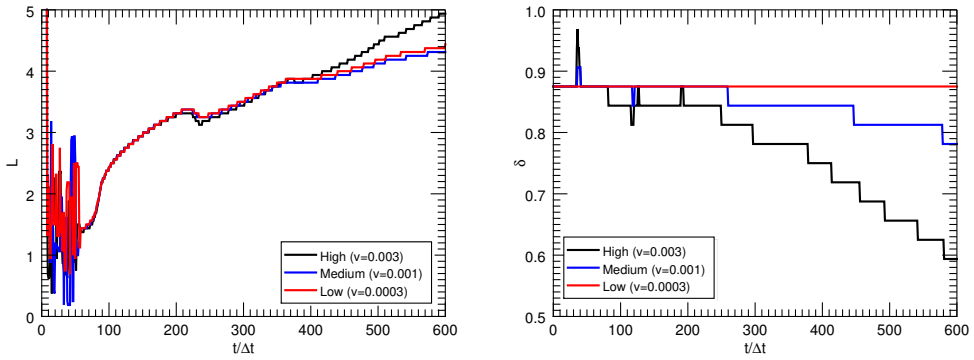

(a) (b)

FIGURE 4.6: (a) Half-length L and (b) half-width δ of the reconnection region for the coronal case. L is calculated using the maximum outflow. δ is calculated as the HWHM the the current density

implies the advection process dominates late times. η is very small in this case so the diffusion term is also small. The $\mathbf{v} \times \mathbf{B}$ term shows the three distinct phases: reflection phase, development phase and reconnection phase.

During the reflection phase, the wavefront from the driver hits the centreline (at time $t = 80\Delta t$) and causes a fast-mode reflection. In the wake of this reflection the current sheet fluctuates in width towards a new equilibrium. This same process occurs for all three velocities tested. These fluctuations are present in the $\mathbf{v} \times \mathbf{B}$ component of Ohm's law, shown in Figure 4.7(b) by the damped oscillations between $t = 80\Delta t$ and $100\Delta t$.

One can also identify the end of the development phase in Figure 4.7(b) as the point where the $\mathbf{v} \times \mathbf{B}$ term becomes larger than the $\eta\mathbf{J}$ term. This occurs at a different time in all cases. Here some magnetic reconnection is occurring, however the process appears to be different in each case. To understand this, one must consider the components of $\mathbf{v} \times \mathbf{B}$ in the x-direction, i.e. $v_y B_z$ and $v_z B_y$. The magnetic field in the y-direction is far stronger than the z-direction and hence the effects of v_z are magnified when looking at $\mathbf{v} \times \mathbf{B}$. The high driver shows a plateau in the development region, approximately times $t = 120\Delta t$ to $200\Delta t$ in Figure 4.7(b). The pressure of the incoming velocity is sufficient to result in a velocity directed predominantly in the y-direction at the location of the maximum electric field. The low velocity driver increases in $\mathbf{v} \times \mathbf{B}$ during the development phase. This is because the pressure from the incoming velocity is insufficient to direct the flow in the y-direction. Instead the velocity flows predominantly along the magnetic field lines. The medium driver is a combination of these two effects.

During the reconnection phase, the $\mathbf{v} \times \mathbf{B}$ term dominates the diffusion term and slow-mode shocks begin to form. The difference between the magnitudes of the advection and

diffusion terms is dependent on the driver velocity. For the high driver the advection term is approximately 4 orders larger than the diffusion term.

The maximum electric field occurs at the centre of the domain when diffusion dominates. When advection dominates, the maximum electric field moves along the line $z = 0$ with the outflow. Note however the electric field variation along this line are small (less than an order of magnitude).

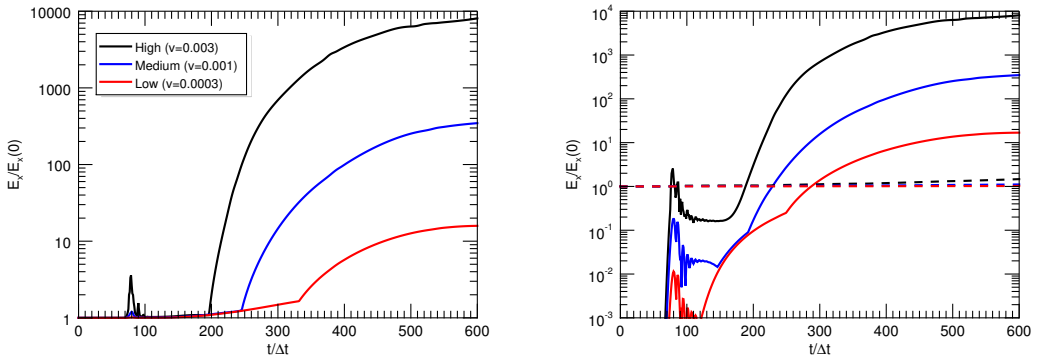

FIGURE 4.7: (a) Maximum electric field in the reconnection region for the coronal case for the different velocity driver magnitudes divided by the electric field at time t=0. (b) Components of the Ohm's law: $|\mathbf{v} \times \mathbf{B}|$ (solid line) and ηJ_x (dashed line) normalised by the electric field at time $t = 0$.

4.5.2.1 Electric field scaling with driver Alfvén Mach number

The electric field tends towards a maximum value for all tested driver Alfvén Mach numbers, see Figure 4.7(a). By plotting the driver Alfvén Mach number against the electric field value at the end time, a power law relationship can be fitted, see Figure 4.8. This power law has a gradient of approximately 2.7. This gives a direct relationship between the maximum electric field obtained and the driver Alfvén Mach number.

4.5.3 Energy flux through the reconnection region

Figure 4.9(a) shows the kinetic energy ratio $\epsilon_{K(in)}/\epsilon_{K(out)}$ along the edge of the reconnection region. All driver velocities give a ratio less than unity at late times indicating that there is acceleration of the plasma in the reconnection region. The peak in the kinetic energy ratio at times $t \approx 260\Delta t$ corresponds to the fast-mode reflection entering the reconnection region. This doesn't appear to have any effect on the reconnection process. The outflow velocity remains fairly linear however the inflow contains a few fluctuations, see Figure 4.9(b). These fluctuations in the inflow are due to the fast-mode

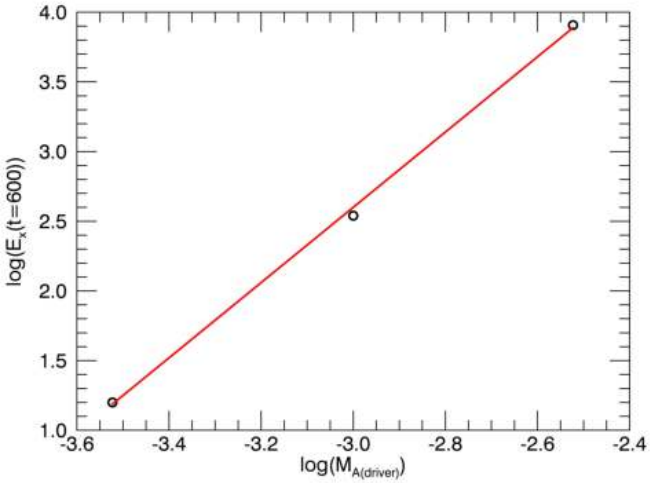

FIGURE 4.8: Log-log plot of the driver Alfvén Mach number vs the electric field at time $600\Delta t$. Simulation results are denoted by the black circles. The red line denotes a power law of gradient ≈ 2.7

reflection propagating into the reconnection region however these are small enough not to have an effect on the outflow.

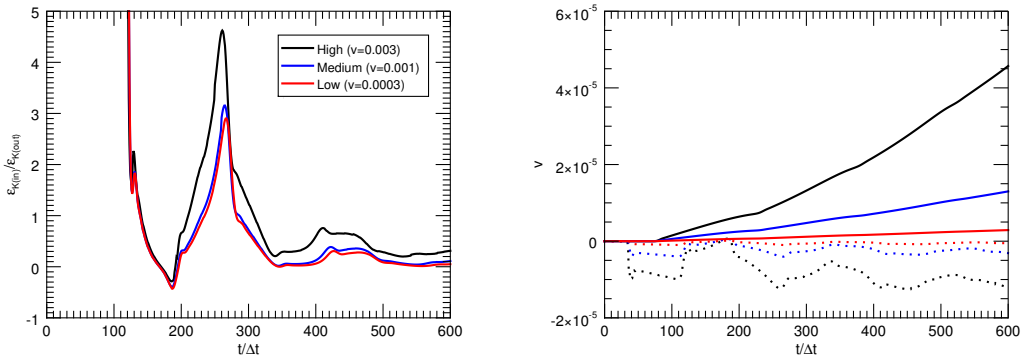

(a) (b)

FIGURE 4.9: (a) Kinetic energy ratio $\epsilon_{K(in)}/\epsilon_{K(out)}$. (b) Inflow (dashed) and outflow (solid) velocities at the centre of the inflow and outflow of the reconnection region.

The Ohmic heating ηJ^2 is shown in Figure 4.10. Note that everything before time $t = 80\Delta t$ has been set to zero since the reconnection region is ill-defined for these times. All velocity drivers have the same amount of Ohmic heating until approximately $t = 220\Delta t$. At this time the high driver begins to increase at a higher rate.

Internal energy per area is shown in Figure 4.11. In the high driver the internal energy appears to grow linearly for late times but demonstrates only a 3% increase. The low driver appears to result in a decrease in internal energy as time progresses. This is due to a peak in internal energy. Time $t = 100\Delta t$ corresponds to the start of the fast

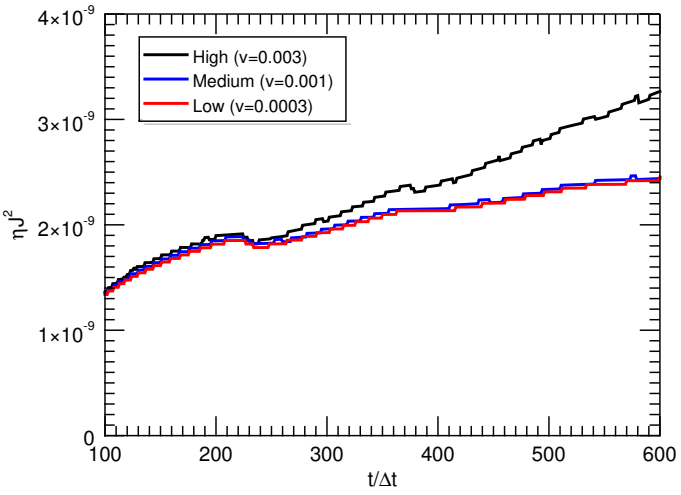

FIGURE 4.10: Ohmic heating ηJ^2 integrated over the reconnection region.

mode reflection so there is a peak here and then a steady decline to background levels ($\epsilon(t=0) \approx 4 \times 10^{-11}$ mA$^-$−2 using the ideal gas law).

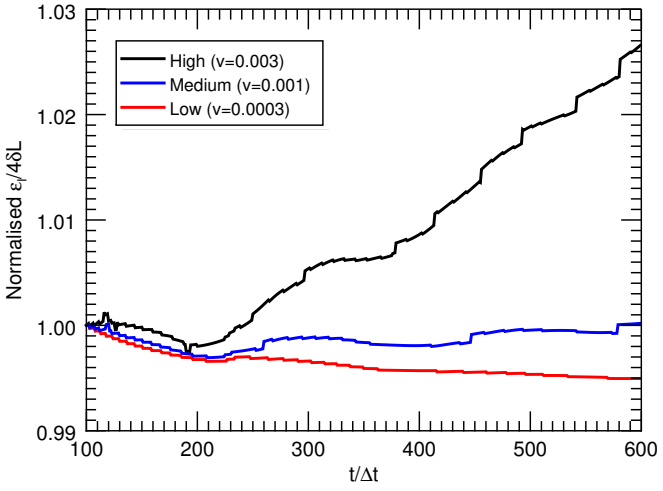

FIGURE 4.11: Internal energy in reconnection region per area for the coronal case. This is normalised to the internal energy per unit area at time $t = 100\Delta t$.

4.6 Plasma-β dependence

To investigate the effect of the plasma-β, the high driver from the previous section is used (note that this is also the baseline model in Section 4.4). Three plasma-β values have been tested: $0.002, 0.1$ and 1. The change in plasma-β changes the density ρ and hence the propagation time of the driven velocity. This changes the time at which the wavefronts collide. Note that the change in plasma-β affects the Alfvén speed via the

density and wave propagation time. The effects of the Alfvén speed was previously analysed (Section 4.5).

4.6.1 Reconnection region

As before, a reconnection region of width 2δ and length $2L$ can be fitted to the data. The half-width δ and half-length L are shown in Figure 4.12.

The half-width δ shows nearly identical values for late times. The main differences appear to be the magnitude of δ during the reflection phase, when the wave front hits the current sheet. However all three cases show the same qualitative behaviour. The absolute magnitude of the velocity driver is the same across the three cases and hence the rate at which magnetic flux is entering the diffusion region is the same. This results in similar increases in current density in the inflow region and hence similar behaviour in δ.

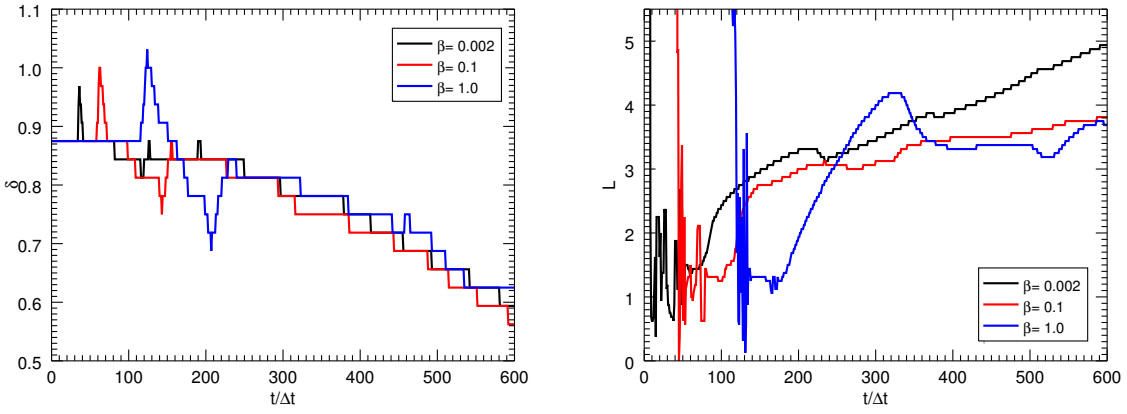

(a) (b)

FIGURE 4.12: (a) Half-width δ for different plasma-β values. (b) Half-length L for different plasma-β values.

The half-length L shows differences between the three tested plasma-β values. All three cases show a general increasing trend however the rates of this increase vary. In the case where plasma-$\beta = 0.002$, L increases in an approximately linear fashion. For the high plasma-β case, $\beta = 1$, the half-length L is relatively constant after the initial spike due to the waves colliding. L starts to increase for this case towards the end of the simulation. As the plasma-β increases, the density ρ increases and hence there is increased resistance to plasma being ejected from the current sheet, resulting in a smaller L for higher plasma-β values.

4.6.2 Electric field

The maximum electric field in the reconnection region is shown in Figure 4.13. There are significant differences between the electric field signature for different plasma-β values.

The low plasma-β case ($\beta = 0.002$) was analysed in Section 4.4 as the baseline model and Section 4.5 as the high case. A peak in electric field occurs during the reflection phase, when the two wavefronts collide at approximately $t = 80\Delta t$. After this, the electric field is relatively constant throughout the development phase. Finally there is a rise of 4 orders of magnitude in electric field as the reconnection phase starts-up at approximately time $t = 200\Delta t$ in Figure 4.13. This is due to the $\mathbf{v} \times \mathbf{B}$ term in Ohm's law becoming far larger than the $\eta\mathbf{J}$ term as was seen in Figure 4.7(b) and discussed in Section 4.5.2.

The other plasma-β values behave quite differently. As the plasma-β value increases, the plasma pressure becomes more important. This results in a larger electric field spike when the two wavefronts collide. Following this, the behaviour is different than in the baseline model (black line in Figure 4.13). The development phase occurs at a later time and has multiple peaks as oppose to being fairly constant. The reconnection phase is also very different from the baseline model; there is no large, smooth increase, instead the electric field is fairly constant and noisy. For the plasma-$\beta = 1$ case the advection term is far larger than the diffusion term. For the plasma-$\beta = 0.1$ case, the advection and diffusion terms are of similar orders of magnitude.

Increasing the plasma-β appears to inhibit the reconnection due to the increase plasma pressure. The electric field only demonstrates a sharp rise, indicative of reconnection, for high plasma-β values when the inflow velocity approaches the Alfvén speed.

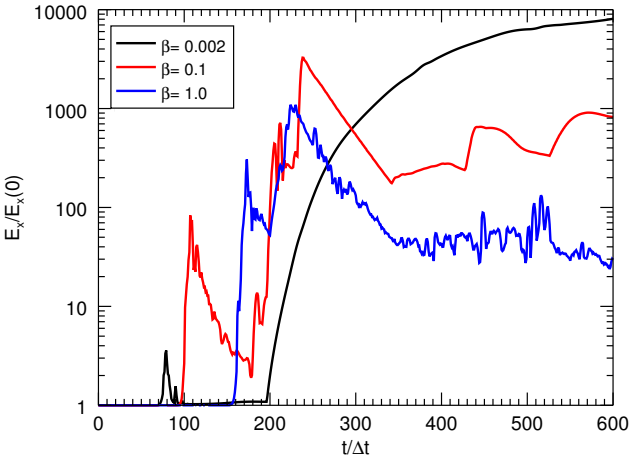

FIGURE 4.13: Maximum normalised electric field in the reconnection region for different plasma-β values.

4.6.3 Kinetic energy and velocity

The kinetic energy ratio shows that there is acceleration of the plasma for all three of the tested plasma-β cases, see Figure 4.14. The ratio of the kinetic energy into and out of the reconnection region shows that all three cases exhibit acceleration of the plasma at late times. This is further verified by the velocity values at the centres of the inflow and outflow at late times, see Figure 4.14. All three cases show a fairly constant inflow but a steadily increasing outflow at late times.

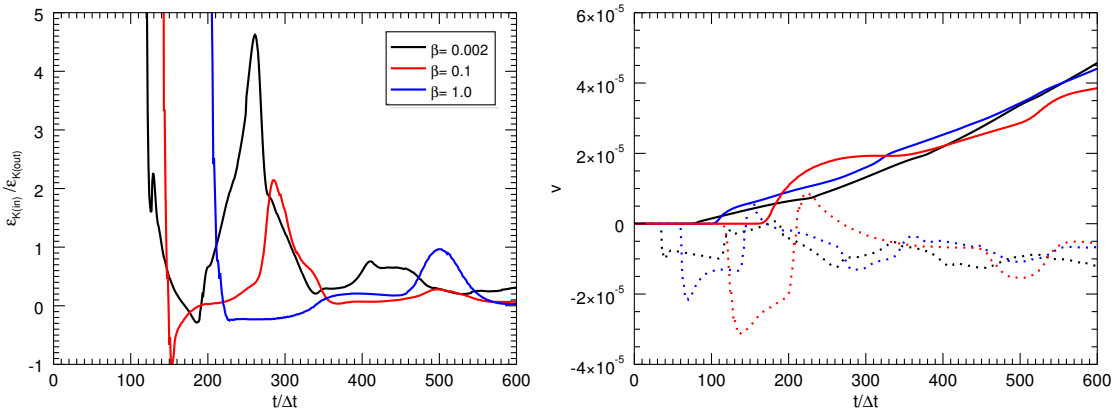

(a) (b)

FIGURE 4.14: (a) Kinetic energy ratio and (b) inflow (dashed) and outflow (solid) velocities for different plasma-β values

4.7 Resistivity dependence

A diffusion test was performed on the simulation grid determining that the numerical resistivity is of order $\eta_n \approx 10^{-8}\Omega$m, i.e. far smaller than the Spitzer resistivity for the coronal case $\eta = 10^{-6}\Omega$m (see Table 4.1). However, increasing the Spitzer resistivity to $\eta = 10^{-2}\Omega$m did not significantly change the structure of the current density. The reconnected magnetic field B_z along the line $z = 0$ does increase for the higher resistivity however remains small compared to the inflow magnetic field B_y. This shows that changing the resistivity does have an effect on the amount of reconnected magnetic field, however the reconnected flux remains too small to have an effect on other parameters. The velocity driver carries magnetic field towards the diffusion region and hence, the rate at which magnetic flux enters the diffusion region is determined by the velocity amplitude. This acts as a limiting factor on the reconnection rate during the onset of magnetic reconnection. Towards the end of the simulation, the advection term stabilises but the current term is still increasing. One would expect that the diffusion term ηJ

would eventually dominate the physics of the reconnection process as time increases beyond our simulation.

4.8 Ambipolar diffusion

In the solar chromosphere, the plasma is partially ionised. This introduces Cowling resistivity $\eta_\perp$ that acts perpendicular to the magnetic field and is calculated by Equation (4.9). $\eta_\perp$ appears in the internal energy equation (Equation (4.4)) and Ohm's law (Equation (4.5)). The neutral fraction $\xi_n = \xi_n(T, \rho)$ is calculated using the modified Saha equation, as implemented in Lare3d by Leake et al. [2005]. Ambipolar diffusion refers to the $\eta_\perp J_\perp$ term in Ohm's law (Equation (4.5)).

To investigate the effects of Cowling resistivity, simulations were performed using chromospheric conditions, see Table 4.3. Three initial temperature values have been chosen at 7200, 9200 and 10300 K such that the respective neutral fraction is 0.1, 0.5 and 0.9. The driver velocity is chosen to avoid shocks in the inflow region at all three temperatures. Note that the change in temperature changes the propagation speed and hence the time at which the wavefronts collide.

Parameter [Units]	Value
Plasma-β	0.1
Temperature [K]	$7200, 9200$ and 10300
Corresponding ξ_n	$0.9, 0.5$ and 0.1
Resistivity [Ωm]	10^{-3}

TABLE 4.3: Chromospheric parameters

4.8.1 Reconnection region

The reconnection region half-length L and half-width δ are shown in Figure 4.15. At late times, all three cases show a linear increase in L and a linear decrease in δ. There is only minimal difference between the considered cases in terms of the reconnection region half-width and half-length. Including neutrals results in a thinner current sheet, in line with previous studies [e.g. Brandenburg and Zweibel, 1994].

4.8.2 Electric field

Figure 4.16 shows the maximum electric field in the reconnection region. Again there is very little difference between the cases. All three cases show near identical behaviour,

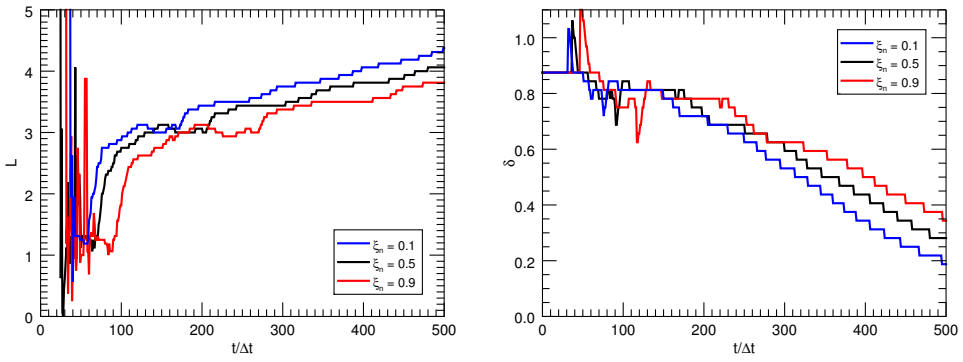

(a) (b)

FIGURE 4.15: (a) Half-length L and (b) half-width δ of the reconnection region with three different neutral fractions ξ_n. L is calculated using the maximum outflow. δ is calculated as the HWHM of J_x

both quantitatively and qualitatively. The staggering in time of the results is due to the difference in temperature altering the propagation speed of the driven wavefronts. The large increase in electric field occurs when the $\mathbf{v} \times \mathbf{B}$ term becomes larger than the $\eta\mathbf{J}$ term in Ohm's law.

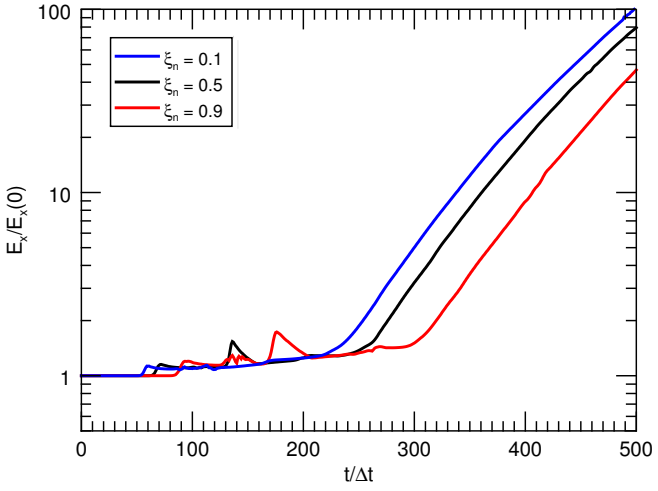

FIGURE 4.16: Normalised electric field for different neutral fractions ξ_n.

4.8.3 Current distribution

For a partially ionised plasma the distribution of the current should follow a power law of $-2/3$ [Brandenburg and Zweibel, 1994]. Figure 4.17 shows the distribution of the current J_x in the z-direction at time $t = 500\Delta t$ along the line $y = 0$, i.e. the distribution of the current along the inflow direction. At this time the edge of the diffusion region is located at $z \approx 0.2, 0.3$ and 0.4 for $\xi_n = 0.1, 0.5$ and 0.9 respectively (Figure 4.15(b)). All three

cases demonstrate a power law region with roughly the expected $-2/3$ gradient. This indicates that the inclusion of partial ionisation alters the distribution of the current along the inflow direction inside the diffusion region for $\xi_n = 0.5$ and $\xi_n = 0.9$ and just outside the diffusion region for $\xi_n = 0.1$. In contrast, there is no power-law region in the distribution of the current for the coronal case.

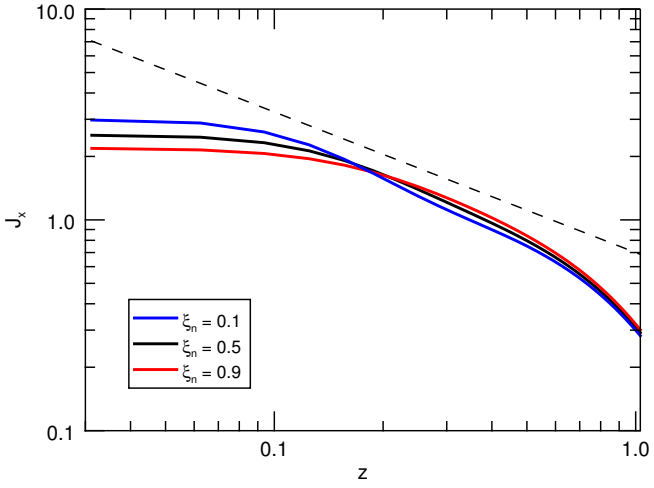

FIGURE 4.17: Current J_x for different neutral fractions ξ_n at time $t = 500\Delta t$. The dashed line represents the $-2/3$ scaling law of Brandenburg and Zweibel [1994].

4.8.4 Ohmic heating

There is a slight difference in the maximum percentage temperature increase when changing the neutral fraction. For a neutral fraction of $\xi_n = 0.5$ and $\xi_n = 0.1$ the temperature in the centre of the domain increases by approximately 280K. For $\xi_n = 0.9$ there is temperature increase of approximately 410K. The perpendicular resistivity depends on ξ_n^2 (Equation (4.9)) and hence the additional diffusion due to the $\eta_\perp J_\perp$ term is significantly higher when $\xi_n = 0.9$ than when $\xi_n = 0.5$ or $\xi_n = 0.1$, producing more of a temperature increase. The distribution of the heated plasma is roughly identical in all cases and confined to the reconnection region.

4.9 Photospheric vs chromospheric vs coronal

Now that the different parameters have been investigated separately, we can compare the reconnection event occurring at different atmospheric heights. The driver magnitude in all cases has been chosen such that the Alfvén Mach number on the inflow approaches but never exceeds unity. The key parameters in the different cases are in Table 4.4.

The output data for the simulations have been scaled such that the time for a fast-mode wave to propagate across the domain is approximately $100\Delta t$. This means the wavefronts collide at time $t \approx 50\Delta t$. The values of Δt are 100, 38.5 and 24 seconds for photosphere, chromosphere and corona respectively.

Parameter [Units]	Photosphere	Chromosphere	Corona
Plasma-β	1	0.1	0.002
Temperature [K]	6000	9200	10^6
Neutral fraction ξ_n	≈ 0.99	≈ 0.5	≈ 0
Resistivity [Ωm]	10^{-3}	10^{-3}	10^{-6}
Time Δt [s]	100	38.5	24

TABLE 4.4: Photospheric, chromospheric and coronal parameters

4.9.1 Size of the reconnection region

The half-length L and half-width δ of the reconnection region are shown in Figure 4.18. In the figure time is scaled by Δt and the photospheric case appears to narrow at the fastest rate.

By looking at the rates of the linear change in δ one can calculate the rate $\Delta\delta/\Delta t$ in real units (m s^{-1}), i.e. the speed at which the reconnection region is narrowing. These values are approximately 0.213, 0.4132 and 0.208 m s^{-1} for the photosphere, chromosphere and corona respectively. Therefore the fastest rate of change is in the chromosphere.

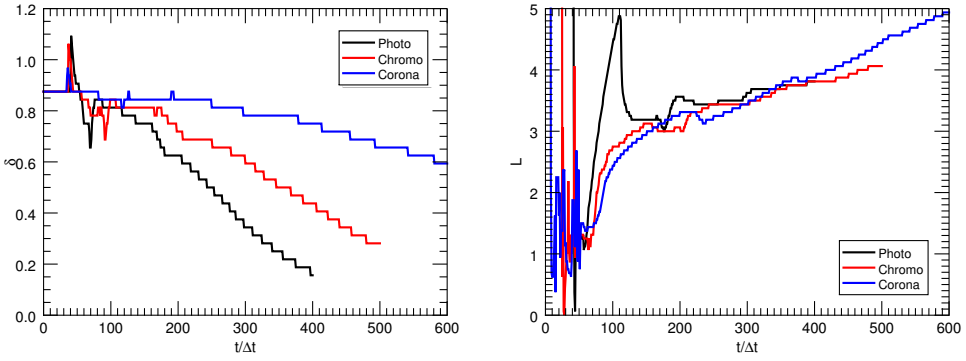

(a) (b)

FIGURE 4.18: (a) Half-width δ and (b) half-length L of the reconnection region for the three atmospheric heights.

4.9.2 Electric field

Figure 4.19 shows the electric field in each case normalised by its electric field at time $t = 0$. The three cases demonstrate very different behaviour during the reconnection phase. There are orders of magnitude difference between the maximum electric field in each case. In the photosphere, the electric field exhibits exponential behaviour (Figure 4.19) but has a very low gradient. There appears to be two separate exponential phases with different gradients: one between $180\Delta t$ and $280\Delta t$ corresponding to the tail end of the development phase, and one from $280\Delta t$ and $400\Delta t$ with a slightly steeper gradient that corresponds to the reconnection phase. The chromosphere has a very flat electric field until $t = 270\Delta t$ when the reconnection phase starts and the $\mathbf{v} \times \mathbf{B}$ term dominates. The corona has the highest electric field gradient, again corresponding to the $\mathbf{v} \times \mathbf{B}$ term dominating the electric field.

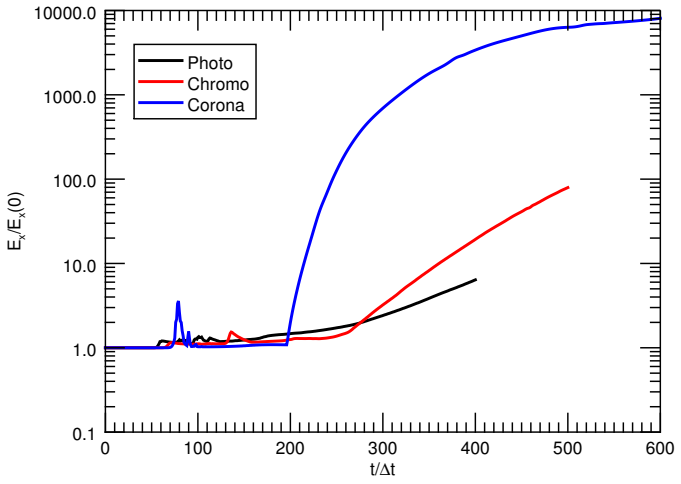

FIGURE 4.19: Normalised electric field for the three atmospheric heights.

The electric field signature also depends on the driver velocity. This was analysed for the coronal case in Section 4.5. The electric field for different driver velocities in the photosphere and chromosphere are shown in Figures 4.20(a) and 4.20(b) respectively. The different driver velocities are shown in Table 4.5 for the photospheric case and Table 4.6 for the chromospheric case. In the photosphere, only the fastest driver yields a steep gradient in electric field at late times. This occurs when the advection and diffusion terms are of the same order. In the chromosphere, one can produce behaviour in the electric field similar to both photospheric and coronal cases depending on the magnitude of the velocity driver. The fastest driver has comparable behaviour to the coronal case: a steep gradient in electric field and advection dominates at late times. However for slow drivers there is very little change in the electric field and the diffusion dominates, similar

to the slow photospheric case. Therefore reconnection occurring at chromospheric levels is highly dependent on the magnitude of the velocity driver.

Driver name	Alfvén Mach Number
High	0.0808
Medium	0.0412
Low	0.00838

TABLE 4.5: Driver Alfvén Mach numbers for the photospheric case.

Driver name	Alfvén Mach Number
High	0.021
Mid-High	0.013
Mid	0.0084
Mid-Low	0.0042
Low	0.0021

TABLE 4.6: Driver Alfvén Mach numbers for the chromospheric case.

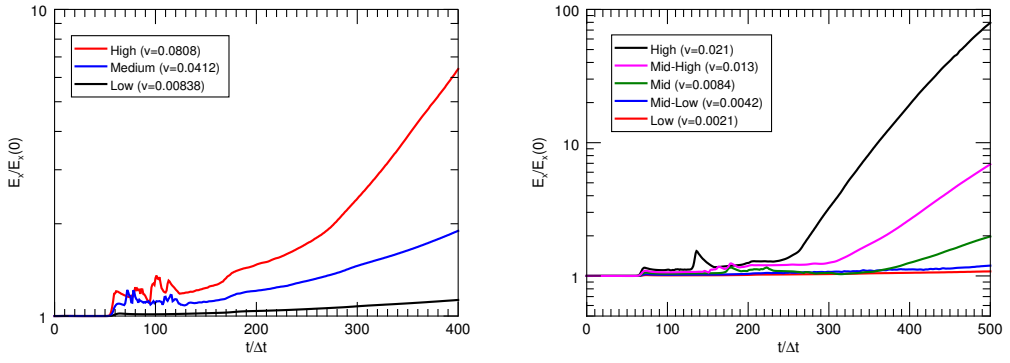

(a) (b)

FIGURE 4.20: (a) Normalised electric field in the photospheric case with different velocity drivers. (b) Normalised electric field in the chromospheric case with different velocity drivers.

4.9.3 Internal energy

The normalised internal energy per unit area in the reconnection region is shown in Figure 4.21. This is normalised by the value at time $t = 100\Delta t$. The photospheric case shows the largest increase.

The heating can be calculated in real terms. In all cases the maximum heating occurs at the centre of the domain. The original values of the temperature are 6000, 9200 and 10^6 K for the photosphere, chromosphere and corona (Table 4.4). The temperature change

at the end of the simulation is approximately 186, 267 and 39456 K in the three cases. This corresponds to a 3.1%, 2.9% and 3.9% rise in temperature over the simulation for the photosphere, chromosphere and corona.

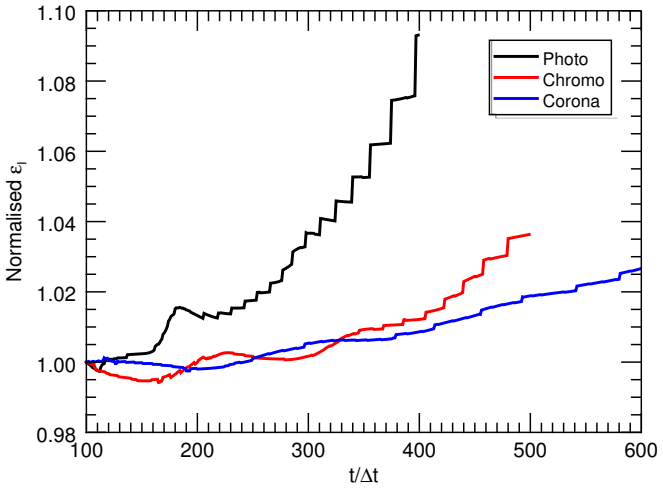

FIGURE 4.21: Normalised internal energy per unit area in the reconnection region for the three atmospheric heights. This is normalised to the internal energy per unit area at time $t = 100\Delta t$.

The shape of the heating region also varies in the different cases, see Figure 4.22. For the photospheric case, the heat appears to be carried out along the double Y-shaped slow-mode shocks that exist on the interface between inflow and outflow regions. This is similar to the shape of the outflow jet and termination shocks in Forbes [1988]. The coronal case produces a fairly evenly distributed heating region with very little heat being carried out along the magnetic field lines. The chromospheric case has a very localised heating region of approximately the same size as the reconnection region. The power law current distribution for the chromospheric case results in a thin current sheet and hence a very localised Ohmic heating region.

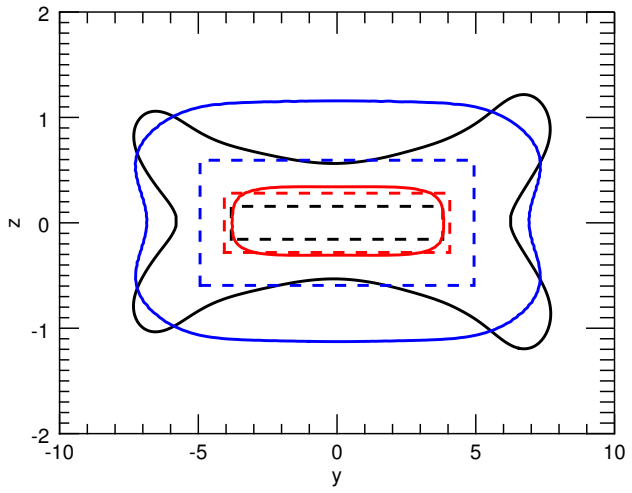

FIGURE 4.22: Shape of the heating region for the photospheric (black), chromospheric (red) and coronal (blue). The level is half the maximum heating, i.e. a temperature increase of 1.5% for photosphere and chromosphere and 2% for the corona. The diffusion region of each case is overplotted with a dashed line.

4.10 Conclusions

In this chapter the onset of 2D magnetic reconnection has been investigated at different atmospheric heights of the Sun, namely the solar corona, chromosphere and photosphere, by using a sub-Alfvénic velocity driver specified perpendicular to a Harris current sheet. Waves and flows are ubiquitous in the solar atmosphere and can encounter current sheets, triggering reconnection. This external velocity driver allows us to study the early behaviour of magnetic reconnection in a naturalistic manner.

The process has been separated into three phases: reflection, development and reconnection. When the velocity wave hits the centre of the Harris current sheet there is a fast mode reflection. This causes the current sheet to fluctuate in width. During the development phase, the current density starts to rise and magnetic field lines begin to reconnect. Finally, during the reconnection phase, there is clear acceleration of the plasma exiting the reconnection region.

The reconnection event behaves Sweet-Parker-like in some ways, and Petschek-like in others. The reconnection region is narrow and elongated, as in Sweet-Parker. However weak slow-mode shocks form on the interface between the inflow and outflow and the outflow velocity is closer to the Petschek speed, where $v_{outflow} = M_{A(inflow)}\sqrt{\rho_{inflow}/\rho_{outflow}}$. The inflow magnetic field decreases towards the reconnection region thus the general behaviour is similar to the flux pile-up models [e.g. Priest and Forbes, 1986].

In the photosphere, the atmospheric conditions act to inhibit reconnection and a clear reconnection signature was only obtained when the velocity entering the reconnection region approached the Alfvén speed. The slow-mode shocks that form however are far stronger than in the other two atmospheric cases and carry out the heating that occurs in the reconnection region. The coronal case has a very strong signature of reconnection in the electric field, where the normalised electric field increases by four orders of magnitude. The chromosphere lies somewhere between the corona and photosphere in terms of behaviour. There is a strong increase of approximately two orders of magnitude in electric field for an inflow velocity close to the Alfvén speed. However slower drivers produce an electric field signature closer to the photospheric case. The heating in the chromosphere is confined to the diffusion region.

Reconnection is ubiquitous in the solar atmosphere and plays a key role in many phenomena occurring at photospheric, chromospheric and coronal levels. This chapter investigated the onset of magnetic reconnection at different atmospheric heights and analysed the role of different parameters. The key parameters in determining the behaviour of reconnection onset at different atmospheric heights are the plasma-β and the driver velocity. A lower plasma-β creates a larger change in the electric field signature of the reconnection event. A high plasma-β acts to hinder the magnetic reconnection and a sharp rise in electric field is only obtained as the inflow into the reconnection region approaches the Alfvén speed. For low plasma-β a sharp rise is obtained in electric field for the all tested velocity drivers however the magnitude of this rise is dependent on the amplitude of the velocity driver; a higher amplitude driver produces a larger rise in electric field.

Chapter 5

Summary

This thesis has presented research into the behaviour of a chromospheric resonator above a sunspot umbrae and the resultant coronal intensity, observational signatures of a kink-unstable flux rope, and the onset of magnetic reconnection at different atmospheric heights.

5.1 Sunspot Resonating Cavity

The first branch of this thesis (Chapter 2) investigated the wave propagation above sunspot umbrae. The steep temperature gradients at the photosphere and transition region allow waves to resonate in the chromospheric cavity above sunspot umbrae. These resonant waves produce an upwards propagating velocity signature in the corona with a strong peak around the three-minute frequency range [e.g. Beckers and Schultz, 1972, De Moortel et al., 2006, Marsh and Walsh, 2006, Shibasaki, 2001, Thomas et al., 1987]. Multiple numerical simulations were performed looking at the effect of different continuous random noise colours and chromospheric cavity size on the resultant coronal velocity signature. Both a flat profile (uniform temperature) and a step profile (two uniform temperature regions) were investigated.

It was found that varying the noise colour of the velocity driver had no significant effect on the coronal frequency spectra. The reasoning behind this is that the resonator redistributes energy to its prefered frequencies.

The coronal frequency spectra has four regions (Figures 2.10 and 2.11) that persisted at the same frequencies regardless of driver colour or chromospheric cavity size. One of these regions was between 17 and 200 mHz where the spectral power followed a power

law that is correlated with chromospheric cavity size. This gradient was estimated by fitting a line through the data using the method of least squares.

Varying the chromospheric cavity size was found to change the frequency spectra in the corona. In particular, it was found that increasing the size of the chromospheric cavity decreased the gradient of the coronal frequency spectra. This provides a potentially useful diagnostic for indirectly measuring the size of the chromospheric cavity.

This work has been published as Snow et al. [2015].

5.2 Forward Modelling

5.2.1 Resonances

Line-of-sight integration was performed on the coronal signature from the resonances research, using the flat profile. Several spectral lines from SDO/AIA, SOHO/SUMER and Hinode/EIS were considered. The LOS frequency spectra varied greatly from the single-point numerical analysis. The acoustic cut-off frequency was present in the LOS spectra, at approximately the same frequency as the single-point analysis. The frequency spectra obtained in Figure 3.2 are very similar to observational papers as can be seen in Tian et al. [2014]; an excited range of frequencies is present between approximately 4.5 and 10 mHz [Reznikova et al., 2012, Thomas et al., 1987, Tian et al., 2014]. Unlike the single point results, there was no discernable trend in the gradient of the frequencies. However, in the LOS spectra, changing the size of the chromospheric cavity yielded a different trend; as the chromospheric cavity size increased, the broadband of excited frequencies became narrower. This provides a potentially useful diagnostic for indirectly measuring the size of the chromospheric cavity via the velocity signature present in the corona.

5.2.2 Kink-unstable coronal flux rope

LOS integration was also performed to generate the observational signatures from a 3D simulation of a kink-unstable coronal flux rope. The numerical simulation was performed by Botha et al. [2011]. This branch of the thesis generated synthetic spectral lines using Chianti v7 and used these to synthesise the observational intensities and Doppler velocities, as observed by Hinode/EIS and DKIST/DL-NIRSP.

5.2.2.1 Hinode/EIS

Hinode/EIS rasters were calculated by integrating along a line-of-sight, spatially degrading resulting intensity and finally integrating over the exposure time (50 seconds). There are three main observational signatures that can be detected in the intensity and Doppler maps.

First, there is an increase in intensity towards the edge of the loop in the intensity rasters. This is due to the loop conducting heat radially outwards and activating different spectral lines.

Secondly, the growth of the loop is measurable in the sit-and-stare intensity maps. This is an overestimate of the loop width compared to the loop width measured in the simulation resolution results. This discrepancy is largest when the loop is growing rapidly in width, i.e. as the kink instability enters the non-linear phase.

Finally, the dense Doppler raster located at the centre of the loop detected oppositely directed Doppler velocities. This corresponds to velocity begin guided along a twisted magnetic field line in the simulation.

These three results are signatures of a kink-unstable coronal flux rope that can be detected by Hinode/EIS. However, the time integration and spatial degradation in creating the observable signatures annihilate small scale transient features present in the simulation.

5.2.2.2 DKIST/DL-NIRSP

A prediction of the observational signature of the kink-unstable coronal loop using the coronal mode of DKIST/DL-NIRSP was also performed by synthesising a few spectral lines using Chianti and recreating the mosaics that this future instrument will observe. The end result showed considerable levels of structure in the intensity maps. The loop width was measurable in the intensity maps for both the moving mosaic and the sit-and-stare modes. Small-scale structure was also present in the moving mosaics and features could be tracked across tiles.

5.3 Onset of 2D Magnetic Reconnection at Different Atmospheric Heights

The final branch of the thesis (Chapter 4) looked at the onset of 2D magnetic reconnection at different atmospheric heights. Numerical simulations were performed where

reconnection was triggered using an external (non-local) velocity driver located far away from the current sheet. This allows us to investigate the onset of magnetic reconnection, i.e the physics of the start-up process of magnetic reconnection. Waves and flows are ubiquitous in the solar atmosphere and can encounter current sheets and initiate reconnection. This type of driver allows us to investigate the onset of reconnection triggered in such a manner. The parameter space was investigated looking at atmospheric conditions that correspond to photospheric, chromospheric and coronal regimes.

The onset process has been separated into three phases; reflection, development and reconnection. As the driver propagates towards the current sheet, a wave front forms due to the decreasing Alfvén speed. When these wave fronts collide, it produces a fast-mode reflection that propagates towards the driven boundaries (this reflection is annihilated by the damping region). In the wake of this, the current starts to rise and magnetic field begins to reconnect. Finally, stronger magnetic fields reconnect and a stable reconnection phase is reached.

The distribution of the heating varies across the different atmospheric layers. In the corona, the heating is fairly evenly distributed in a large are surrounding the reconnection region. In the photospheric case, the heating is carried out along the slow-mode shocks. In the chromospheric case, the heating is confined to the reconnection region.

The reconnection is found depend on the magnitude of the velocity driver. In the corona, a large increase in electric field is obtained for a range of velocities. In the photosphere, a strong signature of reconnection was only obtained as the velocity flowing into the reconnection region approaches the Alfvén speed.

Reconnection is ubiquitous in the solar atmosphere and plays a key role in many phenomena occurring at photospheric, chromospheric and coronal levels. This paper investigated the onset of magnetic reconnection at different atmospheric heights and analysed the role of different parameters. The key parameters in determining the behaviour of reconnection onset at different atmospheric heights are the plasma-β and the driver velocity. A lower plasma-β creates a larger change in the electric field signature of the reconnection event. A high plasma-β acts to hinder the magnetic reconnection and a sharp rise in electric field is only obtained as the inflow into the reconnection region approaches the Alfvén speed. For low plasma-β a sharp rise is obtained in electric field for the all tested velocity drivers however the magnitude of this rise is dependent on the amplitude of the velocity driver; a higher amplitude driver produces a larger rise in electric field.

5.4 Suggestions for future work

The research presented in this thesis can be expanded in a number of ways. Here I will list a few potential avenues for continuation of this research.

One of the remaining questions from the resonances project is why the broad peak of excited frequencies extends to 17 mHz. An interesting extension on the resonances research would be to investigate the the behaviour of the chromospheric resonator in multiple dimensions. Also the behaviour of shock waves in the resonator would be interesting, since these would change the thermal structure and hence the behaviour of resonant waves.

The EIS section of the forward modelling chapter can be extended using a convolution function to more accurately mimic the instrument observations. This would effectively spread out any sharp structures present. Also, the Fe XV line is strong enough that a shorter exposure time can be used. Investigating the signatures of the Fe XV line using a 6 second exposure would therefore be another direction for future work.

For the forward modelling using DKIST/DL-NIRSP, it would be interesting to investigate different spectral lines which cover a larger thermal range. This would reveal different structure in the loop across the different lines. DKIST/NL-NIRSP will also be able to observe the Fe XIII pair at 10749 and 10801 Å. This provides a density diagnostic based on the ratio of these two lines. Comparing the synthesised density calculated from the intensity ratio to the simulation density is also a potential avenue for future research.

Finally, the reconnection section has a few interesting results that could be investigated further. It is found that the magnetic flux that enters the diffusion region, and hence the amount of flux that can reconnect, is determined by the advection term. However, as time increases, the advection term stagnates, whereas the diffusion term rises. This means that after a certain time, the diffusion term will dominate. The transition between these two phases would be potential future work. Also, one could consider using a inflow velocity that is above the Alfvén speed when it enters the diffusion region.

Appendix A

DKIST/DL-NIRSP standard observation mode

Example #3:	**Wide field, low resolution, off-limb coronal dynamics and magnetometry**		
SPATIAL COVERAGE AND RESOLUTION			
Resolution Mode	Wide		
Spatial Sampling	0.464″ per pixel		
Spatial resolution limit	0.928″		
Target location	On-limb ; Line and background brightnesses are 100.e-6 and 25e-6 of disk center		
Num. of IFU x/y positions	1 / 1		
Total Field of View	27.84″ x 18.56″		
SPECTRAL INFO:	Band #1	Band #2	Band #3
Wavelength:	789.0 nm	Fe XIII 1074.7 nm	Si X 1430 nm
Velocity coverage:	+/- 125 km/sec	+/- 125 km/sec	+/- 125 km/sec
Spectral dispersion	0.003417 nm/pixel	0.004332 nm / pixel	0.00626 nm/pixel
Spectral resolution (R)	125000	125000	125000
Polarimetric SNR	370	490	480
Polarimetric Noise (norm.)	0.0027	0.002	0.002
Polarimetric Noise (norm.) after coadding all 120 time steps of sequence	0.00025	0.00019	0.00019
TIMING SUMMARY			
Duration of single scan tile	21.26 seconds		
Total integration per tile	21.26 seconds		
Full field of view map	21.21 seconds		
Time for 120 maps	42.52 minutes		
DATA RATES			
Average raw data rate	13 MB/sec		
Total raw data (20 maps)	31.88 GB (does not include calibration data)		

Bibliography

Arber, T., Longbottom, A. W., Gerrard, C., and Milne, A. M. (2001). *J. Comput. Phys*, 171(151).

Arber, T. D., Botha, G. J. J., and Brady, C. S. (2009). *ApJ*, 705:1183–1188.

Arber, T. D., Haynes, M., and Leake, J. E. (2007). *ApJ*, 666:541–546.

Athay, R. G. and Thomas, R. N. (1961). *Physics of the solar chromosphere*.

Avrett, E. and Loeser, R. (2008). *ApJS*, 175(229).

Bard, S. and Carlson, M. (2010). *ApJ*, 722(888).

Beckers, J. and Schultz, R. (1972). *Sol. Phys.*, 27(1):61–70.

Bel, N. and Leroy, B. (1977). *A&A*, 55:239.

Bhattacharjee, A. (2004). *Annu. Rev. Astron. Astrophys.*, 42:365–384.

Boerner, P., Edwards, C., Lemen, J., Rausch, A., Schrijver, C., Shine, R., Shing, L., Stern, R., Tarbell, T., Title, A., Wolfson, C. J., Soufli, R., Spiller, E., Gullikson, E., McKenzie, D., Windt, D., Golub, L., Podgorski, W., Testa, P., and Weber, M. (2012). *Sol. Phys.*, 275:41–66.

Bogdan, T. J. (2000). *Sol. Phys.*, 192(373).

Bogdan, T. J. and Judge, P. G. (2006). *Phil. Trans. R. Soc. A.*, 364(313).

Botha, G. J., Arber, T. D., Nakariakov, V. M., and Zhugzhda, Y. D. (2011). *ApJ*, 728(84).

Botha, G. J. J., Arber, T. D., and Hood, A. W. (2011). *A&A*, 525:A96.

Botha, G. J. J., Arber, T. D., and Srivastava, A. K. (2012). *ApJ*, 745:53.

Brandenburg, A. and Zweibel, E. G. (1994). *ApJ*, 427:L91–L94.

Brown, J. C. (1973). *Sol. Phys.*, 29:421–427.

De Moortel, I., Ireland, J., Hood, A. W., and Walsh, R. W. (2006). *A&A*, 354(334).

De Moortel, I. and Nakariakov, V. M. (2012). *Phil. Trans. R. Soc. A.*, 370(3193).

Dere, K., Landi, E., Mason, H., Fossi, B. M., and Young, P. (1997). *A&AS*, 125(1):149–173.

Ellerman, F. (1917). *ApJ*, 46:298.

Evans, C. R. and Hawley, J. F. (1988). *ApJ*, 332:659–677.

Fitzpatrick, R. (2003). *Physics of Plasmas*, 10:2304–2312.

Fleck, B. and Schmitz, F. (1991). *A&A*, 250(235).

Forbes, T. G. (1988). *Sol. Phys.*, 117:97–121.

Gary, A. (2001). *Sol. Phys.*, 203:71–86.

Hahm, T. S. and Kulsrud, R. M. (1985). *Physics of Fluids*, 28:2412–2418.

Hillier, A., Takasao, S., and Nakamura, N. (2016). *A&A*, 591:A112.

Hood, A. W., Browning, P. K., and van der Linden, R. A. M. (2009). *A&A*, 506:913–925.

Jess, D. B., Moortel, I. D., Mathioudakis, M., Christian, D. J., Reardon, K. P., Keys, P. H., and Keenan, F. P. (2012). *ApJ*, 757(2):160.

Katsukawa, Y., Berger, T. E., Ichimoto, K., Lites, B. W., Nagata, S., Shimizu, T., Shine, R. A., Suematsu, Y., Tarbell, T. D., Title, A. M., and Tsuneta, S. (2007). *Science*, 318:1594.

Keil, S. L., Rimmele, T. R., Wagner, J., and ATST Team (2010). *Astron. Nachr.*, 331:609.

Lacoste, H., editor (2004). *Waves, Oscillations and Small Scale Transient Events in the Solar Atmosphere: A Joint View form SOHO and TRACE*. ESA.

Landi, E., Young, P., Dere, K., Del Zanna, G., and Mason, H. (2013). *ApJ*, 763(2):86.

Leake, J. E., Arber, T., and Khodachenko, M. (2005). *A&A*, 442(3):1091–1098.

Leake, J. E. and Arber, T. D. (2006). *A&A*, 450:805–818.

Leake, J. E., Lukin, V. S., Linton, M. G., and Meier, E. T. (2012). *ApJ*, 760:109.

Lites, B. W. and Skumanich, A. (1982). *ApJS*, 49(293).

Maltby, P., Averett, E. H., Carlsson, M., Kjeldseth-Moe, O., Kurucz, R. L., and Loeser, R. (1986). *ApJ*, 306(284).

Malyshkin, L. M. and Zweibel, E. G. (2011). *ApJ*, 739:72.

Marsh, M. S. and Walsh, R. W. (2006). *ApJ*, 643(540).

McIntosh, S. W. and Jefferies, S. M. (2006). *ApJ*, 647:L77–L81.

Moore, R. L., Sterling, A. C., Hudson, H. S., and Lemen, J. R. (2001). *ApJ*, 552:833–848.

Morita, S., Shibata, K., Ueno, S., Ichimoto, K., Kitai, R., and Otsuji, K.-I. (2010). *PASJ*, 62:901–920.

NASA (2007). Layers of the sun. Online. Accessed August, 2016.

Nelson, C. J., Shelyag, S., Mathioudakis, M., Doyle, J. G., Madjarska, M. S., Uitenbroek, H., and Erdélyi, R. (2013). Ellerman Bombs: Evidence for Magnetic Reconnection in the Lower Solar Atmosphere. *ApJ*, 779:125.

Parker, E. N. (1957). *J. Geophys. Res.*, 62(4):509–520.

Petschek, H. E. (1964). *NASA Special Publication*, 50:425.

Pontin, D. I. (2012). *Phil. Trans. R. Soc. A*, 370:3169–3192.

Priest, E. (2014). *Magnetohydrodynamics of the Sun*. Cambridge University Press.

Priest, E. and Forbes, T. (2000). *Magnetic Reconnection*.

Priest, E. R. and Forbes, T. G. (1986). *J.G.R.*, 91:5579–5588.

Rabello-Soares, M. C., Roca Cortes, T., Jimenez, A., Andersen, B. N., and Appourchaux, T. (1997). *A&A*, 318(970).

Reid, A., Mathioudakis, M., Doyle, J. G., Scullion, E., Nelson, C. J., Henriques, V., and Ray, T. (2016). *ApJ*, 823:110.

Reznikova, V. E., Shibasaki, K., Sych, R. A., and Nakariakov, V. M. (2012). *ApJ*, 746(119).

Roberts, B. (2006). *Phil. Trans. R. Soc. A.*, 364(447).

Sakai, J. I. and Smith, P. D. (2008). *ApJ*, 687:L127.

Savcheva, A., Cirtain, J., Deluca, E. E., Lundquist, L. L., Golub, L., Weber, M., Shimojo, M., Shibasaki, K., Sakao, T., Narukage, N., Tsuneta, S., and Kano, R. (2007). *PASJ*, 59:S771–S778.

Schmelz, J. T., Reames, D. V., von Steiger, R., and Basu, S. (2012). *ApJ*, 755(1):33.

Shibasaki, K. (2001). *ApJ*, 550(1113).

Shibata, K., Ishido, Y., Acton, L. W., Strong, K. T., Hirayama, T., Uchida, Y., McAllister, A. H., Matsumoto, R., Tsuneta, S., Shimizu, T., Hara, H., Sakurai, T., Ichimoto, K., Nishino, Y., and Ogawara, Y. (1992). *PASJ*, 44:L173–L179.

Shibata, K., Nakamura, T., Matsumoto, T., Otsuji, K., Okamoto, T. J., Nishizuka, N., Kawate, T., Watanabe, H., Nagata, S., UeNo, S., Kitai, R., Nozawa, S., Tsuneta, S., Suematsu, Y., Ichimoto, K., Shimizu, T., Katsukawa, Y., Tarbell, T. D., Berger, T. E., Lites, B. W., Shine, R. A., and Title, A. M. (2007). *Science*, 318:1591.

Singh, K. A. P., Hillier, A., Isobe, H., and Shibata, K. (2015). *PASJ*, 67:96.

Smith, P. D. and Sakai, J. I. (2008). *A&A*, 486:569–575.

Snow, B., Botha, G. J. J., McLaughlin, J. A., and Hillier, A. (2016). *A&A*, Submitted.

Snow, B., Botha, G. J. J., and Régnier, S. (2015). *A&A*, 580:A107.

Spitzer, L. (1962). *Physics of fully ionized gases*. Interscience tracts on physics and astronomy. Interscience Publishers.

Srivastava, A. K., Zaqarashvili, T. V., Kumar, P., and Khodachenko, M. L. (2010). *ApJ*, 715:292–299.

Stangalini, M., Giannattasio, F., Del Moro, D., and Berrilli, F. (2012). *A&A*, 539(L4).

Staude, J. (1981). *A&A*, 100(284).

Sweet, P. A. (1958). The neutral point theory of solar flares. In *Electromagnetic phenomena in cosmical physics*, volume 6, page 123.

Sych, R., Zaqarashvili, T. V., Nakariakov, V. M., Anfinogentov, S. A., Shibasaki, K., and Yan, Y. (2011). *A&A*, 539.

Taroyan, Y. and Erdelyi, R. (2008). *Sol. Phys.*, 251(523).

Thomas, J. H., Lites, B. W., Gurman, J. B., and Ladd, E. F. (1987). *ApJ*, 312(457).

Tian, H., DeLuca, E., Reeves, K. K., Mckillop, S., De Pontieu, B., Martinez-Sykora, J., Carlsson, M., Hansteen, V., Kleint, L., Cheung, M., Golub, L., Saar, S., Testa, P., Weber, M., Lemen, J., Title, A., Boerner, P., Hurlburt, N., Tarbell, T. D., Wuelser, J. P., Kankerborg, C., Jaeggli, S., and McIntosh, S. W. (2014). *ApJ*, 786(137).

Ulmschneider, P., Rammacher, W., Musielak, Z. E., and Kalkofen, W. (2005). *ApJ*, 631(L155).

Vernazza, J. E., Avrett, E. H., and Loeser, R. (1981). *ApJ Sup*, 45:635–725.

Wang, X. and Bhattacharjee, A. (1992). *Physics of Fluids B*, 4:1795–1799.

Wilson, A., editor (1997). *The Corona and Solar Wind Near Minimum Activity*, Institute of Theoretical Astrophysics, University of Oslo, Norway. ESA.

Yamada, M., Kulsrud, R., and Ji, H. (2010). *Reviews of Modern Physics*, 82:603–664.

Yuan, D., Nakariakov, V. M., Chorley, N., and Foullon, C. (2011). *A&A*, 533(A116).

Yuan, D., Pascoe, D. J., Nakariakov, V. M., Li, B., and Keppens, R. (2015). *ApJ*, 799:221.

Yuan, D., Sych, R., Reznikova, V. E., and Nakariakov, V. M. (2014). *A&A*, 561:A19.

Zaqarashvili, T. V., Khodachenko, M. L., and Soler, R. (2013). Torsional Alfvén waves in partially ionized solar plasma: effects of neutral helium and stratification. *A& A*, 549:A113.

Zhugzhda, Y. D. (2008). *Sol. Phys.*, 251(501).

Zweibel, E. G. (1989). Magnetic reconnection in partially ionized gases. *ApJ*, 340:550–557.

Zweibel, E. G. and Yamada, M. (2009). *Annu. Rev. Astron. Astrophys.*, 47:291–332.